ON THE ORIGIN OF NEUTRAL HYDROGEN CLOUDS IN NEARBY GALAXY GROUPS: THE ROLE OF GALAXY INTERACTIONS

By

KATIE MAE CHYNOWETH

Dissertation

Submitted to the Faculty of the
Graduate School of Vanderbilt University
in partial fulfillment of the requirements
for the degree of
DOCTOR OF PHILOSOPHY
in
Physics

May, 2010

Nashville, Tennessee

Approved:

Prof. Kelly Holley-Bockelmann

Prof. Glen Langston

Prof. David Weintraub

Prof. Robert A. Knop Jr.

Prof. Kalman Varga

PHYSICS AND ASTRONOMY

ON THE ORIGIN OF NEUTRAL HYDROGEN CLOUDS IN NEARBY GALAXY GROUPS: THE ROLE OF GALAXY INTERACTIONS

KATIE MAE CHYNOWETH

Dissertation under the direction of Prof. K. Holley-Bockelmann & Prof. G. Langston

This thesis addresses the origin of the High Velocity Clouds (HVCs) observed around the Milky Way and other nearby galaxies. Such clouds are likely created through a combination of galactic fountains, galaxy interactions, dark matter substructure, and cold accretion. The aim is to explore the role of galaxy interactions in generating such clouds. This thesis also tests predictions for H I -embedded dark matter halos made by the Lambda Cold Dark Matter (ΛCDM) cosmological model.

I address these questions by using sensitive radio observations of nearby galaxy groups, to search for clouds of neutral hydrogen, and by comparing the observations to numerical simulations. The groups have varying levels of galaxy interactions by design. I find 9 clouds in the M81 galaxy group – the most highly interacting system. I also find 4 clouds that may be associated with the Milky Way HVC Complex A. I find two H I clouds in the direction of the Canes I galaxy group. However, these clouds may be HVCs associated with either the Canes I group or the more distant galaxy KUG 1218+387.

Using a statistical comparison of observed data to numerical models, I show that the M81 group H I clouds are unrelated to dark matter halos. Since the clouds are located in the most highly interacting group, it is likely that the clouds are formed via galaxy interactions. However, more simulations are needed to determine the expected properties for H I clouds generated through galaxy interactions. To this end, I have run a suite of galaxy group simulations, and have begun analysis.

Future work in determining H I cloud formation mechanisms should include high-resolution H I observations with the EVLA to determine substructure; UV and optical observations to search for a stellar component; and comparison with simulations of the M81 Group that include all the relevant gas physics and allow for cold accretion.

Approved____ Date__________

ACKNOWLEDGEMENTS

I would like to express my heartfelt thanks to all who supported my efforts during graduate school. My parents, Mark and Kathleen Chynoweth, and my brother, Roy Chynoweth, for their unfailing love, humor, and encouragement. My Grandpa Bill Chynoweth, who taught me to love calculus and computers and questions – this dissertation is dedicated to him.

Jared Keating, for his love, support, patience, and amazing computer repair skills.

The Father, the Son, and the Holy Spirit, from whom all blessings flow. All of the churches that provided me a home and surrogate family in my travels, especially the Nashville Cathedral of the Incarnation, St. John Neumann's and St. Mark's in West Virginia, and Holy Family Catholic Church in Marietta, Georgia.

Sarah Fitzgerald, for her friendship and support that brought a smile to so many work days. All of my friends at Vanderbilt, particularly Sonali Shukla and Yilen Gomez Maqueo Chew for the use of their couches. The entire Chynoweth and Wermeling families – I am proud to be a member of both. My truck, whose continued working condition is a true miracle. The National Radio Astronomy Observatory and the Physics Department at Vanderbilt University, without whom I'd have no thesis at all. Finally, my advisors Glen Langston and Kelly Holley-Bockelmann, and the rest of my committee, for their guidance.

TABLE OF CONTENTS

Page

Chapter

Appendices

LIST OF TABLES

LIST OF FIGURES

CHAPTER I

INTRODUCTION

This dissertation addresses the origin of the High Velocity Clouds (HVCs) observed around the Milky Way and other nearby galaxies. In particular, this dissertation explores the role of galaxy-galaxy interactions as an originating mechanism for such clouds. In addition to investigating the galaxy interaction/HVC connection, this dissertation places observational constraints on two fundamental questions concerning the process of galaxy formation:

1. Are the predictions of the currently favored Lambda Cold Dark Matter (ΛCDM) cosmological model confirmed by observations of nearby galaxies?
2. Are the large number of HVCs observed around the Milky Way significant evidence for the continuing process of galaxy formation, through cold accretion in the form of primordial neutral hydrogen?

This dissertation addresses these questions by making sensitive observations of nearby galaxy groups, searching for clouds of neutral hydrogen and by comparing the observations to numerical models for galaxy formation in ΛCDM cosmology and models of galaxy interactions.

Most galaxies within 7 Mpc of the Milky Way are located in a few galaxy groups (Karachentsev et al., 2003, 2004) which lie not randomly on the sky, but instead on one or two “filaments” on the super-galactic plane (de Vaucouleurs, 1953; Fouque et al., 1992). This formation of galaxies and galaxy groups along filaments is predicted by ΛCDM cosmology (Silk, 1990). An outstanding question in galaxy formation is whether remnants of galaxy formation are still visible in the local universe (Westmeier et al., 2007; Chynoweth et al., 2008, 2009). It is believed that both tidal effects and accretion along dark matter filaments contribute to the observed properties of galaxy groups (Yun et al., 1994; Thilker et al., 2004; Westmeier et al., 2007; Chynoweth et al., 2008; Zitrin & Brosch, 2008). The contribution of both effects likely varies with local environment within a filament.

In order to understand these observations we compare the statistics of HVCs with predictions of a number of authors concerning detection of dark matter sub-haloes through neutral hydrogen by making large angular area, high sensitivity observations with the Robert C. Byrd Green Bank Telescope (GBT).

In this dissertation I first outline the basic physics of radio astronomical observations of galaxies, through observations of neutral hydrogen. In Chapter 2, I discuss galaxy interactions. In Chapter 3 I present the selection criteria for our GBT observations. In Chapter 4 I describe in detail the GBT observational methods. The results of the GBT observations are presented in Chapters 5 and 6. In Chapters 7 and 8 I present numerical simulations and compare the results of these simulations to our observations. In Chapter 9 I outline plans for future observations. Finally, in Chapter 10 I present the conclusions.

1.1 The 21-centimeter Neutral Hydrogen Line

Hydrogen is by far the most common element in the interstellar medium. In particular, neutral hydrogen (H I) is both very abundant and directly observable. H I is observed in emission at a wavelength of 21 centimeters. Observations of the 21 cm transition of H I can be used to obtain information about kinematics via Doppler shifts and line broadening, gas distribution via imaging, and column densities and masses via line strength.

In galaxies, the neutral hydrogen extends far beyond the optically visible regions of the galaxy. Therefore, it is a good tracer of dark matter and it bears far more telling signs of galaxy interactions than does the stellar (optical) portion of interacting galaxies. Also, the relatively long wavelength means that 21 cm radiation is not scattered as it passes through dusty regions. It is essential to observe neutral hydrogen in order to get a complete picture of a galaxy or system of galaxies. For an excellent illustration of this concept, consider the M81 galaxy group, show in Figure 1. In the optical, the galaxies appear as merely close companions; however, the H I image reveals violent ongoing interactions in the group in the form of massive tidal streams and tails.

See Appendix A for more details on the 21 cm line.

1.2 The Milky Way High Velocity Clouds

Neutral hydrogen observations of the Milky Way and other nearby galaxies reveal a repository of cold gas clouds that do not appear to rotate with the galaxy. Since they

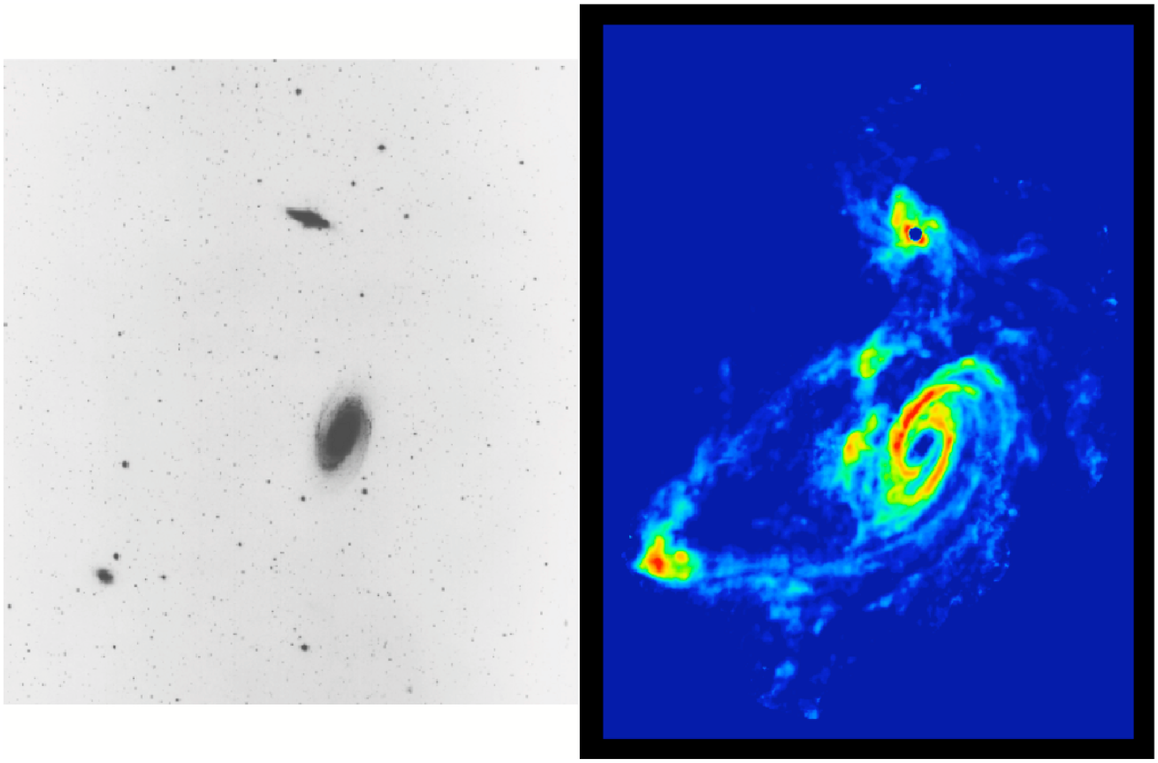

Figure 1: **Left**: Optical image of the M81 galaxy group from the Digital Sky Survey. **Right**: Radio image of the same region in neutral hydrogen emission from Yun (1999). Notice the signs of ongoing interaction in the group clearly visible in the radio image.

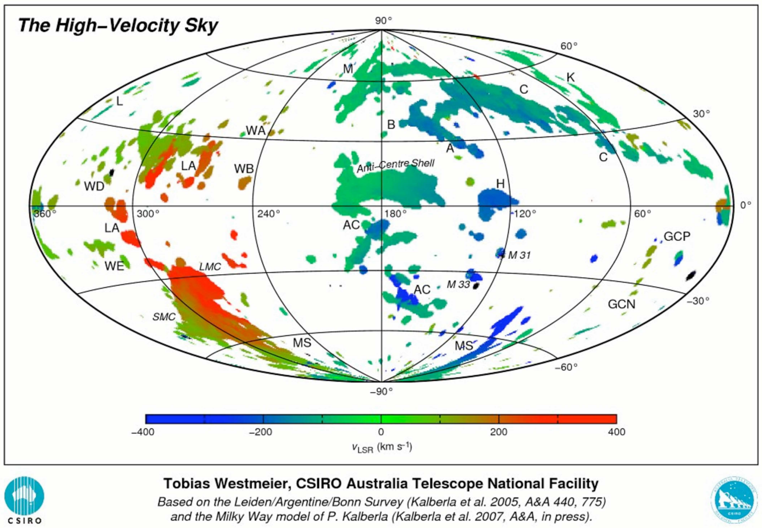

Tobias Westmeier, CSIRO Australia Telescope National Facility
Based on the Leiden/Argentine/Bonn Survey (Kalberla et al. 2005, A&A 440, 775)
and the Milky Way model of P. Kalberla (Kalberla et al. 2007, A&A, in press).

Figure 2: Column density map of all H I with anomalous velocity in the vicinity of the Milky Way, from Westmeier (2009). HVCs are labeled.

are kinematically decoupled from galactic rotation, they are known as High Velocity Clouds (HVCs). In this section, I detail the known properties of these clouds, and discuss the remaining questions.

Milky Way HVCs were first discovered by Muller et al. (1963), after detection of interstellar clouds through absorption line studies prompted systematic searches for H I clouds in equilibrium with a Galactic corona (Wakker & van Woerden, 1997). Subsequent studies have revealed that the Milky Way HVCs are both ionized and neutral, and found in large complexes and as smaller isolated clouds. In neutral hydrogen, the clouds cover nearly 40% of the sky (Wakker & van Woerden, 1997; Lockman et al., 2002). In ionized gas, the clouds cover as much as 85% of the sky (Shull et al., 2009). In total, these clouds make up as much as 10% of the total H I mass of the Milky Way (Wakker & van Woerden, 1997). An all-sky map of high-velocity H I is shown in Figure 2.

1.2.1 HVC Characteristics: Structure

HVCs have a variety of physical sizes and structures. As many as 20 % of HVCs have a distinct cometary or head-tail physical structure (e.g., Brüns et al. (2000); Putman et al. (2002)). These are observed to have a dense core surrounded by an envelope of diffuse H I . Figure 3 shows a HVC with head-tail structure. This shape is attributed to ram pressure in the interaction of the HVC with the hot Galactic corona (Quilis & Moore, 2001). Since the HVCs with this cometary structure are small in angular size, they are often referred to as Compact High Velocity Clouds, or

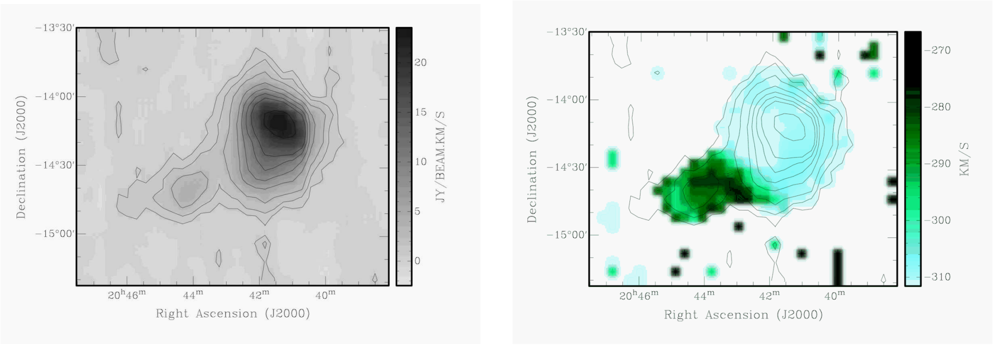

Figure 3: Milky Way HVC with head-tail structure from the catalog of Putman et al. (2002). Left: H I column density. Right: H I velocity field. This type of structure is caused by ram pressure from the hot Galactic corona. Images via http://www.astro.columbia.edu/∼mputman/Erik/web-content/Frames.html.

CHVCs (Westmeier et al., 2005a). The large HVC complexes are made up of many cores, and tend to have a linear shape (Wakker & van Woerden, 1997).

1.2.2 HVC Characteristics: Velocity

In the Milky Way, HVCs are usually defined by their velocity. Generally, a cloud is categorized as a High Velocity Cloud if its velocity deviates by more than 50 km s^{-1} from the range allowed by a simple model of differential galactic rotation (Wakker, 1991).

Many HVCs have a distinct internal velocity structure, illustrated in Figure 3. The head-tail HVCs discussed in the previous section usually show a velocity gradient as well, with the higher density head moving at a faster pace than the tail. These HVCs also show a gradient in velocity dispersion, with both a broad and a narrow component comprising the line profile. The "narrow" component is found within the core of the HVC, and the broad component arises from the envelope or tail. In cloud complexes, there are many cores surrounded by an envelope, and each core exhibits a narrow line profile.

These features can arise from many factors, such as motions of the gas within the cloud in the form of turbulence or bulk motion. The prevailing mechanism causing velocity gradients is thought to be the same mechanism responsible for the core-envelope physical structure —ram pressure from the cold, pressure-confined cloud interacting with the hot (10^6 K) Galactic halo. The cloud, then, would have a thermal structure corresponding to the velocity structure, with a warm ($T \sim 10^4$ K) and a cool ($T \sim 10^2$ K) component (Wakker & van Woerden, 1997).

1.2.3 HVC Characteristics: Distance and Mass

Measurement of many physical properties of H I gas is dependent on an accurate value for distance. For example, mass scales as D^2, size as D^1, and density and pressure as D^{-1}, where D represents distance (Wakker & van Woerden, 1997). Unfortunately, the distances to the clouds in our galaxy are very difficult to measure. HVCs are starless, so none of the traditional methods for measuring the distance to a star can be used. The clouds' anomalous velocities and extraplanar positions make it impossible to use a model of disk rotation to determine their distances. The best that can be done is to use stellar absorption lines to determine upper and lower distance limits for a cloud (Schwarz et al., 1995; Wakker & van Woerden, 1997). In order to determine the upper distance limit, absorption in the spectrum of a star at the velocity of the cloud must be detected in a star in the line-of-sight of the cloud. For a lower distance limit, a significant non-detection of the absorption line in a star in the line-of-sight is required. Many attempts have been made to measure the distances of clouds in the Milky Way using stellar absorption (see, e.g., Schwarz et al. (1995); van Woerden et al. (1999b); Ben Bekhti et al. (2006)). These studies have placed cloud distances in the range of 5-10 kpc above and below the disk (Barentine et al., 2008). Because background stars are required for this method of distance measurement, only clouds that are relatively close to the disk can be measured. Some Milky Way HVCs may reach distances much further than 5-10 kpc.

Given the factor of two or more uncertainties in distance to the HVCs, their masses are estimated to range from $\sim 10^4$ $M_\odot$ for CHVCs (Westmeier et al., 2005b) to $\sim 10^6$ $M_\odot$ for the large complexes (Barentine et al., 2008). The Magellanic Stream is the most massive HVC, with an estimated mass of $\sim 2 \times 10^8$ $M_\odot$ (Putman et al., 2003).

1.3 Galaxies and Galaxy Groups

Possible analogues to the Milky Way clouds have been found around nearby galaxies including M31 (Thilker et al., 2004), M33 (Grossi et al., 2008), and others (van der Hulst & Sancisi, 1988; Miller et al., 2009; Hess et al., 2009). An advantage to studying H I clouds in external galaxies is that there are many robust methods for measuring the distance to a galaxy, so the distance to any associated H I cloud is known much more accurately. Additionally, the projected distance between a cloud and galaxy is easy to measure for extragalactic H I clouds.

The best-studied external HVC system in an isolated galaxy is that of M31.

Around the galaxy, Westmeier et al. (2008) found a population of H I clouds with properties consistent with those of Milky Way HVCs. The M31 clouds have typical H I masses of 10^5 $M_\odot$. The system of HVCs reaches a distance of 50 kpc from the M31 disk.

However, galaxies in low-density environments like M31 are rare. Galaxies are most commonly found in groups (e.g.Geller & Huchra (1983); Tully (1987); Eke et al. (2004); Tago et al. (2008)), so groups are logical environments in which to search for H I clouds. One H I cloud search of galaxy groups has been done – Pisano et al. (2007) searched a sample of loose groups that are Local Group analogs. They did not find any H I clouds, but used their observations to set the constraint that H I clouds should be on average clustered within 90 kpc of group galaxies, with an average mass of 4×10^5 $M_\odot$.

1.4 What is the Origin of H I Clouds?

There are several proposed theories for the source of H I clouds. Broadly, they consist of two classes: those that invoke a galactic plane origin and rely on dynamics to remove the gas from the disk, and those that invoke an extraplanar origin and tie the dynamics to large scale structure. Although it may seem that these different formation scenarios are at odds with one another, it is likely that several processes work in tandem to generate a set of HVCs in a galaxy halo. These processes are described below.

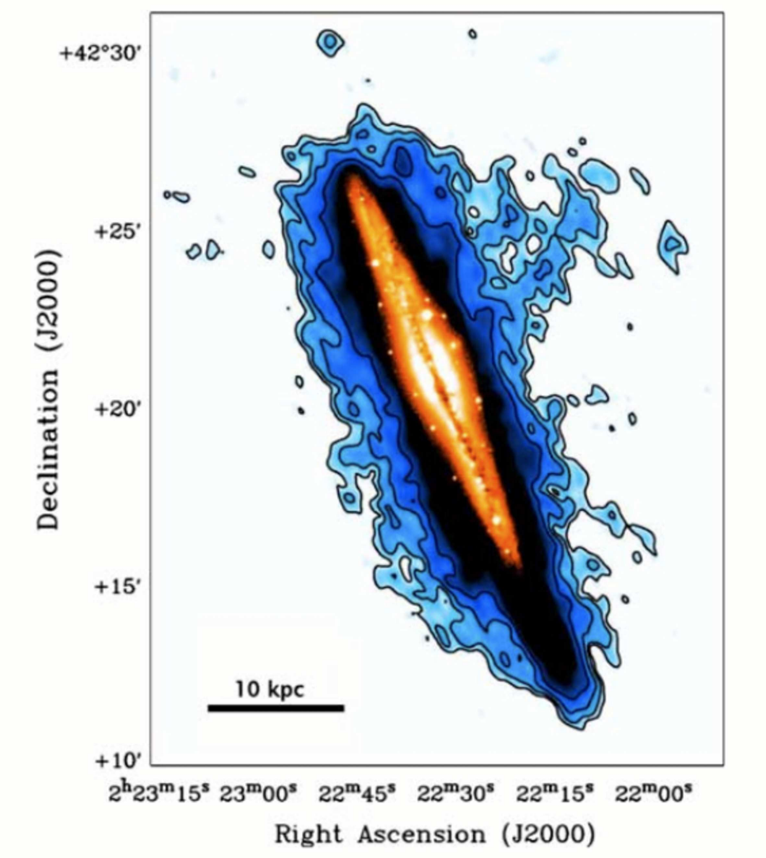

Figure 4: Optical DSS image (red) and total H I map (contours + blue shade) of the edge-on galaxy NGC 891 from Oosterloo et al. (2007) via Sancisi et al. (2008). The extraplanar H I gas in this map is at least partly associated with a galactic fountain, particularly the plume in the northwest (upper right).

1.4.1 Galactic Fountain

In a galactic fountain, gas is blown out of the disk by a supernova outburst, after which it cools, condenses and rains back onto the disk as a galactic fountain (Shapiro & Field, 1976; Bregman, 1980). An example of H I gas in NGC 891 associated with a galactic fountain is shown in Figure 4.

The galactic fountain model for HVCs is supported by the existence of a hot (10^6 K) galactic corona with a scale height of a few kpc, detected in x-rays around galaxies (e.g., Strickland et al. (2004)). This corona is supplied with gas by supernovae explosions from the disk, and radiative cooling causes the formation of H I clouds through thermal instabilities (Shapiro & Field, 1976; Bregman, 1980). Semi-analytic models of this phenomenon by Bregman (1980) and Fraternali & Binney (2006) have successfully reproduced the spatial distribution of HVCs around galaxies, but fail to match HVC velocity distribution. Models of a galactic fountain also predict an outflow of gas that is not observed (Fraternali & Binney, 2006).

Although galactic fountains most certainly exist at some level in all star-forming galaxies, not all observed H I clouds can be produced through a fountain. In particular, the galactic fountain model fails to explain H I clouds further than a few kpc from the disk of a galaxy, beyond the extent of the hot galactic corona. In addition, recent models suggest that the formation of H I clouds via thermal instabilities in the galactic corona may not be possible, depending on the structure of the corona and the sizes and distances of the H I clouds in question (Binney et al., 2009).

1.4.2 Galaxy Interactions

Galaxy interactions may generate HVCs through a combination of tidal stripping, shock heating and subsequent cooling (Chynoweth et al., 2008). In the Milky Way, the Magellanic Stream is a prime example of this phenomenon. As discussed in Section 2.3.1, galaxy interactions draw gas out into tidal tails. One possible source of H I clouds far from galaxy disks is leftover fragments of these tidal tails. Another HVC formation channel related to galaxy interactions is that during minor mergers, gas

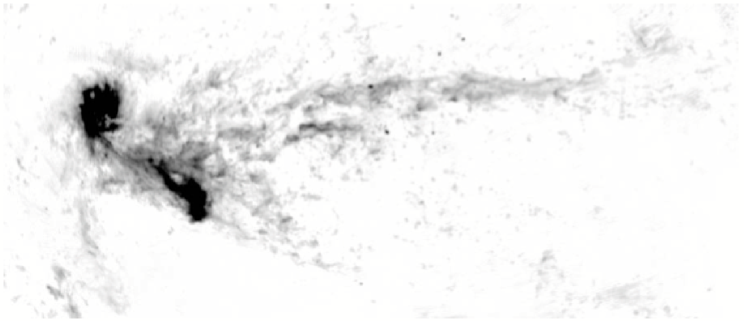

Figure 5: Column density map of the H I in the Magellanic Stream from Putman et al. (2003). This is an example of a Milky Way HVC most likely generated by the interaction of the LMC, SMC, and Milky Way. In this figure the LMC and SMC at the left of the figure, and the Magellanic stream extends to the right.

may be stripped out of the satellite galaxy and be observed as H I clouds.

1.4.3 Dark Matter Halos

HVCs may be the H I tracers of a population of $10^7 - 10^{10} M_\odot$ dark matter halos (Kravtsov et al., 2004). In this case, the gas from these small satellites may also be stripped by the hot halo gas into a long stream of complexes (Putman et al., 2003).

Cosmological simulations based upon the accepted paradigm of ΛCDM (Cold Dark Matter) cosmology, such as the Via Lactea II simulation of Diemand et al. (2008), consistently predict a high degree of dark matter substructure. This aspect of simulations is not well-matched to observations–for instance, the Milky Way is observed to have a factor of at least 4 fewer satellites (in the form of dwarf galaxies) than predicted by simulations (Simon & Geha, 2007). One possible solution to this "missing satellites problem" could be the High Velocity Clouds, if the HVCs are

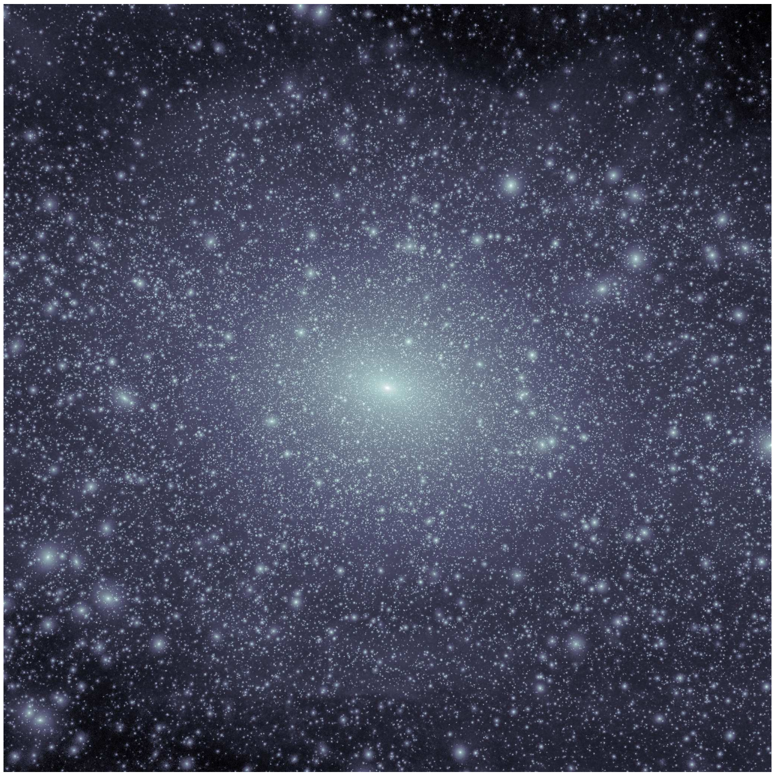

Figure 6: The Via Lactea II simulation, showing the dark matter satellites predicted by ΛCDM cosmology. These satellites may host H I gas and be observed as HVCs. This figure shows the predicted dark matter density at z=0 for an 800 kpc cube. The bright halo in the center is a Milky-Way sized halo, and each other halo is a dark matter satellite.

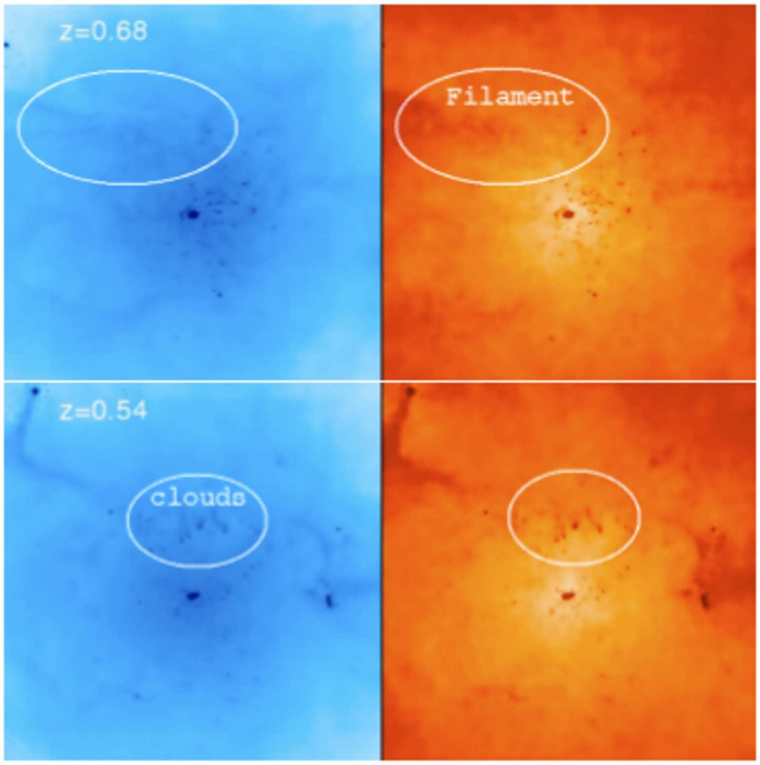

Figure 7: Cold-mode gas accretion from Kereš & Hernquist (2009). Some of this cold accretion may be seen as H I clouds. Left: projected density. Right: projected mass-weighted temperature. The box is $200h^{-1}$ kpc on a side and $100h^{-1}$ kpc thick. Clouds and filaments observable as H I are labeled.

situated within dark matter halos. However, there are still not enough clouds observed to supply the predicted number of satellites, and the clouds that are observed do not have the expected spatial distribution of dark matter halos (Chynoweth et al., 2008, 2009).

1.4.4 Cold Accretion

The clouds could also be a result of instabilities in a hot halo that causes the gas to cool in clumps and fall toward the galactic midplane (Maller & Bullock, 2004; Kereš

& Hernquist, 2009). In this case, HVCs are cold, pressure-confined clouds without an associated dark matter halo (Kereš & Hernquist, 2009). These are formed via Rayleigh-Taylor instabilities when a density inversion develops as cold gas is accreted along filaments feeding into a galaxy filled with hot halo gas.

This scenario is supported by the kinematics of the Milky Way HVC system, which imply significant inflow (Mirabel & Morras, 1984; Simon et al., 2006; Wakker et al., 2007). For example, analysis of HVC Complex C shows a mass inflow rate onto the Galaxy of 0.1-0.25 $M_\odot$ yr^{-1} from Complex C alone (Wakker et al., 2007). Additionally, some extragalactic HVCs appear to represent inflowing gas, such as in the case of NGC 2403 (Fraternali & Binney, 2006). In order to sustain star formation, galaxies must be replenished with fresh gas—for the Milky Way, the required accretion rate is 1 $M_\odot$ yr^{-1}. Numerical simulations show that this gas may arrive via accretion along dark matter filaments (Kereš et al., 2005). Gas accretion along filaments appears to happen in two modes, a "hot" ($T \sim 10^6$ K) and a "cold" ($T < 10^5$ K) mode. A model of this process is shown in Figure 7. The cold mode of accretion, where gas is not shock heated to the halo virial temperature as it falls in, is of primary relevance to H I studies, since some cold-mode accretion gas may appear as H I (Kereš & Hernquist, 2009).

1.5 H I Gas in the Cosmic Web

In addition to the HVC phenomenon, large scale structure may have an H I component. Both cosmological simulations and observations show that matter is concen-

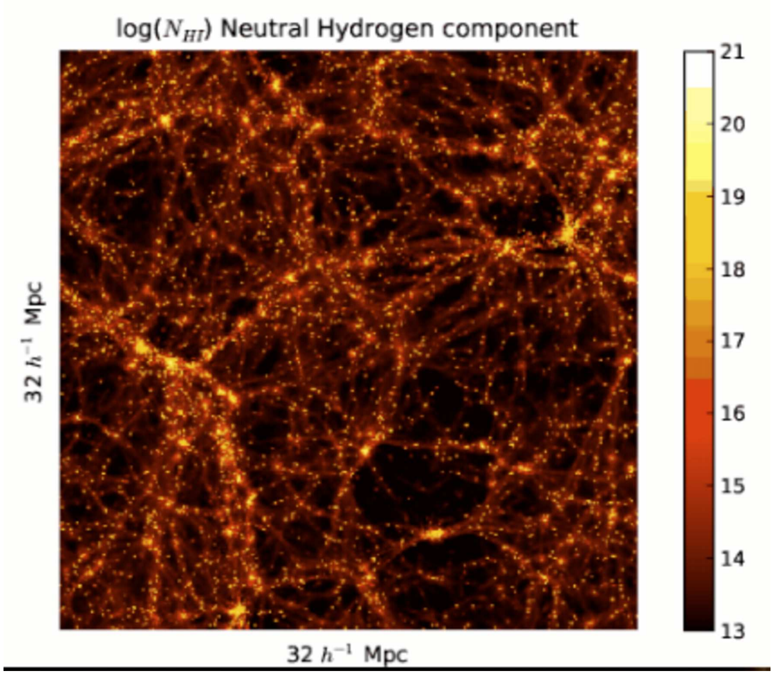

Figure 8: Projected H I column density in the cosmic web to a distance of 32 h^{-1} Mpc, from the simulation of Popping et al. (2009).

trated in filamentary structures that grow from dark matter density perturbations after the Big Bang. This filamentary structure is known as the “cosmic web”. Galaxies are the densest and most luminous structures within this cosmic web, and therefore the most well-studied, but the filaments between galaxies can contain significant amounts of matter as well.

In fact, the consensus is that roughly 60% of the baryons reside not in individual galaxies, but in the intergalactic medium (Fukugita et al., 1998; Fukugita & Peebles, 2004; Cen & Ostriker, 1999; Davé et al., 1999, 2001; Cen & Ostriker, 2006; Dolag et al., 2006; Davé & Oppenheimer, 2007). At high redshift, most of the baryonic mass is in the Lyman-α forest (Fukugita et al., 1998; Fukugita & Peebles, 2004), while at low redshift, these baryons are as yet undetected. The missing baryons are predicted to be composed of warm and cold components (Cen & Ostriker, 1999; Davé et al., 1999; Cen & Ostriker, 2006; Davé & Oppenheimer, 2007; Popping et al., 2009), and are thought to trace the cosmic web. However, both of these are extremely difficult to detect due to their diffuse, faint nature. The warm gas component is undetectable with current x-ray instrumentation, although future x-ray telescopes such as the International X- Ray Observatory (IXO), hold promise for detecting this Warm-Hot Intergalactic Medium, or WHIM (Bregman et al., 2009). The cold gas component of the cosmic web remains undetected as well. Only one instance of cosmic web H I emission has been tentatively observed so far; in the filament joining M31 and M33, significant H I is seen in both emission and absorption by Braun & Thilker (2005). However, this gas may also be due to a previous interaction between the galaxies (Bekki, 2008). Therefore, the cosmic web is still largely mysterious in terms of gas content, structure, and kinematics.

Recent numerical simulations predict that low density, cosmic web H I gas traces the cosmic web with a high filling fraction, and could be detectable in emission for $N_{HI} \leq 10^{17.5}$ cm^{-2} (Popping et al., 2009). A snapshot of the predicted H I column density distribution is shown in Figure 8. With current radio instrumentation, $N_{HI} \leq 10^{19}$ cm^{-2} has long been considered a practical observational limit that places surveys for cosmic web H I emission out of observational reach. However, with large single-dish telescopes, column density sensitivities of $N_{HI} \sim 10^{18}$ cm^{-2} over large areas are possible. Although this column density sensitivity is still too large to meet the predictions for diffuse cosmic web H I emission, current observations may still be able to constrain the high end of the cosmic web H I mass function in this unexplored region, and determine if there are any dense clouds of H I in the cosmic web.

CHAPTER II

QUANTIFYING GALAXY INTERACTIONS

Although in some cases it is obvious that a galaxy interaction is taking place, it is not always a simple matter to determine whether a particular galaxy has undergone a recent interaction. Determining the relative strength or intensity of interactions is even more difficult. Usually, H I provides the strongest evidence of recent galaxy interactions. However, since we are studying the correlation of H I properties with interaction level, we need an independent metric for this study. There are a number of other parameters and phenomena that can be indicators of galaxy interactions; these are described in this chapter. We must consider that phenomena that are sometimes induced by interactions are not a guarantee of interactions. Furthermore, it is not clear how much weight to give each factor. However, with these caveats, a combination of these parameters can be used as a guide for quantifying the level or probability of interactions in a galaxy group. Section 2.6 describes a possible parameterization of the phenomena described below, with equations for "interaction indices" that are a first step towards quantifying galaxy interactions.

2.1 Density

Dense groups are more likely to interact than loose groups, as the galaxies will encounter one another more often. Since the masses of galaxy groups are not easy to constrain, a mass density cannot be calculated accurately. A volume density is also difficult to calculate, but a projected number density can be calculated and give a rough guide to the density of a group. A conservative estimate for the virial radius of a typical galaxy group is approximately 1 Mpc; therefore, in order to calculate this parameter we calculate the number density of galaxies within ± 1 Mpc from the most massive galaxy in each group.

2.2 Velocity Dispersion

The trajectories of galaxies in a group will strongly influence the likelihood and strength of interactions. Numerical simulations show that the length and mass of tidal tails generated by an interaction depends strongly on initial orbital parameters of the encounter. Specifically, close and slow approaches produce tidal tails and bridges, whereas fast encounters do not (Barnes & Hernquist, 1992). In order to quantify the overall trajectories of group galaxies in relation to interactions, a useful metric is the velocity dispersion of a group. For this study, we use the standard deviation of group galaxy velocities.

2.3 Morphology

Various morphological features may be induced by galaxy interactions. They are described below. Although spiral, barred, and elliptical galaxies can all be related to interactions, the most reliable morphological indication of interactions are tidal bridges and tails. Therefore, to include this parameter we calculate the number of group galaxies exhibiting clear tidal features.

2.3.1 Tidal Bridges and Tails

Long, thin tails of stars and gas extending far beyond the galaxies are often seen in strongly interacting systems. As two galaxies approach, tidal forces strip material from the far sides of the rotating disks and draw it out into long streams. Between interacting galaxies, a broad bridge across which gas may be transferred is observed. Examples of tidal tails and bridges from both observations and numerical simulations are shown in Figure 9.

Theory has predicted these structures since early work on galaxy interactions. Numerical simulations have been successful in reproducing tidal features using only gravitational forces (Toomre & Toomre, 1972), and it is found that the occurence of tidal tails depends strongly on the trajectories of interacting galaxies. Tidal tails and bridges are interesting to study not only as relics of past interactions, but also as continually evolving structures. They may form structures such as dwarf galaxies through self-gravity (Barnes & Hernquist, 1992), although dissipation may play an important role in the formation of tidal dwarfs as well (Wetzstein et al., 2007).

2.3.2 Spiral Arms

Spiral arms are ubiquitous features of galaxy morphology. Spirals are the most common type of giant galaxy, and they produce most of the optical luminosity in the local universe (Sparke & Gallagher, 2000). A famous example is M51, a spiral galaxy which is clearly interacting with a barred spiral/irregular companion galaxy NGC 5195; see Figure 11.

Spiral arms are understood as density waves propagating through the stars and gas in the galactic disk. It is thought that one possible driver of these waves is perturbation by another galaxy. Simulations have had success in inducing spiral arms via forces from a nearby perturber (Barnes & Hernquist, 1992; Oh et al., 2008; Dobbs et al., 2010). A simulation of two interacting galaxies where spiral structure appears is shown in Figure 10, and a simulation of the specific case of M51 is shown in Figure 11.

It is important to note, however, that not every spiral galaxy is obviously interacting, and models have shown that spiral arms can appear in an isolated galaxy (Barnes & Hernquist, 1996). Therefore, spiral morphology is not a good metric for this study.

2.3.3 Bars

Large scale bars of gas and dust that stretch across the center of a galaxy are quite common; they are found in about half of galaxies in the local universe. Stars in barred galaxies stay within the bar (as opposed to the density waves that comprise spiral arms). Examples of barred galaxies from numerical simulations and observations are shown in Figures 10 and 12.

Just as with spiral arms, interactions are not the only possible cause of a galactic bar. However, it is thought that bars may be induced by the gravitational instability caused by a companion galaxy or merger, much in the same way that spiral arms are caused. Simulations of galaxy interactions can produce a large-scale bar (Noguchi, 1988; Gerin et al., 1990; Barnes & Hernquist, 1996). Since bars are common in both isolated and interacting galaxies, barred morphology is not a good metric for this study.

2.3.4 Elliptical Galaxies

Elliptical galaxies can also show many signs of galaxy interactions. It is thought that ellipticals may be the remnant left behind after the violent processes involved with an ongoing interaction or merger have subsided. Simulations of galaxy mergers show that remnants tend to be ellipticals once the galaxies have merged and relaxed (Mihos & Hernquist, 1996). Upon close inspection, even galaxies that appear to have an undisturbed morphology are seen to have small-scale structure such as loops, shells, and bubbles which may be the last stages of relaxation after a merger (Barnes & Hernquist (1992), Mihos & Hernquist (1996)).

Although the signs of mergers' effects on elliptical galaxies are not immediately obvious, they do tend to show signs of external influence. For example, ellipticals have been observed to have distinct cores, with metal rich, young stellar populations, that are rotating counter to the rest of the galaxy (Emsellem et al., 2007). This has been attributed to mergers via tidal disruptions which cause gas to settle in the center of the merger remnant and form stars (Bender & Surma, 1992), or the accretion of a counter-spinning dwarf satellite galaxy that transfers its angular momentum to the primary galaxy (Barnes & Hernquist, 1992).

Since elliptical galaxies are thought to be an indication of past interactions that have since relaxed, we will not include them as an indicator of ongoing interactions.

2.4 Star Formation

Galaxies are often observed to have vigorous bursts of massive star formation, producing stars at a rate of $\sim$ 10-100 $M_\odot$/yr (Lacey, 1989). These can be caused by interaction or merger with another galaxy; indeed, many interacting systems show indications of starburst activity such as high levels of Hα emission and high infrared luminosity (e.g., Sanders et al. (1988); Knapen & James (2009)).

As two galaxies approach, the gas from each galaxy loses energy and angular momentum and sinks to the center of the galaxes. As the gas collides it is compressed to high densities; these dense gas regions are prime areas for star formation. Starbursts are seen globally, across the entire galaxy (Mihos & Hernquist, 1996), due to shocks and collisions between clouds of gas. Starbursts are also observed in localized areas, as in the case of nuclear starbursts (Schinnerer et al., 2006), or between two approaching galaxies (Thronson et al., 1989).

Although interactions can certainly create favorable conditions for triggering a starburst, not all interacting systems show enhanced star-forming activity. The effect of orbital parameters and internal structure of the galaxies play an important part in the details of gas dynamics leading to star formation. The mass ratio of the merging galaxies also strongly affects the resultant star formation; Cox et al. (2008)

find that the strongest starbursts occur when the masses of merging galaxies are close to equal. The most efficient inflows of gas tend to occur in coplanar major mergers. The structure of the merging galaxies determines the timescale for starburst activity; galaxies with a dense central bulge tend be more stable to perturbations caused by interaction (Mihos & Hernquist, 1996; Cox et al., 2008). Only when two such galaxies are in the final stage of merging are the bulges disrupted enough to allow strong inflows of gas.

Clearly, the detailed relationship between galaxy interactions and star formation is not well understood. However, in general it is found that the star formation rate (SFR) is increased in merging spiral galaxies (e.g., Kennicutt & Keel (1984); Keel et al. (1985); Bushouse (1986); Hummel et al. (1990); Darg et al. (2010)). Therefore, we will use the relative star formation rates in our observed sample as an indicator of ongoing galaxy interactions.

The star formation rate (SFR) can be directly calculated from Hα luminosity (Kennicutt, 1998), which is readily available for nearby galaxies. We will use average SFR as an indicator of higher likelihood of recent or ongoing interactions in a group. SFRs are calculated using:

$$\mathrm{SFR}(M_{\odot} yr^{-1}) = 7.9 \times 10^{9} L(H\alpha) \tag{1}$$

Where L(Hα) is in units of ergs s^{-1}. For Hα luminosities, we use the Galactic extinction-corrected values from the 11HUGS study of Kennicutt et al. (2008). Caveats in this technique vs. IR in Dopita et al. (2002).

2.5 AGN Activity

Some galaxies have an extremely bright, extremely compact core. Such galaxies are known as active galaxies, and their cores are referred to as Active Galactic Nuclei, or AGN. AGN are seen to radiate strongly across the entire electromagnetic spectrum; normal galaxies do not radiate strongly in the radio, X-ray, or γ-ray regimes. AGN luminosities are higher than can be provided through stellar sources in such a compact region; some AGN reach luminosities of over 10^{12} $L_\odot$ (Sparke & Gallagher, 2000) in an emitting region approximately the size of the solar system. There are many classes of AGN, including Seyfert galaxies, quasars, blazars, and radio galaxies.

These different types of active galaxies are distinguished by different observed properties, such as characteristics of their spectra, degree of polarization, and variability. For instance, Seyfert galaxies show optical emission lines, radio emission, and X-ray emission. Within the Seyfert category, Seyfert 1 galaxies exhibit both broad and narrow emission lines, while Seyfert 2 galaxies have only narrow lines (Binney & Merrifield, 1998).

It is thought that most of the classes of AGN are actually the same physical phenomenon, but different orientations give rise to different observed characteristics (Urry & Padovani, 1995). A diagram of the currently accepted picture of an AGN is shown in Figure 13. It is well-established that most, if not all, galaxies have a super-massive black hole (SMBH), as no other known phenomena can provide the observed luminosity in such a compact region (Gebhardt et al., 2000; Ferrarese & Merritt, 2000). This SMBH is the primary engine for an active galaxy.

If the currently accepted schematic of an AGN holds true, a huge amount of gas is required in nuclear regions to provide enough mass to account for the observed luminosity. There are various physical mechanisms by which gas loses angular momentum and falls to the center of a galaxy, including gravitational torques, viscous torques, and hydrodynamical torques or shocks (Binney & Tremaine, 1987). Galaxy interactions and mergers provide efficient mechanisms for funneling gas to the nucleus of a galaxy (Mihos & Hernquist, 1996).

There are links between galaxy interactions and the onset of nuclear activity in galaxies in both observations (Sanders et al., 1988) and simulations (Springel et al., 2005). Many active galaxies show signs of interaction and merger such as disturbed morphology, particularly in H I (Kuo et al., 2008). Seyfert nuclei are found preferentially in interacting galaxies (Kennicutt & Keel, 1984; Laurikainen & Salo, 1995). The strongest links between interactions and AGN are found in the systems with the highest luminosity (Bahcall et al., 1997).

To include this parameter we calculate the number of group galaxies classified as any type of AGN in NED[1].

2.6 Interaction Indices

All of the factors described above fall into two categories. One category are indicators of likelihood or potential for interaction, including density of galaxies and velocity

---

[1] NASA/IPAC Extragalactic Database (NED) which is operated by the Jet Propulsion Laboratory, California Institute of Technology, under contract with the National Aeronautics and Space Administration, http://nedwww.ipac.caltech.edu/

dispersion of the galaxy group. The second category are evidence of past or current interactions, including morphology, star formation, and AGN activity. Therefore we calculate two "interaction indices", described below. Both indices include only those galaxies within ± 1 Mpc of the most massive galaxy in each group. These indices are applied to the sample of galaxy groups studied for this dissertation as well as the Local Group in Chapter 3. Note that the numbers resulting from these calculations are arbitrary; in order to use these indices to rank our observation sample, we have normalized each variable to the maximum for our sample. A robust statistic would need to include a normalization of the indices to some standard and appropriate weighting of each variable. However, for the purposes of this study it is only necessary to determine the interaction indices of the groups relative to one another, so no effort towards normalization or weighting is made.

2.6.1 Interaction potential

The interaction potential index should take the form:

$$\mathrm{IP} = \mathrm{Density} + \mathrm{Velocity} \tag{2}$$

Quantifying each factor, this becomes:

$$\mathrm{IP} = \frac{N}{max(N)} + \left(\frac{\sigma_v}{max(\sigma_v)}\right)^{-1} \tag{3}$$

Where N is the number of galaxies and σ_v is the velocity dispersion of those galaxies. We take the reciprocal of σ_v to account for a high velocity dispersion corresponding to low interactions.

2.6.2 Interaction evidence

The interaction evidence index should take the form:

$$\text{IE} = \text{Morphology} + \text{Star Formation} + \text{AGN Activity} \tag{4}$$

Quantifying each factor, this becomes

$$\text{IE} = \frac{N_{Tidal}}{max(N_{Tidal})} + \frac{SFR}{max(SFR)} + \frac{N_{AGN}}{max(N_{AGN})} \tag{5}$$

Where N_{Tidal} is the number of group galaxies exhibiting tidal tails or bridges; SFR is the average star formation rate of group galaxies, calculated following Kennicutt (1998); and N_{AGN} is the number of group galaxies with AGN.

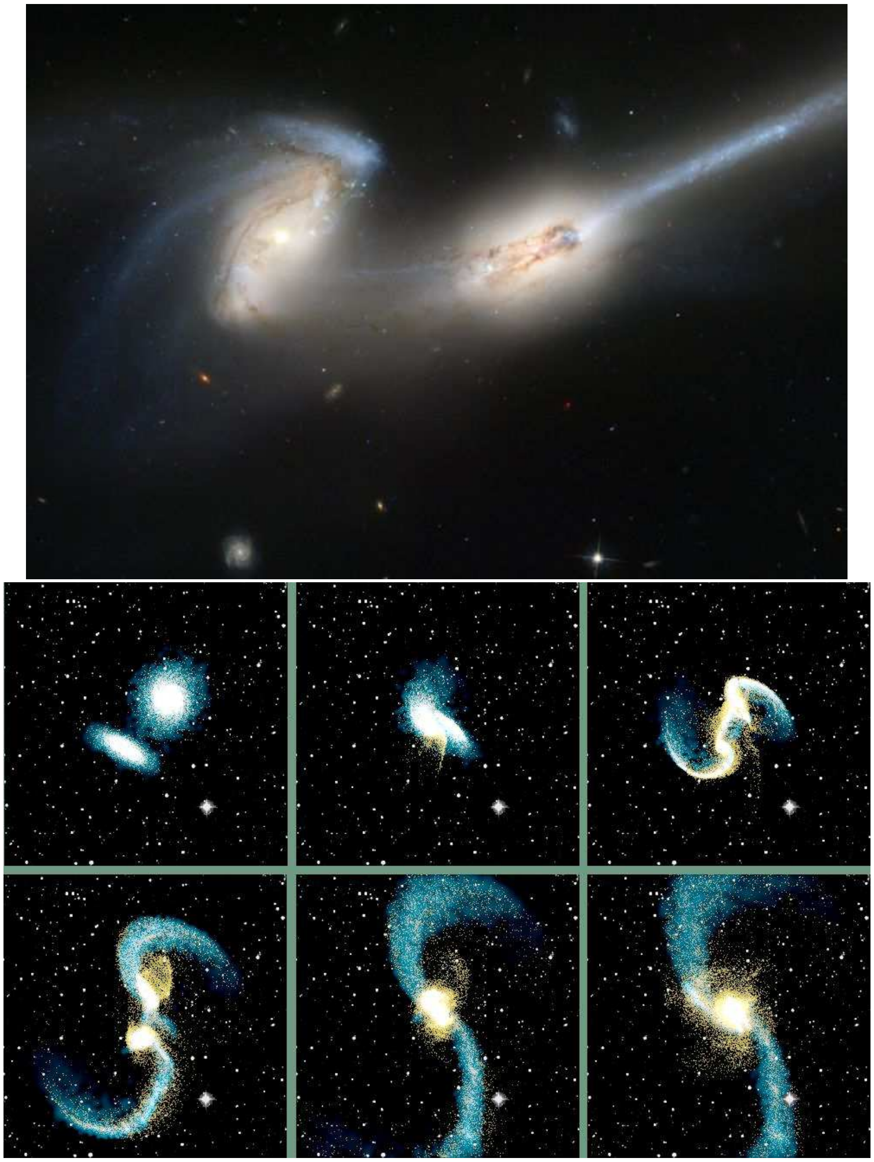

Figure 9: Tidal tails caused by gravitational interaction of two galaxies. **Top**: NGC 4676 (The Mice). Credit: ACS Science & Engineering Team, NASA. **Bottom**: A simulated collision of two disk galaxies. Yellow and white indicate stars, and blue shows the gas. The sequence spans approximately 1 Gyr. Credit: C. Mihos & S. Maxwell, Case Western Reserve University.

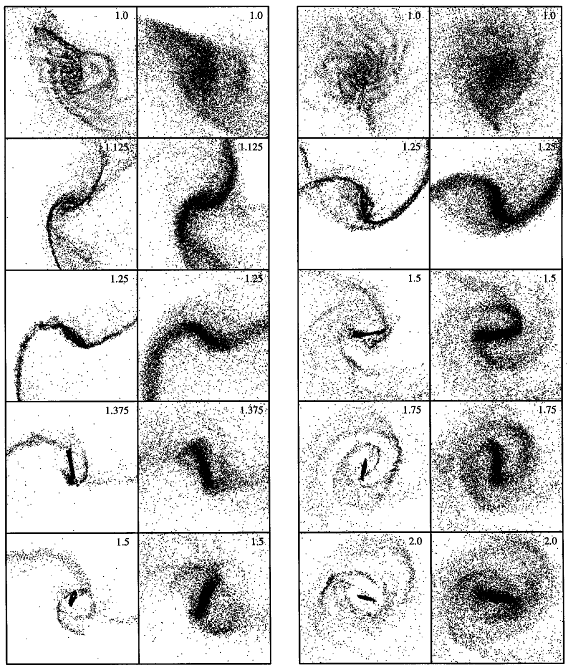

Figure 10: Simulation of two merging disk galaxies by Barnes & Hernquist (1996). Time increases from top to bottom. From left to right, the first two columns correspond to the gas and stars in one galaxy. The next two columns are the gas and stars in the other galaxy in the merger. Note that both galaxies form prominent stellar bars and spiral arms, and gaseous concentrations in the nucleus.

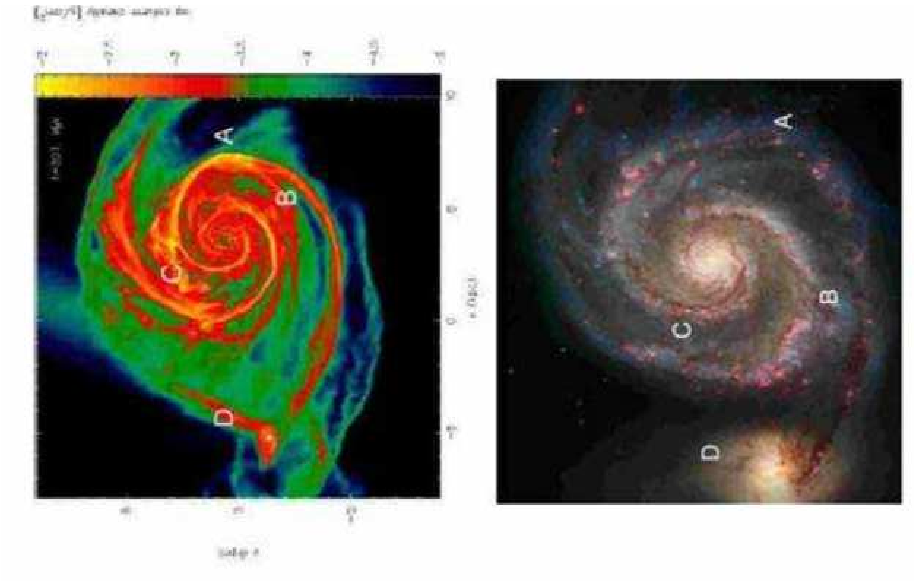

Figure 11: Left: Projected gas column density of simulated M51 and NGC 5195, from Dobbs et al. (2010). Right: Optical image of spiral galaxy M51, with its companion galaxy NGC 5195. Features that match in the observations and simulation are marked. Credit: S. Beckwith (STScI) Hubble Heritage Team, (STScI/AURA), ESA, NASA

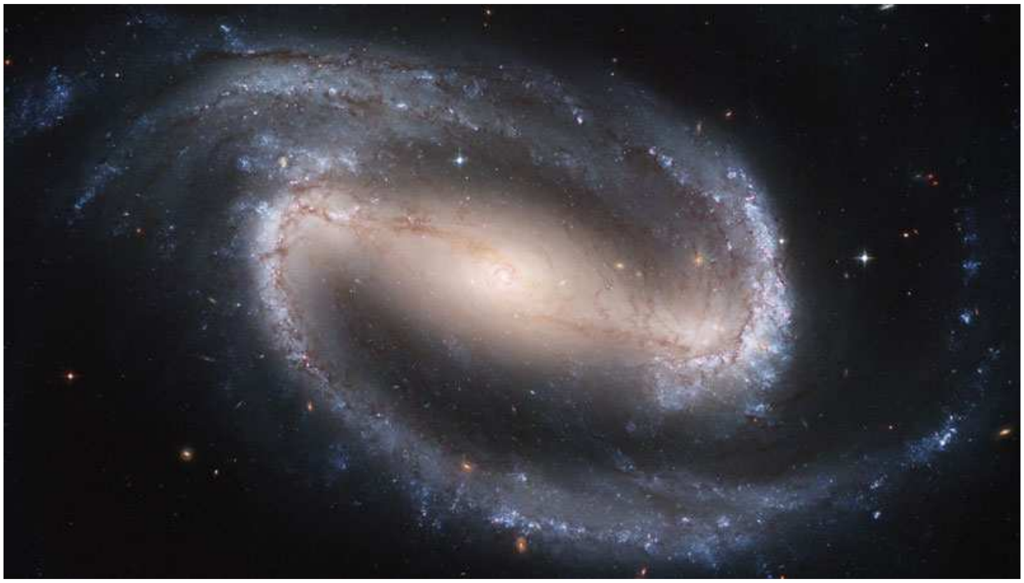

Figure 12: Barred galaxy NGC 1300. Bars may be induced by galaxy interactions. Credit: Hubble Heritage Team, ESA, NASA.

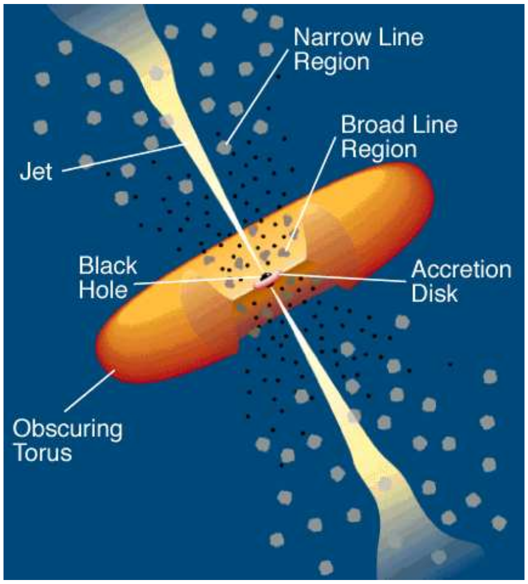

Figure 13: A model AGN from Urry & Padovani (1995). Gas that feeds the AGN may be funneled to the nucleus via disturbances caused by galaxy interaction. The observed characteristics of each class of AGN depend on the angle from which this schematic is viewed.

CHAPTER III

STUDY AND SAMPLE SELECTION

3.1 Study Overview

In order to determine the origins of H I clouds in galaxy groups, we observed five nearby galaxy groups with the 100m Robert C. Byrd Green Bank Telescope (GBT) at the NRAO[1] in Green Bank, West Virginia. We observed a wide angular area and velocity range around each galaxy, and the properties of detected H I clouds were catalogued and compared against simulations.

3.2 Sample Selection

The five galaxy groups were chosen with the following criteria.

1. Galaxy groups must be observable with the GBT. The GBT can observe sources in the declination range $\delta \geq$ -46°.
2. Galaxy groups must be nearby, for adequate angular resolution and sensitivity. We aimed for a maximum group distance of 7.5 Mpc.
3. Galaxy groups must be at least partially distinct from the Milky Way in velocity space to avoid confusion with foreground H I gas. This criterion is difficult to reconcile with (2), so the two closest groups partially overlap with the Milky

---

[1] The National Radio Astronomy Observatory (NRAO) is a facility of the National Science Foundation operated under cooperative agreement by Associated Universities, Inc.

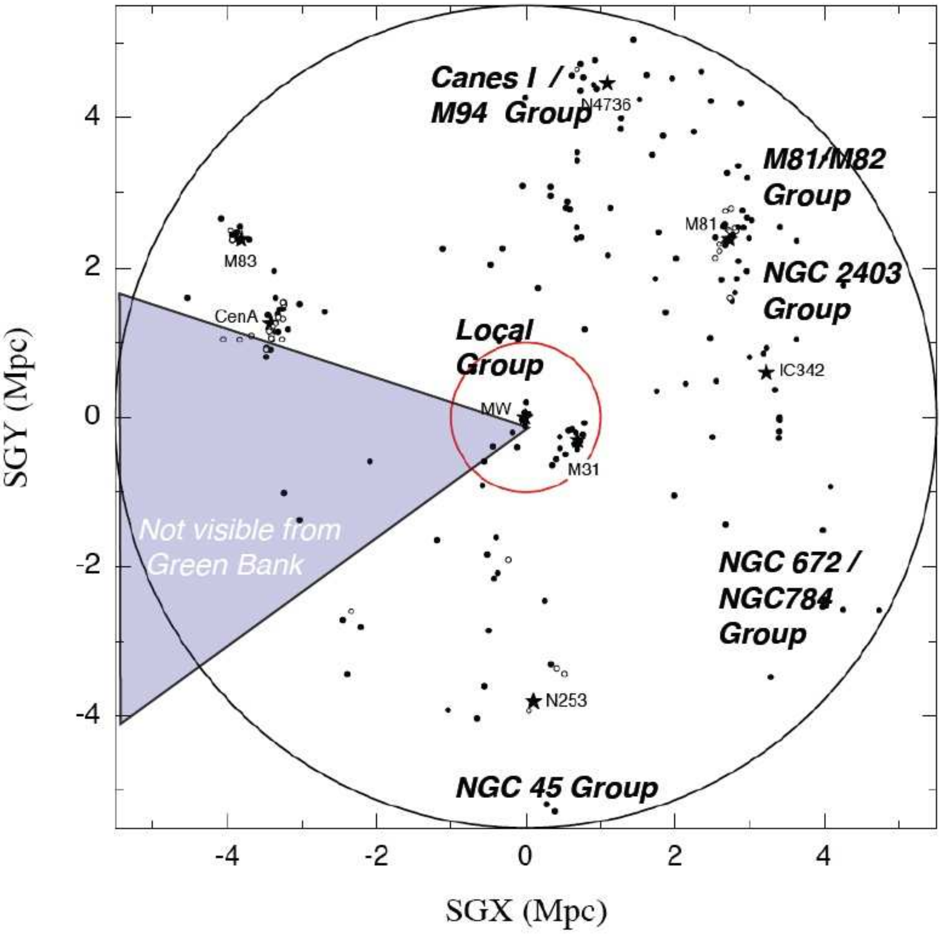

Figure 14: Map of observed galaxy group locations. The gray wedge indicates the declination range not observable from Green Bank.

Way in velocity space.

4. Galaxy groups must span the range in intensity of galaxy interactions.

Numbers 1-3 are easily satisfied. Criteria 4 is essential in order to explore the role of interactions in the generation of H I clouds. We attempted to choose galaxy groups with different levels of galaxy interactions. The galaxy groups observed for this study are described in the next section, and interaction indices are calculated in Section 3.4. Table 1 lists all galaxy groups within 10 Mpc (Fouque et al., 1992; Tully,

Table 1: Galaxy Groups Within 10 Mpc

Name	α (J2000)	δ (J2000)	D (Mpc)	V_{hel} (km s^{-1})
M81	10:10	+69.1	3.7	127
Maffei	03:49	+68.0	3.1	171
Sculptor	00:36	-31.0	2.8	177
NGC 2403	07:43	+66.7	3.7	231
Canes I	12:18	+35.8	4.0	294
M101	14:03	+54.6	7.7	363
NGC 5128	13:25	-41.6	4.3	390
NGC 672	01:51	+27.8	6.1	458
NGC 5194	13:09	+44.0	7.7	466
NGC 3115	10:05	-7.7	9.2	494
NGC 45	00:13	-23.4	6.1	503
NGC 2835	09:14	-23.5	9.2	547
Canes II	12:22	+45.4	9.2	548
NGC 2541	08:12	+49.9	9.2	565
NGC 7640	23:24	+40.9	9.2	589

1987). Galaxy groups observed for this study are listed in bold. Our observations cover 33% of galaxy groups within 10 Mpc.

3.3 Sample Description

3.3.1 M81 Group

The M81 group is one of the closest galaxy groups to the Milky Way, at a distance of 3.5 Mpc. It is comprised of 4 major galaxies (M81, M82, NGC 3077, NGC 2976) and over 40 dwarf galaxies. Although the galaxies are optically undisturbed, H I observations reveal that the galaxies are undergoing strong interactions. Additionally, M82 is an extreme starburst galaxy and many of the dwarf galaxies show morpholog-

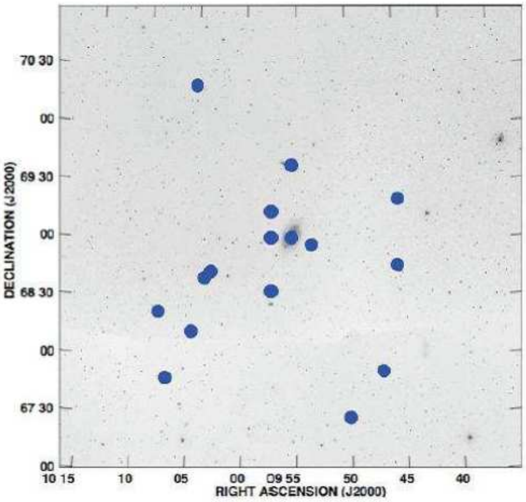

Figure 15: Locations of M81 Group galaxies in blue dots, overlaid on optical DSS image.

ical and kinematic irregularities. Table 2 lists galaxy properties and Figure 15 shows galaxy locations.

3.3.2 NGC 2403 Group

The NGC 2403 group is locate at approximately the same distance as the M81 group. The NGC 2403 group contains the bright spiral galaxy NGC 2403, 3 additional large galaxies (NGC 2366, UGC 4305, UGC 4483), and at least 4 dwarf or low surface brightness satellite galaxies. The NGC 2403 group does not show clear signs of interaction. However, some of the group galaxies show subtle irregularities which may be due to previous interactions between group galaxies. The largest galaxy, NGC 2403, shows a thick, lagging H I layer and a few H I filaments with anomalous velocities, which are similar to the M81/M82 clouds in mass (Fraternali et al., 2002).

Table 2: M81 Group Galaxy Properties

Name	α (J2000)	δ (J2000)	D (Mpc)	V_{hel} (km s^{-1})	Type	f(Hα) (log ergs cm^{-2} s^{-1})
M81	$09^h55^m33.5^s$	69°03‘06“	3.65	-34	SA(s)ab;LINER Sy1.8	-10.31 ± 0.02
Holmberg IX	$09^h57^m32.4^s$	69°02‘35“	2.64	46	Im	-13.07 ± 0.14
BK3N	$09^h53^m48.5^s$	68°58‘09“	4.02	-40	Im	$<$ -15.70
A0952+69	$09^h57^m29.0^s$	69°16‘20“	...	100	...	...
KDG 61	$09^h57^m02.7^s$	68°35‘30“	3.45	-135	dE	-13.41 ± 0.05
M82	$09^h55^m53.9^s$	69°40‘57“	4.55	203	I0;Sbrst HII	-10.09 ± 0.03
NGC 3077	$10^h03^m21.0^s$	68°44‘02“	3.45	14	I0 pec HII	-11.18 ± 0.04
Garland	$10^h03^m42.7^s$	68°41‘27“	3.82	50	Im	...
BK1N	$09^h45^m14.3^s$	69°23‘23“	9.3	571	Im	...
FM 1	$09^h45^m10.0^s$	68°45‘54“	...	...	...	...
BK5N	$10^h04^m40.3^s$	68°15‘20“	3.88	...	dE	...
IKN	$10^h08^m05.9^s$	68°23‘57“	...	...	dSph	...
NGC 2976	$09^h47^m15.6^s$	67°54‘49“	2.83	3	SAc pec HII	-11.19 ± 0.06
U5423	$10^h05^m30.6^s$	70°21‘52“	7.14	347	Im	-12.86 ± 0.05
KDG 64	$10^h07^m01.9^s$	67°49‘39“	3.60	-18	Im	...
KK 77	$09^h50^m10.0^s$	67°30‘24“	...	...	...	...
IC 2574	$10^h28^m22.4^s$	68°24‘58“	3.96	57	SAB(s)m	-11.23 ± 0.07

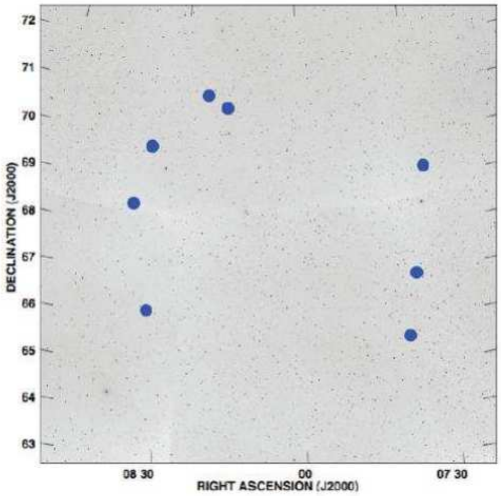

Figure 16: Locations of NGC 2403 Group galaxies in blue dots, overlaid on optical DSS image.

These features may be analogues to Milky Way HVCs, and their origins are similarly unclear. They have been attributed to a combination of outflow from a galactic fountain and accretion from the IGM (Fraternali & Binney, 2006); both of these phenomena may be induced by interactions between group galaxies (Larson & Tinsley, 1978; Sancisi et al., 2008). UGC 4305 has a cometary appearance in H I (Bureau & Carignan, 2002), which may be caused by ram pressure from the intragroup medium. The dwarf galaxy DDO 53 is also kinematically irregular in H I (Begum et al., 2006). The other galaxies in the group appear to be normal. Table 3 lists galaxy properties and Figure 16 shows galaxy locations.

Table 3: NGC 2403 Group Galaxy Properties

Name	α (J2000)	δ (J2000)	D (Mpc)	V_{hel} (km s^{-1})	Type	f(Hα) (log ergs cm^{-2} s^{-1})
NGC 2403	$07^h36^m52.7^s$	65°35‘52“	3.30	131	Sc	-10.25 ± 0.04
DDO 44	$07^h34^m11.9^s$	66°52‘58“	3.19	...	dSph	...
NGC 2366	$07^h28^m55.7^s$	69°12‘59“	3.19	99	IBm	-11.01 ± 0.01
UGC 4483	$08^h37^m03.1^s$	69°46‘44“	3.21	156	BCD	-12.50 ± 0.02
UGC 4305	$08^h19^m06.5^s$	70°43‘01“	3.39	157	Im	-11.28 ± 0.04
KDG 52	$08^h23^m56.2^s$	71°01‘36“	3.55	113	Irr	$<$ -15.30
DDO 53	$08^h34^m08.6^s$	66°11‘03“	3.56	20	Irr	-12.26 ± 0.12
VKN	$08^h40^m11.1^s$	68°26‘11“	...	...	dSph(?)	...

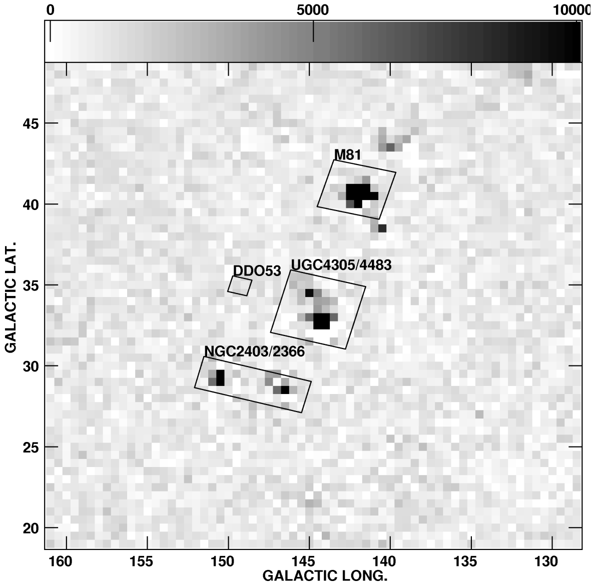

Figure 17: Map of the NGC 2403 and M81/M82 groups along the M81 filament from the Leiden/Argentine/Bonn (LAB) Galactic HI survey (Kalberla et al., 2005), integrated from 107 to 200 km s^{-1}. The grayscale range is 0 to 10 K × km s^{-1}

3.3.3 M81 Filament

The extent of the dark matter and hot gaseous halos of the M81 and NGC 2403 groups are unknown– in fact, the M81 group is sometimes considered to encompass the NGC 2403 group as part of one structure (Begum et al., 2006; Karachentsev & Kaisin, 2007), known as the "M81 Filament" (Karachentsev et al., 2002). The M81 Filament includes the M81 and NGC 2403 galaxy groups and the region between them. It is likely that the linearly shaped set of galaxies is contained within a dark matter filament of the type commonly seen to form in cosmological simulations. Figure 17 shows the M81 Filament, with the M81 and NGC 2403 groups indicated.

If the two groups are indeed part of one group and situated within a dark matter filament, then we may expect to detect both pressure-confined clouds and H I -laced

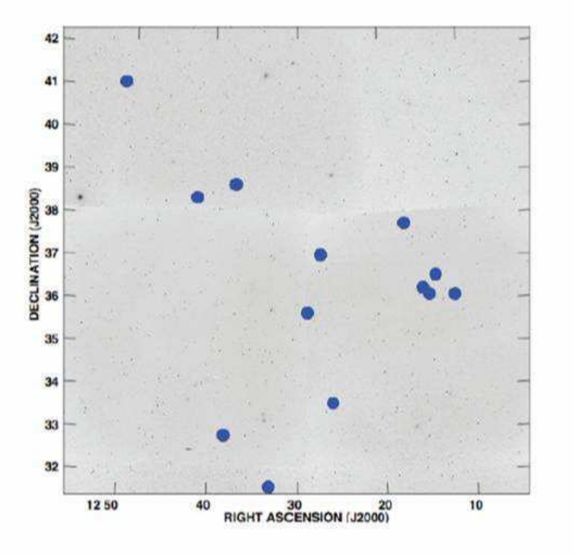

Figure 18: Locations of Canes I Group galaxies in blue dots, overlaid on optical DSS image.

dark matter halos in between the two groups. We observed the entire extent of the M81 Filament in order to enable the treatment of the Filament as one group, as well as considering the M81 and NGC 2403 group separately. With a wide span of velocities and unprecedented sensitivity over such a large area, this campaign was designed to assemble a complete census of the H I clouds generated by all the plausible HVC formation mechanisms. Treating the M81 Filament as one large group also affects the interaction metric. Table 4 lists the properties of M81 Filament galaxies, as well as galaxies in the background that our observations cover.

3.3.4 Canes I Group

The Canes I galaxy group is located approximately 4 Mpc away and contains many galaxies. The Canes I group is a diffuse cloud of galaxies. The brightest galaxy, M94,

Table 4: M81 Filament and Background Galaxy Properties

Name	α (J2000)	δ (J2000)	D (Mpc)	V_{hel} (km s^{-1})	Type	f(Hα) (log ergs cm^{-2} s^{-1})
UGC 3580	06:55:30.8	69:33:47	15.90	1193	...	...
NGC 2366	07:28:55.7	69:12:59	3.19	102	IBm	-12.50 ± 0.02
KUG 0724+695	07:29:50.0	69:25:26	12.02	902	...	...
NGC 2403	07:36:52.7	65:35:52	3.30	134	Sc	-10.25 ± 0.04
KKH 44	08:16:38.5	69:20:49	14.08	1056	...	...
UGC 4305	08:19:06.5	70:43:01	3.39	160	Im	-11.28 ± 0.04
KDG 52	08:23:56.2	71:01:36	3.55	116	Irr	$<$ -15.30
DDO 53	08:34:08.6	66:11:03	3.56	23	Irr	-12.26 ± 0.12
UGC 4483	08:37:03.1	69:46:44	3.21	159	BCD	-12.50 ± 0.02
NGC 2787	09:19:18.5	69:12:12	9.31	716	...	...
Holmberg I	09:40:32.3	71:10:56	3.84	152	...	-12.44 ± 0.05
BK1N	09:45:15.3	69:23:22	7.86	584	Im	...
NGC 2976	09:47:15.6	67:54:49	3.56	6	SAc pec HII	-11.19 ± 0.06
NGC 2985	09:50:22.2	72:16:43	16.45	1213	...	...
NGC 3027	09:55:40.6	72:12:13	14.12	1061	...	...
M81	09:55:33.5	69:03:60	3.63	-32	SA(s)ab;LINER Sy1.8	-10.31 ± 0.02
M82	09:55:53.9	69:40:57	3.53	206	I0;Sbrst HII	-10.09 ± 0.03
NGC 3077	10:03:21.0	68:44:02	3.82	17	I0 pec HII	-11.18 ± 0.04
UGC 5423	10:05:30.6	70:21:52	5.30	350	...	-12.86 ± 0.05s
HIJASS J1021+68	10:20:30.1	68:39:25	3.70	64	...	...
UGC 5612	10:24:06.5	70:52:56	13.67	1025	...	...
IC 2574	10:29:19.0	68:27:42	4.02	79	SAB(s)m	-11.23 ± 0.07
UGC 5692	10:30:35.0	70:37:07	4.00	69	...	-12.82 ± 0.05
NGC 3403	10:53:54.8	73:41:25	15.35	1216	...	...

is apparently isolated but is morphologically disturbed and has a ring (Mulder & van Driel, 1993). Many of the galaxies show bursts of star formation (Karachentsev et al., 2003). Table 5 lists galaxy properties and Figure 18 shows galaxy locations.

Table 5: Canes I Group Galaxy Properties

Name	α (J2000)	δ (J2000)	D (Mpc)	V_{hel} (km s^{-1})	Type	f(Hα) (log ergs cm^{-2} s^{-1})
UGC 6541	11:33:30	49:14:00	3.80	250	Irr+Comp HII	-12.23 ± 0.02
NGC 3738	11:35:48	54:31:00	4.24	229	Irr HII	-11.81 ± 0.02
NGC 3741	11:36:06	45:17:00	3.25	229	ImIII/BCD	-12.41 ± 0.04
UGC 6817	11:50:48	38:52:00	3.22	242	Im	-12.49 ± 0.01
NGC 4068	12:04:00	52:35:00	4.53	210	IAm	-12.10 ± 0.04
NGC 4163	12:12:06	36:10:00	2.83	165	IAm BCD	-12.91 ± 0.08
NGC 4190	12:13:42	36:38:00	3.14	228	Im pec	-12.33 ± 0.02
UGCA 276	12:14:54	36:13:00	3.35	284	Im:	< -15.60
NGC 4214	12:15:36	36:19:00	3.31	291	IAB(s)m HII	-10.77 ± 0.01
NGC 4244	12:17:30	37:48:00	4.72	244	SA(s)cd: sp HII	-11.31 ± 0.07
UGC 7321	12:17:30	22:32:00	3.8	408	Sd	...
IC 779	12:19:36	29:53:00	3.05	222	E	...
IC 3308	12:25:18	26:42:00	4.22	316	Sdm:	...
NGC 4395	12:25:54	33:32:00	4.19	319	SA(s)m:;LINER Sy1.8	-11.28 ± 0.04
UGCA 281	12:26:12	48:29:00	5.44	281	Sm pec BCDG	-11.90 ± 0.01
UGC 7559	12:27:06	37:08:00	4.18	218	IBm	-12.45 ± 0.01
UGC 7577	12:27:36	43:29:00	3.22	195	Im	-12.50 ± 0.05
NGC 4449	12:28:12	44:05:00	3.38	207	IBm;HII Sbrst	-10.54 ± 0.02
UGC 7605	12:28:42	35:42:00	4.18	310	Im	-12.95 ± 0.05
UGC 7698	12:32:54	31:32:00	4.95	331	Im	-12.23 ± 0.03
UGCA 290	12:37:24	38:45:00	4.26	458	Im pec	-13.18 ± 0.04
UGCA 292	12:38:24	32:46:00	3.35	308	ImIV-V	-12.76 ± 0.01
IC 3687	12:42:12	38:30:00	4.02	354	IAB(s)m	-12.21 ± 0.03
M94	12:50:54	41:07:00	5.13	308	(R)SA(r)ab;Sy2 LINER	-10.74 ± 0.06
NGC 4789A	12:54:06	27:09:00	4.15	374	IB(s)m IV-V	-12.73 ± 0.05

Continued on Next Page…

Table 5 – Continued

Name	α (J2000)	δ (J2000)	D (Mpc)	V_{hel} (km s^{-1})	Type	f(Hα) (log ergs cm^{-2} s^{-1})
IC 4182	13:05:48	37:36:00	4.59	321	SA(s)m	...
UGC 8215	13:08:00	46:49:00	4.75	218	Im	-14.39 ± 0.16
NGC 5023	13:12:12	44:02:00	8.86	407	Scd	-12.13 ± 0.07
UGC 8308	13:13:24	46:19:00	3.70	163	Im	-13.11 ± 0.04
UGC 8320	13:14:30	45:55:00	4.31	192	IBm	-12.38 ± 0.06
UGCA 342	13:15:06	42:00:00	6.22	388	Im	-11.87 ± 0.05
NGC 5204	13:29:36	58:26:00	5.28	201	SA(s)m HII	-11.46 ± 0.03
UGC 8508	13:30:48	54:55:00	2.63	62	IAm	-12.59 ± 0.06
NGC 5229	13:34:06	47:55:00	6.4	364	SB(s)d? sp	-12.54 ± 0.03
NGC 5238	13:34:42	51:37:00	5.04	235	SAB(s)dm	-12.26 ± 0.06
UGC 8638	13:39:18	24:47:00	4.11	274	Im	-12.60 ± 0.03
UGC 8651	13:39:54	40:44:00	3.27	202	Im	-12.61 ± 0.05
UGC 8760	13:50:54	38:01:00	4.2	192	SAB(s)dm IV	-13.16 ± 0.11
UGC 8833	13:54:48	35:50:00	3.33	227	Im:	-13.36 ± 0.05
UGC 9128	14:15:54	23:03:00	4.22	153	ImIV-V	-13.70 ± 0.16
UGC 9240	14:24:42	44:31:00	3.13	150	IAm	-12.70 ± 0.07

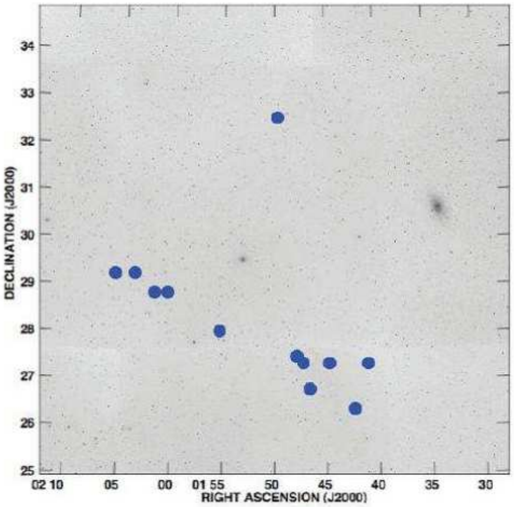

Figure 19: Locations of NGC 672 Group galaxies in blue dots, overlaid on optical DSS image.

3.3.5 NGC 672 Group

The NGC 672 and NGC 784 groups form a 6° linear filament of galaxies at a distance of approximately 5 Mpc (Zitrin & Brosch, 2008). The galaxies in both groups show evidence that a burst of star formation occurred ~ 10 Myr ago. Zitrin & Brosch (2008) conclude that these coincident SF bursts are most likely not due to galaxy interactions, since the SFR of the galaxies does not correlate with with projected distance from the brightest and most massive galaxy. Instead, they attribute the bursts in star formation to accretion along the filament. However, it is well known that NGC 672 and IC 1727 are undergoing a strong interaction (Combes et al., 1980; Sohn & Davidge, 1996). Table 6 lists galaxy properties and Figure 19 shows galaxy locations.

Table 6: NGC 672 Group Galaxy Properties

Name	α (J2000)	δ (J2000)	D (Mpc)	V_{hel} (km s^{-1})	Type	f(Hα) (log ergs cm^{-2} s^{-1})
NGC 672	01:47:54.5	27:25:58	7.35	422	SB(s)cd	-11.49 ± 0.06
IC 1727	01:47:29.9	27:20:00	6.80	345	SB(s)m	-11.96 ± 0.06
AGC110482	01:42:17.3	26:22:00	6.54	357	Irr	...
AGC111945	01:44:42.7	27:17:18	7.45	423	Irr	...
AGC111946	01:46:42.2	26:48:05	6.64	366	Irr	...
AGC112521	01:41:08.0	27:19:20	5.44	282	...	...
LEDA169957	01:36:35.9	23:48:54	9.33	563	...	...
NGC 784	02:01:16.9	28:50:14	4.52	198	SBdm: sp	-11.78 ± 0.04
AGC111977	01:55:20.4	27:57:13	4.43	207	Irr	...
AGC111164	02:00:10.2	28:49:53	...	168	Irr	...
UGC 1281	01:49:32.0	32:35:23	5.03	156	Sdm	-12.45 ± 0.07
AGC122834	02:03:47.0	29:11:53	...	...	...	...
AGC122835	02:05:33.0	29:13:58	...	...	...	...
UGC 1561	02:04:05.1	24:12:30	9.3	610	Im	-12.90 ± 0.04
NGC 855	02:14:03.6	27:52:36	9.73	575	E	-12.23 ± 0.04

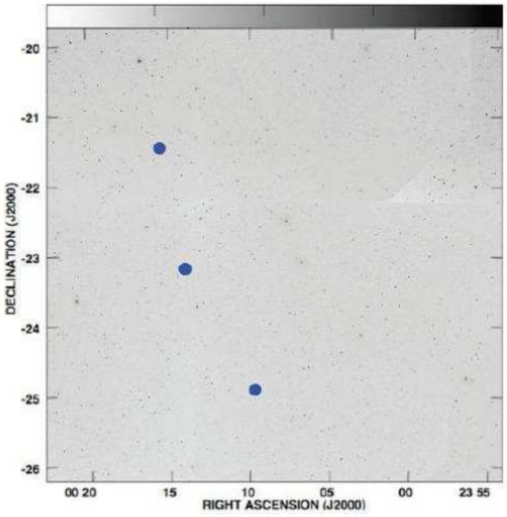

Figure 20: Locations of NGC 45 Group galaxies in blue dots, overlaid on optical DSS image.

3.3.6 NGC 45 Group

The NGC 45 group contains 3 large, low surface brightness galaxies (NGC 45, NGC 24, NGC 59) and is located at a distance of approximately 6 Mpc (Fouque et al., 1992). NGC 45 has a kinematical twist in the major axis and NGC 24 is kinematically regular (Chemin et al., 2006). However, NGC 24 has star forming regions scattered across the entire disk (Rossa & Dettmar, 2003). NGC 59 is the third galaxy in the group, and it appears to be normal and undisturbed. Table 7 lists galaxy properties and Figure 20 shows galaxy locations.

3.4 Application of Relative Interaction Indices

We applied the relative interaction indices described in Section 2.6 to the five galaxy groups, as well as to the M81 Filament. The results are tabulated in Tables

Table 7: NGC 45 Group Galaxy Properties

Name	α (J2000)	δ (J2000)	D (Mpc)	V_{hel} (km s^{-1})	Type	f(Hα) (log ergs cm^{-2} s^{-1})
NGC 24	00:09:56.5	-24:57:47	7.88	554	SA(s)c	-11.87 ± 0.04
NGC 45	00:14:04.0	-23:10:55	6.74	467	SA(s)dm	-11.22 ± 0.04
NGC 59	00:15:25.1	-21:26:40	5.37	362	SA(rs)0-:	-12.36 ± 0.06

8 through 11. For galaxies with no distance or velocity measurement, the distance and velocity of the most massive galaxy in the group was assumed. For galaxies with no Hα luminosity measurement in the 11HUGS survey (Kennicutt et al., 2008), the survey detection limit was assumed.

To avoid giving any one factor an artificially high or low weight, we assign a rank from 1-6 for each variable, and add the ranks for the final ranking order for our sample. The indices show that the Canes I group has the highest interaction potential, while the M81 Filament has the highest interaction evidence. The NGC 45 group ranks lowest in both indices. For the purpose of testing the role of galaxy interactions in the prevalence of H I clouds, the interaction evidence index is the most useful. Based upon these indices, we expect that the M81 Filament and M81 group should contain the most H I clouds, followed by NGC 672, Canes I, NGC 2403, and NGC 45.

To place these calculations in context, we have also calculated the interaction indices for the Local Group. The Local Group measurements are included in boldface in Tables 8 through 11. We consider the Local Group to consist of the Milky Way, M33, and M31 since many Local Group dwarf galaxies would not be visible from the distances of the groups we observed. We calculate the M31 and M33 star formation rate from the 11HUGS survey Hα luminosity, and assume the widely-accepted star formation rate of 1 $M_\odot$ yr^{-1} for the Milky Way. The Local Group has an interaction potential index lower than any group in our sample. The Local Group ranks second to the M81 Filament and M81 in interaction evidence.

Table 8: Interaction Potential Index: Values

Galaxy Group	N	N/max(N)	σ_v (km s^{-1})	σ_v/max(σ_v)
Local Group	**3**	**0.16**	**155.5**	**1**
NGC 2403	8	0.42	43.8	0.28
Canes I	19	1	77.4	0.50
M81 Filament	14	0.74	69.5	0.45
M81	14	0.74	79.8	0.51
NGC 672	8	0.42	86.5	0.56
NGC 45	1	0.05	96.1	0.62

Table 9: Interaction Potential Index: Ranked

Galaxy Group	N	σ_v	IP	IP ranked
Canes I	7	5	12	6
M81 Filament	5	6	11	5
NGC 2403	3	7	10	4
M81	5	4	9	3
NGC 672	3	3	6	2
NGC 45	1	2	3	1
Local Group	**2**	**1**	**3**	**7**

Table 10: Interaction Evidence Index: Values

Galaxy Group	N_{Tidal}	$N_{Tidal}/\max(N_{Tidal})$	N_{AGN}	$N_{AGN}/\max(N_{AGN})$	Mean SFR ($M_\odot$ yr^{-1})	Mean SFR/max(Mean SFR)
Local Group	**2**	**0.5**	**0**	**0**	**0.47**	**1**
M81 Filament	4	1	1	0.5	0.147	0.31
M81	4	1	1	0.5	0.103	0.22
NGC 672	2	0.5	2	1	0.023	0.05
Canes I	0	0	2	1	0.027	0.06
NGC 2403	0	0	0	0	0.071	0.15
NGC 45	0	0	0	0	0.067	0.14

Table 11: Interaction Evidence Index: Ranked

Galaxy Group	N_{Tidal}	N_{AGN}	Mean SFR	IE	IE Ranked
M81 Filament	6	4	6	16	6
M81	6	5	5	16	6
Local Group	**4**	**1**	**7**	**12**	**5**
NGC 672	4	6	1	11	4
Canes I	1	7	2	10	3
NGC 2403	1	1	4	6	2
NGC 45	1	1	3	5	1

CHAPTER IV

OBSERVATIONS AND DATA REDUCTION

4.1 Single-Dish Radio Astronomy

This section briefly outlines the design of single-dish radio telescopes.

A radio telescope works in essentially the same way as an optical telescope. An incoming wave is bounced off the telescope surface and onto a secondary reflector. The secondary reflector directs the light into a receiver. There are variations on this scheme and details in the placement of the reflectors and receivers depending on the telescope.

Radio waves are very low-power, so the instruments must be quite sensitive and precise. At the receiver, the signal is collected with an antenna and amplified. In order to distinguish the astronomical signal from the noise in the electronics, either position or frequency switching is used. In position switching, the beam is moved between the source being observed and empty sky. In frequency switching, the spectrum analyzer is switched to a bandpass away from the observing frequency.

Single radio dishes have poor angular resolution due to the long wavelengths of radio waves. For any telescope, the resolution depends on mostly the wavelength observed and the diameter of the telescope. Imperfections in observing conditions or the telescope optics can also diminish the telescope's resolution. Assuming a perfectly made telescope, and no atmospheric effects, the resolution is limited only by diffraction at the telescope's aperture. This theoretical lower limit on angular resolution is determined by the Rayleigh criterion:

$$\Delta\theta = 1.22\frac{\lambda}{D} \tag{6}$$

For radio telescopes, resolution is usually close to the theoretical limit due to the long wavelengths. However, the theoretical limit at radio wavelengths is very large! For instance, the best theoretically possible resolution of the largest fully-steerable radio telescope, the 100 meter Robert C. Byrd Green Bank Telescope of the National Radio Astronomy Observatory[1] in Green Bank, West Virginia (see Figure 21), is 8.8 arcminutes at 21 cm; in practice the resolution is 9.1 arcminutes due to imperfections in the reflecting surface and the presence of the secondary reflector. An optical telescope of the same diameter observing at 6000 $\AA$ would achieve milli-arcsecond resolution, a factor of about 10^5 better.

Although high angular resolution is not achievable with one radio dish, single-dish observations are an excellent probe of large-scale structure. They also have much better spectral resolution than interferometers. Additionally, single dishes have an advantage in that they sample every baseline from the diameter of the telescope down, whereas an array of telescopes only samples select baselines.

---

[1] The National Radio Astronomy Observatory (NRAO) is a facility of the National Science Foundation operated under cooperative agreement by Associated Universities, Inc.

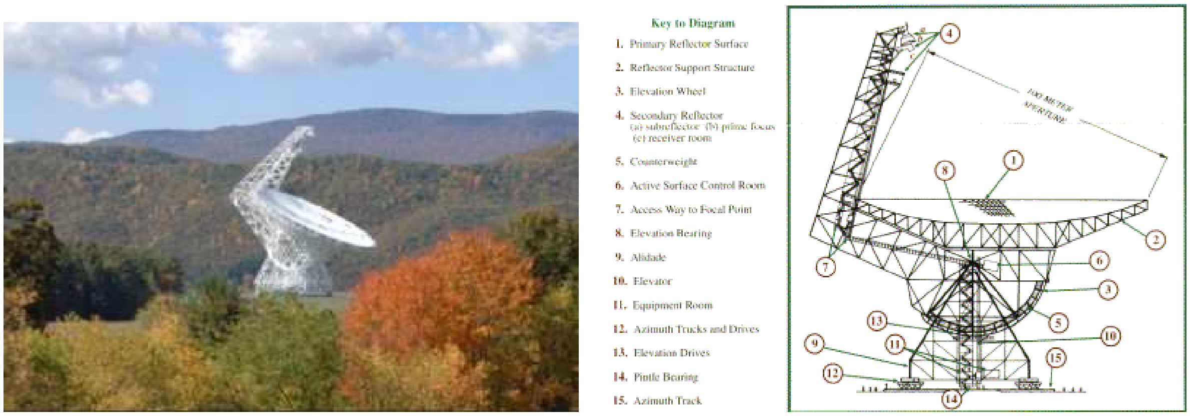

Figure 21: **Left**: the Robert C. Byrd Green Bank Telescope in Green Bank, WV. **Right**: A schematic diagram of the GBT (McKinnon, 2002)

4.2 Observations

This section describes the observations of all five galaxy groups and the M81 Filament. Since there were slight variations in observing technique for each galaxy group, this section is divided into 6 subsections–one for each galaxy group and one for the M81 Filament. All observations were carried out using the GBT in the L-band, which encompasses the HI 21-cm line. The instrumental parameters of the GBT at L-band are summarized in Table 12. For the M81, NGC 2403, and Canes I Groups and the M81 Filament the projected beam size of the GBT is approximately 10 kpc; this is well matched to the expected angular size of H I clouds above our mass detection threshold (Thilker et al., 2004). For the NGC 672 and NGC 45 Groups, the beam reaches a projected size of 20 kpc; this is as much as a factor of 2 larger than the expected angular size of H I clouds above our mass detection threshold. Therefore, it is possible that smaller clouds in those groups will not be detected due to beam dilution.

Table 12: Parameters of the Robert C. Byrd Green Bank Telescope at L-Band

Telescope:	
Diameter	100 m
Beamwidth (FWHM)	$9.1'$
Linear resolution	2.7 D_{Mpc} kpc
Aperture efficiency	~ 0.7
Receiver:	
System Temperature	~ 20 K

4.2.1 M81 Group

We observed the M81/M82 group on 12-16 June, 2003. The brightest galaxies (M81, M82, NGC3077, and NGC 2976) are all within a $2° \times 2°$ region centered on M81, where we concentrated our observations. This $2° \times 2°$ region was observed by moving the telescope in declination and sampling every $4'$ at an integration time of 5 seconds per sample. Strips of constant declination were spaced by $2.'7$. A larger field was then sampled at $4'$ spacing and an integration time of one second per spectrum. The data discussed here cover an area $3° \times 3°$ centered on M81 to include NGC 2976 and the extended H I emission associated the group.

Over the inner 4 square degree region, the resultant typical RMS noise is 18 mK; outside the central region the noise in a channel rises to ≈ 51 mK. Table 13 gives a summary of observations.

Table 13: M81 Observations Summary

Area:	
α range (J2000)	$09^h40^m00.0^s$ - $10^h10m00.0s$
δ range (J2000)	67°30‘00.0“ - 70°30‘00.0“
Observations:	
Center Frequency (MHz)	1410
Bandwidth (MHz)	50
Velocity Range (Heliocentric, km s^{-1}))	-3172 - 7376
Channel Width (kHz)	24.4
Velocity Resolution (km s^{-1})	5.2
Integration time (hours):	
Inner Region	3.88
Expanded Area	6.75
Typical RMS noise (mK/channel):	
Inner Region	18
Expanded Area	51
Sensitivity to H I (1σ):	
M_H ($\times 10^5$ $M_\odot$)	
Inner Region	1.4
Expanded Area	3.9
Beam size (kpc):	
Both Regions	9.8

4.2.2 NGC 2403 Group

We observed the NGC 2403 group in 9 sessions between 8 June and 1 August, 2008. We combined the 9 observing sessions into three maps: a 6° × 2° region containing NGC 2403, NGC 2366, and DDO 44; a 4°×4° region containing UGC 4305, UGC 4483, and K52, with an extension to observe the region around VKN; and a 1° × 1° region around DDO 53. Additionally, in light of the detection of a cloud at $07^h36^m12.1^s$, 67°33“25‘, we re-observed the 1° × 1° region centered on the object for an additional 22 minutes.

The regions were observed by moving the telescope in declination and sampling every 3‘ at an integration time of 3 seconds per sample. Strips of constant declination were spaced by 3‘. Corresponding maps were made by moving the telescope in right ascension to form a 'basket weave' pattern over the region. In the end, each 3‘ pixel was integrated for approximately 6 seconds except in the region surrounding the large new cloud, where each pixel received 18 seconds.

4.2.3 M81 Filament

We observed the M81 Filament in 40 sessions between June 2003 and August 2009. This includes data taken for observations of the M81/M82 and NGC 2403 galaxy groups. We combined the 40 observing sessions into a single 8.7° × 21.3 ° map centered at $08^h40^m37.0^s$, 69°17‘16“. Figure 33 shows a layout of the observations. Observations are described in Table 15.

The filament was observed by moving the telescope in declination and sampling

Table 14: NGC 2403 Observations Summary

Area:	
NGC 2403 α range (J2000)	$07^h25^m00.0^s$ - $07^h40^m00.0^s$
NGC 2403 δ range (J2000)	64°00‘00.0“ - 70°00‘00.0“
UGC 4305 α range (J2000)	$08^h05^m00.0^s$ - $08^h45^m00.0^s$
UGC 4305 δ range (J2000)	68°30‘00.0“ - 72°30‘00.0“
DDO 53 α range (J2000)	$08^h29^m00.0^s$ - $08^h39^m00.0^s$
DDO 53 δ range (J2000)	65°40‘00.0“ - 66°40‘00.0“
Observations:	
Center Frequency (MHz)	1418.4065
Bandwidth (MHz)	12.5
Velocity Range (Heliocentric, km s^{-1}))	-890 - 1750
Channel Width (kHz)	24.4
Velocity Resolution (km s^{-1})	5.2
Integration time (hours):	
Total	21.0
Typical RMS noise (mK/channel):	
All Regions	4.7
Sensitivity to H I (1σ):	
M_H ($\times$ 10^6 $M_\odot$)	
All Regions	1.57
Beam Size (kpc):	
All Regions	8.9

every $3'$ at an integration time of 1-3 seconds per sample, depending on the observation session. Strips of constant declination were spaced by $3'$. Corresponding maps were made by moving the telescope in right ascension to form a 'basket weave' pattern over the region. Total integration time for the entire map was approximately 187 hours. In Figure 34 it is possible to infer the rms noise and corresponding mass sensitivity of the map as a function of position.

The GBT spectrometer was used with a bandwidth of either 12.5 or 50 MHz, depending on the observation session. The combined bandwidth for the final map is 10.5 MHz, corresponding to a velocity range from -890 to 1320 km s^{-1} with a velocity resolution of 5.2 km s^{-1}. Our observations cover a large angular area in order to make a complete study of the H I properties across the entire extent of the filament.

4.2.4 Canes I Group

We observed the Canes I Group in 12 sessions between January and August 2009. We combined the observing sessions into 3 maps encompassing the group galaxies.

Maps were made by moving the telescope in declination and sampling every $3'$ at an integration time of 2-3 seconds per sample. Strips of constant declination were spaced by $3'$. Corresponding maps were made by moving the telescope in right ascension to form a 'basket weave' pattern over the region. Total integration time was approximately 58 hours. Table 17 gives the rms noise and corresponding mass sensitivity of each map.

Table 15: M81 Filament Observations Summary

Area:	
α range (J2000)	$07^h00^m00.0^s$ - $11^h00^m00.0^s$
δ range (J2000)	64°00‘00.0“ - 74°00‘00.0“
Observations:	
Center Frequency (MHz)	1419.4
Bandwidth (MHz)	10.5
Velocity Range (Heliocentric, km s^{-1}))	-890 - 1320
Channel Width (kHz)	24.4
Velocity Resolution (km s^{-1})	5.2
Integration time (hours):	
Total	187
Typical RMS noise (mK/channel):	
All Regions	8.6
Sensitivity to H I (1σ):	
M_{HI} ($\times 10^5$ $M_\odot$)	
Total	6.4
Beam Size (kpc):	
All Regions	9.0

4.2.5 NGC 672 Group

We observed the NGC 672 Group in 11 sessions between January and August 2009. We combined the observing sessions into 3 maps encompassing the group galaxies.

Maps were made by moving the telescope in declination and sampling every 3‘ at an integration time of 2-3 seconds per sample. Strips of constant declination were spaced by 3‘. Corresponding maps were made by moving the telescope in right ascension to form a ‘basket weave’ pattern over the region. Total integration time was approximately 47 hours. Table 17 gives the rms noise and corresponding mass sensitivity of each map.

Table 16: Canes I Observations Summary

Area:	
NGC 4244 α range (J2000)	$12^h05^m00.0^s$ - $12^h25^m00.0^s$
NGC 4244 δ range (J2000)	35°00‘00.0“ - 39°00‘00.0“
M94 α range (J2000)	$12^h46^m00.0^s$ - $12^h56^m00.0^s$
M94 δ range (J2000)	40°00‘00.0“ - 42°00‘00.0“
NGC 4395 α range (J2000)	$12^h21^m00.0^s$ - $12^h31^m00.0^s$
NGC 4395 δ range (J2000)	32°30‘00.0“ - 34°30‘00.0“
Observations:	
Center Frequency (MHz)	1420.4
Bandwidth (MHz)	12.5
Velocity Range (Heliocentric, km s^{-1}))	-1315 - 1320
Channel Width (kHz)	24.4
Velocity Resolution (km s^{-1})	5.2
Integration time (hours):	
NGC 4244	42.2
M94	9.8
NGC 4395	5.7
Typical RMS noise (mK/channel):	
NGC 4244	26.3
M94	21.2
NGC 4395	32.6
Sensitivity to H I (1σ):	
M_{HI} ($\times$ 10^5 $M_\odot$)	
NGC 4244	3.40
M94	5.88
NGC 4395	6.04
Beam Size (kpc):	
NGC 4244	12.7
M94	13.9
NGC 4395	11.3

Table 17: NGC 672 Observations Summary

Area:	
NGC 672 α range (J2000)	$01^h38^m00.0^s$ - $01^h52^m00.0^s$
NGC 672 δ range (J2000)	28°00‘00.0“ - 26°00‘00.0“
NGC 784 α range (J2000)	$01^h58^m00.0^s$ - $02^h04^m00.0^s$
NGC 784 δ range (J2000)	29°30‘00.0“ - 28°10‘00.0“
UGC 1281 α range (J2000)	$01^h47^m00.0^s$ - $01^h15^m00.0^s$
UGC 1281 δ range (J2000)	33°10‘00.0“ - 32°00‘00.0“
Observations:	
Center Frequency (MHz)	1418.4
Bandwidth (MHz)	12.5
Velocity Range (Heliocentric, km s^{-1}))	-890 - 1740
Channel Width (kHz)	24.4
Velocity Resolution (km s^{-1})	5.2
Integration time (hours):	
NGC 672	36.4
NGC 784	5.3
UGC 1281	5.7
Typical RMS noise (mK/channel):	
NGC 672	5.92
NGC 784	12.3
UGC 1281	12.8
Sensitivity to H I (1σ):	
M_{HI} ($\times 10^5$ $M_\odot$)	
NGC 672	2.81
NGC 784	2.66
NGC 1281	3.41
Beam size (kpc):	
NGC 672	19.8
NGC 784	12.2
UGC 1281	13.6

4.2.6 NGC 45 Group

We observed the NGC 45 Group in 9 sessions between January and August 2009. We combined the observing sessions into one map for each of the three group galaxies (NGC 45, NGC 24, NGC 59).

Maps were made by moving the telescope in declination and sampling every 3‘ at an integration time of 2-3 seconds per sample. Strips of constant declination were spaced by 3‘. Corresponding maps were made by moving the telescope in right ascension to form a ‘basket weave’ pattern over the region. Total integration time was approximately 11-17 hours per galaxy. Table 18 gives the rms noise and corresponding mass sensitivity of each map.

4.3 Data Reduction

This section describes the data reduction process. This section includes four subsections to include the slight variations in baseline subtraction technique for different observations.

The archived GBT data were reduced in the standard manner using the GBTIDL[2], NRAO AIPS[3], and aips++ data reduction packages. The data reduction process includes the following steps:

1. **Smoothing**: Smoothing spectra to a coarser velocity resolution increases the signal to noise ratio; the optimum channel spacing is the maximum width that

---

[2] Developed by the National Radio Astronomy Observatory; documentation at http://gbtidl.sourceforge.net

[3] Developed by the National Radio Astronomy Observatory; documentation at http://www.aoc.nrao.edu/aips

Table 18: NGC 45 Observations Summary

Area:	
NGC 45 α range (J2000)	$00^h11^m00.0^s$ - $00^h17^m00.0^s$
NGC 45 δ range (J2000)	-22°30‘00.0“ - -23°50‘00.0“
NGC 24 α range (J2000)	$00^h07^m00.0^s$ - $00^h13^m00.0^s$
NGC 24 δ range (J2000)	-24°20‘00.0“ - -25°40‘00.0“
NGC 59 α range (J2000)	$00^h13^m00.0^s$ - $00^h18^m00.0^s$
NGC 59 δ range (J2000)	-20°50‘00.0“ - -22°10‘00.0“
Observations:	
Center Frequency (MHz)	1420.4
Bandwidth (MHz)	12.5
Velocity Range (Heliocentric, km s^{-1}))	-1315 - 1320
Channel Width (kHz)	24.4
Velocity Resolution (km s^{-1})	5.2
Integration time (hours):	
NGC 45	11.3
NGC 24	12.9
NGC 59	16.5
Typical RMS noise (mK/channel):	
NGC 45	13.9
NGC 24	10.2
NGC 59	10.9
Sensitivity to H I (1σ):	
M_{HI} ($\times 10^5$ $M_\odot$)	
NGC 45	6.67
NGC 24	6.68
NGC 59	3.10
Beam size (kpc):	
NGC 45	21.3
NGC 24	18.2
NGC 59	14.5

still allows detection of H I clouds. Spectra were smoothed to a channel spacing of 24.4 kHz, corresponding to a velocity resolution of 5.2 km s^{-1}. This velocity resolution corresponds to the linewidths of H I clouds, which are expected to range from 20-80 km s^{-1}.

2. **Construction of reference spectrum**: For each observation session, a reference spectrum is required to remove noise and emission that is not of interest (i.e., receiver noise and other hardware, cosmic microwave background, etc.). A reference spectrum for each of the observation sessions was made using an observation of a region free from H I emission associated with the galaxy group, usually from the edges of the maps. This type of reference preserves the extragalactic emission that we are primarily interested in studying. However, this method has the disadvantage of including foreground Milky Way emission in the reference, so the Milky Way emission in the final calibrated maps is not accurately preserved.

3. **Amplitude calibration**: The reference spectrum was then used to perform a (signal-reference)/reference calibration of each integration of each scan. The calibrated spectra were scaled by the system temperature, corrected for atmospheric opacity and GBT efficiency. We assumed a zenith atmospheric opacity $\tau_0 = 0.009$. We adopted the GBT efficiency equation from Langston & Turner (2007):

$$\eta_A(\nu) = 0.71 \exp\left(-\left(\frac{\nu}{61.3\mathrm{GHz}}\right)^2\right), \tag{7}$$

where $\eta_A(\nu)$ is the GBT efficiency as a function of frequency, and ν is the frequency in GHz.

4. **Radio frequency interference removal**: Calibrated GBTIDL 'keep' files were processed using `idlToSdfits` [4]. This program is used to identify data contaminated by radio frequency interference (RFI) and convert the data to the form required for input into the NRAO AIPS package. In order to remove RFI from the data, `idlToSdfits` was run on each set of scans, and the resulting RMS noise values were examined. Spectra that showed high values of RMS noise across many channels were flagged and removed. The observations were relatively free of RFI and less than 0.5 % of all spectra were adversely affected by RFI. The spectra exhibiting unacceptably high RFI values were identified by tabulation of the RMS noise level in channels free of neutral hydrogen emission.

5. **Gridding**: After calibration, the observations were imported into the AIPS package. Observations were gridded and convolved using the AIPS task SDIMG, which also averages polarizations. For the convolution function, a round Bessel function times Gaussian function was used, with parameters optimized for GBT H I observations (F. J. Lockman, private communication).

---

[4] Developed by Glen Langston of NRAO; documentation at http://wiki.gb.nrao.edu/bin/view/Data/IdlToSdfits

6. **Baseline fitting and subtraction**: A baseline subtraction is necessary to remove any DC offset and/or curvature in the baseline shape. The baseline subtraction process also removes gain and sky variations between the time of observation of the source and the reference scan. Our baseline fitting technique varied for different galaxy groups, as we refined and simplified our baselining technique as observations progressed. The baseline fitting processes are described in the following sections.

7. **Determination of beam parameters**: The beam size determines effective angular resolution. We determined beam parameters by fitting a two dimensional Gaussian to the continuum emission from the quasar 3C286, which is unresolved in the GBT L-band beam. The GBT beam at L-band is essentially circular, with a diameter of is 9.15‘ ± 0.05‘.

8. **Flux calibration**: To convert to units of flux density, we measured the calibration source 3C286, whose flux density is as a function of frequency is given by Ott et al. (1994). The calibration from K to Jy was derived by mapping 3C286 in the same way that the H I maps were produced. After all corrections for the GBT efficiency and the mapping process, the scale factor from K/Beam to Jy/Beam in our images is 0.43 ± 0.03.

4.3.1 M81 Group Baseline Subtraction

The spectral bandpass variation, or baseline, was removed by subtraction of a median filtered baseline with 1300 km s^{-1} width (6.0 MHz width). The median filter baseline subtraction process is summarized here and is described with example figures in Langston & Turner (2007). The baseline was subtracted for each polarization separately, in order to remove the Intermediate Frequency (IF) electronics gain variations that are unique to each signal path. The baseline value is computed for each individual channel of the spectrum by computing the median value of all channels within a range of channels centered on the individual channel. The median width must be small enough to preserve the gain variations, yet large enough to reject spectral lines within the median range. After computation, the baseline is subtracted from the original spectrum.

The median filtering technique can be problematic. Since the linewidth of large galaxies is much wider than that of H I clouds, it is difficult to select a median width that will preserve the spectra of both types of objects correctly. A polynomial baseline fitting does not require selection of a correct width – the following sections describe this technique, used for subsequent observations.

4.3.2 NGC 2403 Group Baseline Subtraction

A 3rd-order polynomial was fit to line-free regions of the spectra within aips++. This baseline was subtracted from the gridded spectra. We suspect that a 3rd-order baseline fit might be overkill, and introduces the possibility of fitting out real sources.

Therefore, a simple 1st-order baseline fit was used for subsequent observations.

4.3.3 M81 Filament, Canes I, NGC 672, and NGC 45 Groups Baseline Subtraction

A 1st-order polynomial was fit to line-free regions of the spectra and subtracted from the gridded spectra using the AIPS task IMLIN. Only channels in high negative velocity ranges, where few or no sources are expected, were used for the fit. This simple baseline fit was extrapolated to the positive velocity range, where galaxies in the Hubble flow are expected. This baseline velocity range for the fit yielded good results for areas free of strong continuum radio sources, the majority of the region.

CHAPTER V

RESULTS

5.1 Data Analysis

H I mass detection thresholds for each observed region were calculated assuming that clouds would be unresolved in the GBT beam, using the formula:

$$\left(\frac{\sigma_M}{M_\odot}\right) = 2.36 \times 10^5 \left(\frac{D}{\mathrm{Mpc}}\right)^2 \left(\frac{\sigma_s}{\mathrm{Jy}}\right) \left(\frac{\Delta V}{\mathrm{kms}^{-1}}\right) \sqrt{N}, \tag{8}$$

where D is the distance to the group, σ_s is the rms noise in one channel in Janskys, ΔV is the channel width, and N is the number of channels required for a secure detection. For our calculation, we used an H I cloud linewidth of 20 km s^{-1}, corresponding to $N = 4$. Mass detection thresholds are listed in Chapter 4 and Table 19. H I masses were calculated using

$$\left(\frac{M}{M_\odot}\right) = 2.36 \times 10^5 \left(\frac{D}{\mathrm{Mpc}}\right)^2 \left(\frac{F}{\mathrm{Jy}}\right) \left(\frac{\Delta V}{\mathrm{km\ s}^{-1}}\right), \tag{9}$$

where F is the integrated flux of the galaxy. Masses and spectra of known galaxies are tabulated in Chapter 6.

Column density measurements are also relevant for the purpose of studying the H I cosmic web associated with the M81 Filament. Column density sensitivity was calculating using:

$$\left(\frac{\sigma_{N_{HI}}}{N_{HI}}\right) = 1.82 \times 10^{18} \left(\frac{\sigma_{T_B}}{\mathrm{K}}\right) \left(\frac{\Delta V}{\mathrm{km\ s^{-1}}}\right) \sqrt{N}, \tag{10}$$

where σ_{T_B} is the average rms noise in one channel in Kelvin. The same linewidth (corresponding to $N = 4$) was used for this calculation as for the mass sensitivity calculation above. The average 5σ detection threshold for H I column density was 4.4×10^{18} cm^{-2}. This figure falls within the "H I Desert", where the gas in the cosmic web is not affected by self-shielding and is therefore photoionized (Popping et al., 2009). Hence, we do not expect to detect diffuse H I in the filament between the two galaxy groups. Our lowest 5σ detection threshold for H I column density was $\sim 1 \times 10^{18}$ $M_\odot$, which is approximately 3 times too high to detect the diffuse cosmic web in H I emission.

H I cloud candidates were found by visual inspection of each channel of the baseline subtracted spectral line cube. Objects that were spatially distinct from group galaxies and tidal streams and coherent in velocity over more than one channel were considered to be cloud candidates. For each candidate, a plot of spectral intensity versus velocity was also produced and checked. Galaxies are easily detected in this procedure, showing a broad emission line with width of up to a few 100 km s^{-1} . We required a cloud candidate to be visible in at least two channels, therefore the lowest velocity width that could be detected was 10 km s^{-1} . At the locations of strong continuum radio sources, the linear spectral baseline t was occasionally poor. In these cases, the spectra would show a broad slope, > 400 km s^{-1} wide, either increasing or decreasing with frequency. These candidates were discarded, as the result of a poor spectral baseline. Only a small fraction of the observations of the M81 Filament were affected by this problem, and none of the other maps were affected. The angular region of the M81 Filament that we mapped corresponds to more than 10,000 GBT beams. Only 26 locations showed spectra with poor spectral baselines.

Positions of candidates were measured at the point of peak emission. For each H I cloud candidate, spectra were obtained from ISPEC. For the M81 group, H I column density maps and position-velocity (PV) plots were made for the velocity range in which the candidate was detected in order to distinguish the clouds in velocity space from the tidal material associated with interactions.

The boundaries of regions containing clouds were determined by inspection of the spectral line images. The boundaries of the region averaged into the H I intensity profile were chosen to separate the individual components from the other galaxies. However all of the newly identified clouds are in close proximity to the interacting members of the galaxies. For each profile, the region was set using a box approximating the area of neutral hydrogen most clearly associated with the object in question and not involved in interaction.

5.2 Completeness of Study

5.2.1 Velocity

Our observations cover more than ± 700 km s^{-1} beyond the systemic velocity of any group galaxy. This allows us to detect clouds associated with any of the mechanisms that create H I clouds, which all predict clouds to be within 300 km s^{-1} of the galaxy's velocity (Miller et al., 2009). In their study of H I clouds in M31, Thilker et al. (2004) found clouds mostly within 150 km s^{-1} of the systemic velocity of M31. Filaments were found within 80 km s^{-1} of the galaxy's velocity. If these values can be interpreted as a prediction for H I cloud velocities, we expect to find clouds with velocities within 150 km s^{-1} of the main galaxies in each group.

There is some overlap in velocity space between the M81 Filament (including the M81 and NGC 2403 Groups) and the Milky Way, and over this velocity range we can not discriminate between local and distant emission. In this velocity range (-85 km s^{-1} to 25 km s^{-1}), we are unable to detect H I clouds. In addition, the Milky Way HVC Complex A is located in the direction of the M81 Filament and is at the velocities -120 to -200 km s^{-1} (Wakker & van Woerden, 1997), so confusion with small Complex A clumps is possible.

5.2.2 Position

Studies of the Milky Way and M31 find clouds anywhere within 1-50 kpc of a galaxy center (Thilker et al., 2004; Wakker & van Woerden, 1997). Simulations predict that clouds will be found as close as 3 kpc and as far as 750 kpc from galaxies (Miller et al., 2009). In order to balance the requirement of a high mass sensitivity and a large angular area in our observations, we attempted to observe a projected radius of at least 50 kpc around major group galaxies.

Our galaxy group maps generally cover this much area or more. For some galaxies in the Canes I and NGC 672 Groups, (M94, NGC 4395, NGC 784, and NGC 1281) slightly less area ($\sim$ 40 kpc from the galaxy) was covered.

In order to detect H I clouds in the M81 Filament indicative of either cold accretion or the cosmic web, a large-area map is required. Cold accretion clouds are expected to be contained in a $\sim$ 60 kpc radius around large galaxies (Kereš & Hernquist, 2009). Our map of the M81 Filament has a projected size of 480 kpc × 1.2 Mpc, and encompasses the M81 Group, NGC 2403 Group, and the region between the two groups. The map size is adequate to detect cold accretion clouds and the H I cosmic web, in addition to interaction remnants and DM halo-associated clouds.

The angular resolution of our observations ranges from 10-20 kpc. Since galactic fountain H I clouds are found at a distance of < 10 kpc from the galactic disk, we may not be able to resolve galactic fountain clouds, depending on their velocity and orientation. We can detect clouds associated with all other H I cloud originating mechanisms, provided that their sizes are large enough to avoid beam dilution (Miller et al., 2009).

5.2.3 Mass

The 5σ detection threshold for H I masses ranged from 13.7 to 18.0 $\times$ 10^6 $M_\odot$, assuming a linewidth of 20 km s^{-1} and using the distance of the most massive group galaxy. For the M81 Filament, the average H I mass detection threshold was calculated using the distance of M81 and the mean rms sensitivity.

With these mass detection thresholds, we would be able to detect analogues to the most massive H I clouds that have been detected surrounding nearby galaxies, as well as large Milky Way objects such as Complexes C and H and the Magellanic Stream. These clouds are the most likely to originate in galaxy interactions, cold accretion, and dark matter halos, rather than from supernovae (Miller et al., 2009).

We have compiled the published values for all known extraplanar H I clouds surrounding nearby galaxies and the Milky Way. If this mass spectrum is representative of the general extragalactic H I cloud mass function, we can use these masses to calculate the mass completeness of our observations. Given the mass limits for our observations, we can detect anywhere from 8% to 29% of the analogous clouds surrounding the galaxies we have observed. Table 19 lists the average mass detection threshold and mass completeness for each galaxy group. Figure 22 shows the mass spectrum of known H I clouds compared to our observational limits for each galaxy group. Note that the mass spectrum for H I clouds is not well-constrained, particularly for the Milky Way, since the properties of Milky Way H I clouds beyond the stellar halo are not known.

We would also be able to detect cold accretion clouds found in the simulations of Kereš & Hernquist (2009), which are predicted to have H I masses of 10^6 to 10^7 $M_\odot$.

5.3 New H I Cloud Identifications

In total, we identify 15 new H I clouds in the 5 galaxy groups and M81 Filament. Thirteen of these clouds are located in the direction of the M81 Filament, either near the M81 Group, NGC 2403 Group, or between the two. The remaining two clouds

Table 19: Mass Detection Thresholds

Galaxy Group	Average Detection Threshold (5σ, $\times 10^6$ $M_\odot$)	Fraction of Detectable H I Clouds
M81	1.37	0.29
NGC 2403	1.46	0.29
M81 Filament	3.23	0.24
Canes I	7.40	0.19
NGC 672	9.10	0.13
NGC 45	18.0	0.08

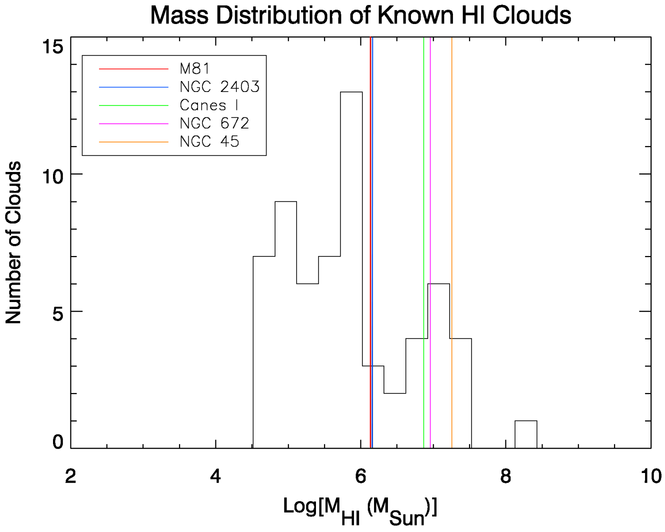

Figure 22: Mass distribution of known H I clouds associated with nearby galaxies. Our mass detection thresholds are indicated with vertical lines. Clouds to the right of the lines would be detectable in our observations. If this population of clouds is representative of galaxy groups, our detection limit allows us to detect the most massive 8-29% of H I clouds in the group. Data: Thilker et al. (2004), Grossi et al. (2008), Chynoweth et al. (2008), van der Hulst & Sancisi (1988), Wakker et al. (2007), Thom et al. (2006), Simon et al. (2006), van Woerden et al. (1999a), Putman et al. (2003), Lockman et al. (2008), Braun & Thilker (2004), Miller et al. (2009), Hess et al. (2009).

are in the direction of the Canes I Group. In the direction of the NGC 672 and NGC 45 groups, we do not detect any H I clouds.

We have designated all H I cloud detections with the identifier GBC for "Green Bank Cloud," and the coordinates of the cloud, i. e., GBC Jhhmmss.s+ddmmss. For the purpose of simplicity in this dissertation, H I clouds are also designated with a number, in order of detection. The following sections detail our results.

5.3.1 M81 Group

Moment maps showing H I the column density are presented in Figures 23 and 24. The integrated column density map from Yun et al. (1994) is shown as the gray scale image in Figure 23. The locations of each major galaxy, dwarf galaxy, and H I cloud detection are indicated. The dwarf galaxy BK 1N (Huchtmeier & Skillman, 1998) is also detected by our observations in the velocity range $\sim$ 560 to 580 km s^{-1}. BK 1N has a velocity outside the range shown in Figure 23, and is therefore not included in the figure.

We detect five H I clouds associated with the M81 Group. See Table 20 for a summary of detections. Three of the clouds are clearly associated with a particular galaxy, and two are located between two known galaxies. All H I cloud detections have some level of H I structure surrounding them, connecting them to the associated galaxy. All of the clouds have a velocity close to that of at least one of their parent galaxies. Clouds were only detected between -105 and 280 km s^{-1}, and the maximum difference between a cloud and associated galaxy was 119 km s^{-1}. Additionally, all of the clouds are within 35 kpc (in projection) of the group. The distance values are consistent with detected distances of clouds near M31 (Thilker et al., 2004).

Figure 24 shows H I column density maps of each detection. For these maps, only the velocity range in which the cloud of interest was detected is summed into the integrated intensity map. One channel on each end of the detected range was excluded from the integrated intensity map in order to increase the signal to noise ratio and highlight the cloud.

Figure 25 shows the spectra of each H I cloud. The mass of each cloud was measured by summing the flux densities measure for the angular regions over the velocity range show in figure 25. The masses of the detected clouds are of order 10^7 $M_\odot$. In order to measure the systemic velocity and velocity dispersion of each cloud, a Gaussian function was fit to the average intensity profile.

Figure 26 shows position-velocity (PV) diagrams for each new H I cloud. Whereas clouds may be difficult to distinguish from the extended H I emission associated with major galaxies and tidal streams in the column density maps, the H I spectra and position-velocity diagrams show the distinct nature of these new clouds.

We have compared the GBT observations with the VLA images from Yun et al. (1993). Below, we describe the H I distribution found in the VLA images at the locations of each cloud.

Cloud 1

Cloud 1 (GBC J095007.2+695556) is located to the north-west of M82, separated by approximately 31 kpc in projection. Cloud 1 lies outside the region imaged by Yun et al. (1993), and no VLA images are currently available for this area.

Cloud 2

Cloud 2 (GBC J100250.7+681949) sits immediately to the south-east of NGC 3077, at a distance of 23 kpc. It is a distinct clump of H I situated within a filamentary structure that extends from NGC3077 south and west, encompassing the dwarf galaxies BK5N, IKN, and K64. The cloud is in the upper range of the filament velocity. The morphology of the filament to the west of the cloud suggests that it may be plunging into NGC3077. Alternatively, the cloud may be gas blown out of the galaxy by star formation. Cloud 2 is a clump within a pronounced filament to the southwest of NGC 3077. This cloud/filament structure may be associated with the dwarf galaxies BK5N, IKN, and K64, as they are close in projection.

Cloud 2 is very weakly visible in the VLA images of Yun et al. (1993). Clearly the VLA images are missing diffuse emission associated with this cloud. Other regions have similar strength in the VLA images, but are significantly weaker in the GBT images. A weak secondary peak in the GBT image, at $10^{h}02^{m}12.3^{s}$, 68°20‘34“, is also visible in the VLA image.

Cloud 2 and the associated filament may be associated with the clouds in the same vicinity detected by Brinks et al. (2008) using the VLA.

Cloud 3

Cloud 3 (GBC J095244.9+681250) is located 27 kpc to the north-east of NGC 2976. It is distinct from NGC 2976. Cloud 3 overlaps with the velocity range of the Galaxy, making properties difficult to determine accurately. Cloud 3 is clearly resolved in the GBT image and only barely detected above the background noise in the VLA images of Yun et al. (1993).

Cloud 4

Cloud 4 (GBC J100145.0+691631) is located to the west of the H I bridge between M81 and M82. It is clearly bound to the H I bridge, but is a distinct clump. Cloud 4 also overlaps with the velocity range of the Galaxy.

Although Cloud 4 is located equidistant from M81 and M82 at a projected distance of 33 kpc from both galaxies, it is most likely associated with M81, as it is much closer to M81 in velocity.

In the H I images of Yun et al. (1993), Cloud 4 has the most compact structure of our newly detected clouds. The peak in the VLA emission in this region is very close to the center of the GBT detection.

Cloud 5

Cloud 5 (GBC J095506.3+692205) is to the south of M82, located approximately halfway between M81 and M82. Cloud 5 is only distinct from M82 in a small range of velocities. It is unclear whether the cloud is actually a separate feature from M82;

it appears as a red shoulder in the H I profile. Since the H I profile of the cloud is blended with M82, the calculated mass is difficult to determine. In order to calculated the mass of the cloud a Gaussian was fit to the H I spectrum in the peak range where the cloud was detected.

Cloud 5 is a large diffuse region in the maps of Yun et al. (1993), only a few sigma above the noise in the VLA images.

5.3.2 NGC 2403 Group

Moment maps of the H I column density are presented in Figures 28 and 29. All of the galaxies in the NGC 2403 group appear undisturbed at the angular resolution of the GBT. We do not detect the filaments of H I in NGC 2403 seen in higher-resolution VLA data (Fraternali et al., 2002), most likely due to beam dilution.

Three H I clouds are detected near NGC 2403 and NGC 2366, labeled numbers 6-8 in Figures 28 and 29. The clouds are described below, and Table 5 lists their properties. Spectra of the clouds are shown in Figure 30.

In contrast to the clouds discovered in the M81 Group, clouds 6-8 are not kinematically connected to NGC 2403 Group galaxies or (nonexistent for this group) tidal material. It is not immediately clear whether the clouds are extragalactic or local to the Milky Way. The region mapped is just south of the Milky Way HVC Complex A, so the clouds may be associated with Complex A or other Milky Way HVCs. In order to distinguish between the two possibilities, we analyzed the spectra of the clouds.

Cloud velocity widths are 20-30 km s^{-1} and consistent with both a local and an

Table 20: New H I Cloud Properties: M81 Group

Cloud	Coordinate Designation	Peak Flux Density (Jy)	V$_{hel}$ (km s^{-1})	σ_V (km s^{-1})	M$_{HI}$ [1] ($\times 10^7 M_\odot$)
1	GBC J095007.2+695556	0.11 ± 0.08	165	50	1.47 ± 0.35
2	GBC J100250.7+681949	0.10 ± 0.08	-105	55	2.25 ± 0.49
3	GBC J095244.9+681250	0.12 ± 0.08	11	82	2.67 ± 0.65
4	GBC J100145.0+691631	0.30 ± 0.08	72	28	8.37 ± 1.75
5	GBC J095506.3+692205	0.07 ± 0.08	280	36	0.69 ± 0.27

---

[a] Assuming the M81 distance, $D = 3.63 \pm 0.34$ Mpc from Karachentsev et al. (2004).

extragalactic origin (Ben Bekhti et al., 2006; Westmeier et al., 2008). If the clouds are located at the distance of NGC 2403 (3.3 Mpc), their masses are 1.5 to 51.7 × 10^6 $M_\odot$ and their diameters range from $\sim$ 9-25 kpc. If, instead, the clouds are within the distance bracket for Complex A given in van Woerden et al. (1999a), their masses are between 2 and 475 $M_\odot$ and their diameters are between 10 and 75 pc. Either of these sets of numbers is plausible: the H I clouds discovered in the M81/M82 group had masses $\sim 10^7$ $M_\odot$ and diameters $\sim$ 10 kpc; likewise, Milky Way H I clouds are found with masses $\sim$ 60 $M_\odot$ and sizes $\sim$ 10 pc (Stil et al., 2006).

Clouds 6 (GBC J073236.0+654302) and 7 (GBC J072528.5+654922) are unresolved in the GBT beam. However, the structure of Cloud 8 (GBC J073612.1+673325) was further analyzed. The cloud has the cometary or 'head-tail' structure, velocity gradient, and velocity-dispersion gradient observed in many Milky Way HVCs (see Chapter 1). These features are all presented in Figure 31. This type of structure is indicative of ram pressure interaction between a moving cloud and an ambient medium, i.e., the warm gaseous halo of a galaxy (Quilis & Moore, 2001). If Cloud 8 is at the distance of the NGC 2403 group, then it is located $\geq$ 90 kpc from any group galaxy, and is far from the outer regions of these galaxies. It is thus likely that the cloud is part of the Milky Way, and interaction with the Milky Way halo is the source of its head-tail structure.

We also compared the velocity distributions of the NGC 2403 H I clouds, the group galaxies, and the Milky Way HVCs in the direction of the NGC 2403 group; see Figure 32. If the new clouds are part of the NGC 2403 galaxy group, their velocity

Table 21: New H I Cloud Properties: NGC 2403 Group

Cloud	Coordinate Designation	$D_{NGC2403}$ (kpc)	T_{peak} (K)	V_{hel} (km s^{-1})	σ_v (km s^{-1})	M_{HI} $(\frac{D}{10kpc})^{-2}$ ($M_\odot$)
6	GBC J073236.0+654302	28.0	0.06	-150	20	14
7	GBC J072528.5+654922	73.2	0.15	-114	20	57
8	GBC J073612.1+673325	120.1	1.97	-205	30	475

distribution ought to be consistent with that of the galaxy group (Chynoweth et al., 2008). The average cloud velocity is -142 km s^{-1}, separated by 250 km s^{-1} from the NGC 2403 galaxy group average velocity of 113 km s^{-1}. The velocity distribution of the clouds is consistent with the velocity of Milky Way HVCs in that direction (van Woerden et al., 2004). Therefore the clouds are likely to be newly discovered compact components of Complex A or other compact Milky Way HVCs rather than members of the NGC 2403 group.

5.3.3 M81 Filament

A moment map of the H I column density is presented in Figure 33. We discovered 5 new H I clouds in the mapped region of the M81 Filament. These clouds are designated Clouds 9-13. Their locations are marked in Figure 33. Table 22 lists their properties. Spectra are shown in Figure 35. The clouds are briefly described below.

Cloud 9 (GBC J092635.8+702850) is to the northwest of the M81 group. With a velocity of -178 km s^{-1}, Cloud 9 is most likely part of Complex A. Cloud 10 (GBC J101926.3+675222) is south of IC 2574 and an adjacent HIJASS source, HIJASS

Table 22: M81 Filament H I Cloud Properties

Cloud	Coordinate Designation	ΔD_{M81} (kpc)	T_{peak} (K)	V_{LSR} (km s^{-1})	σ_v (km s^{-1})	M_{HI} $(\frac{D}{3.63Mpc})^{-2}$ $\times 10^6 M_\odot$
1	GBC J095007.2+695556	65	0.11	168	50	14.7
2	GBC J100250.7+681949	63	0.10	-102	55	22.5
3	GBC J095244.9+681250	57	0.12	14	82	26.7
4	GBC J100145.0+691631	38	0.30	74	28	83.7
5	GBC J095506.3+692205	21	0.07	283	36	6.9
6	GBC J073236.0+654302	900	0.06	-147	20	1.8
7	GBC J072528.5+654922	937	0.15	-113	20	7.5
8	GBC J073612.1+673325	826	1.97	-202	30	62.6
9	GBC J092635.8+702850	186	0.13	-178	57	3.6
10	GBC J101926.3+675222	161	0.20	38	26	3.4
11	GBC J091952.7+680937	218	0.17	-108	42	5.1
12	GBC J1022:39.1+684057	159	0.30	69	68	12.0
13	GBC J071051.4+654428	1024	0.19	-301	47	2.8

J1021+6840 (Boyce et al., 2001). Cloud 11 (GBC J091952.7+680937) is to the southwest of the M81 group and has a velocity of -108 km s^{-1}. Cloud 12 (GBC J1022:39.1+684057) is located near the previously reported HIJASS source. This cloud is relatively bright and is a few arc-minutes east of the HIJASS source. Boyce et al. (2001) find the HIJASS source is extended in the direction of IC 2574. Our observations have higher angular resolution, and in these observations Cloud 12 is clearly separated from HIJASS J1021+6840. Cloud 13 (GBC J071051.4+654428) is west of the clouds reported in Chynoweth et al. (2009) and shows a high negative velocity. It is visible in 5 channels and is extended spatially. It is offset by about 100 km s $^{-1}$ from Complex A, and may likely be a separate Milky Way HVC.

Table 23: New H I Cloud Properties: Canes I

Cloud	Coordinate Designation	T_{peak} (K)	V_{hel} (km s^{-1})	σ_v (km s^{-1})	M_{HI} ($\times 10^7$ $M_\odot$)
14	GBC J122412.0+380016	0.023	646	67	2.77 ± 1.51
15	GBC J122153.0+375918	0.024	569	57	2.15 ± 1.02

5.3.4 Canes I Group

Two new H I clouds are identified in the Canes I group, designated Clouds 14 (GBC J122412.0+380016) and 15 (GBC J122153.0+375918). Their properties are shown in Table 23. The distance to the clouds was calculated using $D = cz/H_0$, where H_0 is the Hubble constant, assumed to be 75 km s^{-1} Mpc^{-1}. Using these distances, they are similar in mass to the clouds in the M81 group. They are unresolved in the GBT beam, so their substructure is unknown. They are located near the Canes I group galaxy NGC 4244, which has a velocity of 244 km s^{-1}. This is a difference of > 300 km s^{-1}, so the clouds are not likely to be associated with NGC 4244. They are also near the background galaxy KUG 1218+387, which has a velocity of 587 km s^{-1} and a mass of 8.6×10^7 $M_\odot$. The clouds, then, are most likely associated with KUG 1218+387 and not part of the Canes I group. It is possible that these clouds are actually undiscovered companion galaxies to KUG 1218+387. Follow-up sensitive optical observations would be necessary to determine whether these clouds are associated with a stellar component.

5.3.5 NGC 672 and NGC 45 Groups

We detect no H I clouds in the NGC 672 or NGC 45 group above our mass detection thresholds. Although some of the column density maps appear to show emission not associated with known galaxies, these objects are found not to have coherent velocity structure. Therefore, these groups do not contain H I clouds that are more massive than our observational limits. It is important to note that these two groups are the most distant of our observed sample, and therefore our observations are less sensitive for these groups (see Figure 22). More sensitive observations of these two groups would be necessary in order to better constrain their H I properties.

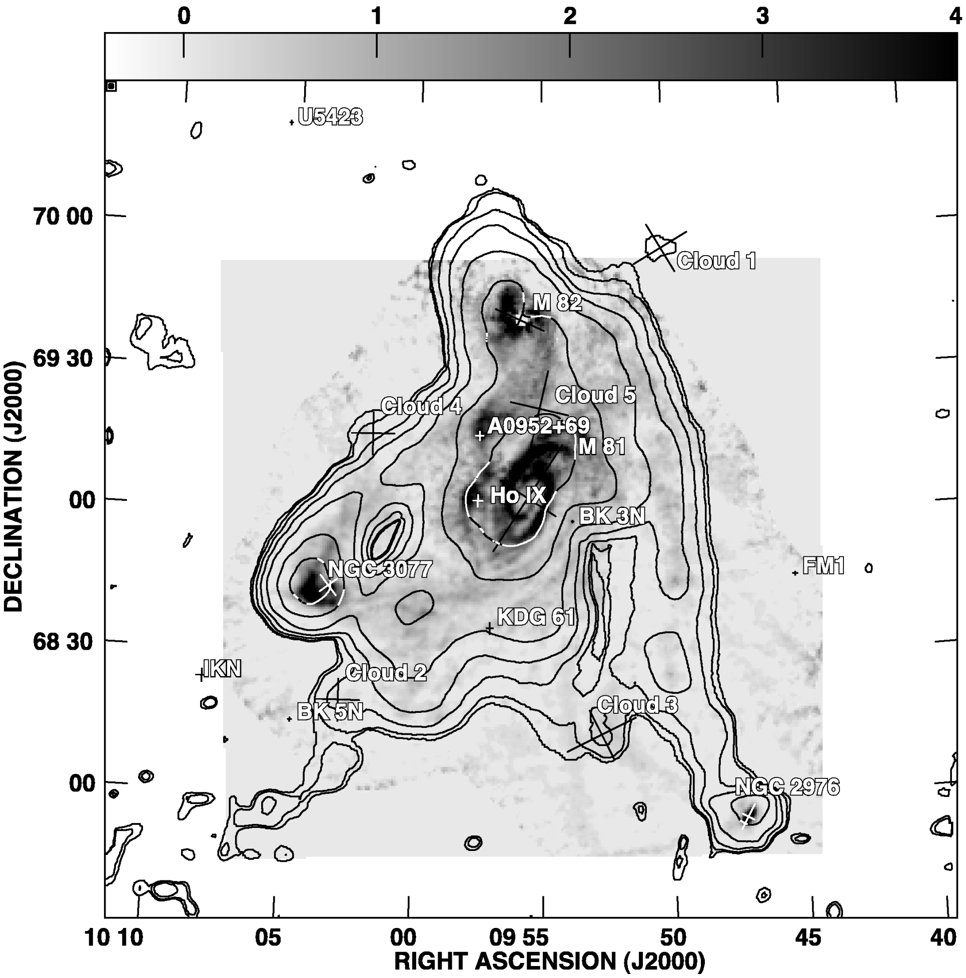

Figure 23: The contours show the GBT H I integrated column density map of the field observed. Galaxy locations and new H I clouds are marked. Contours are overlaid at 1000 Jy beam^{-1} × km s^{-1} × (15, 30, 75, 150, 300, 750, 1500 and 3000). The velocity range included is -250 to 340 km s^{-1}. The integrated column density map from the VLA observations of Yun et al. (1994) is shown in greyscale over the range -400 to 4000 Jy beam^{-1} × km s^{-1}.

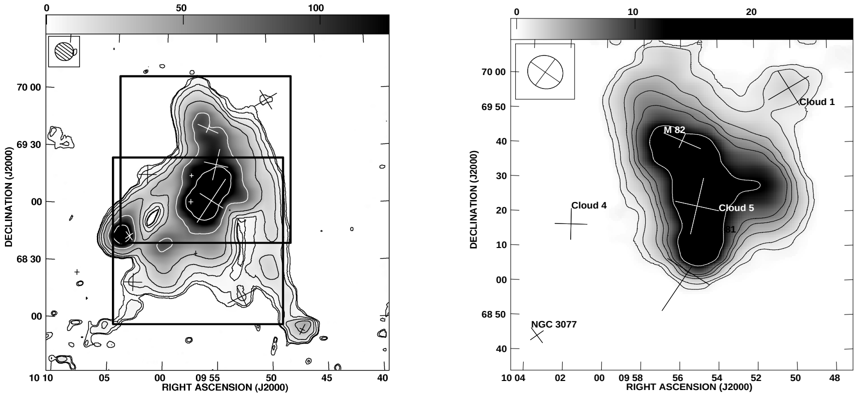

Field of View (-250 to 340 km s^{-1})

Cloud 1 (160 to 185 km s^{-1})

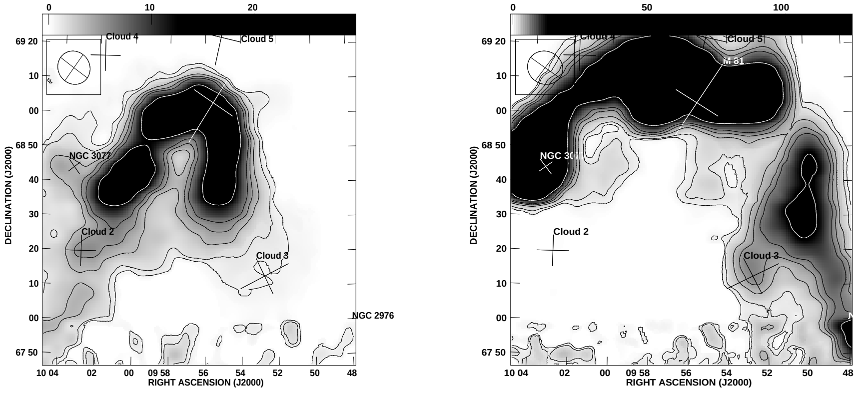

Cloud 2 (-115 to -80 km s^{-1})

Cloud 3 (5 to 75 km s^{-1})

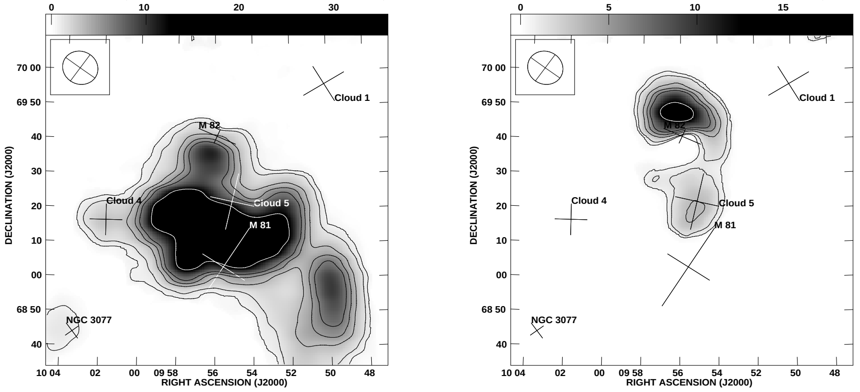

Cloud 4 (75 to 95 km s^{-1})

Cloud 5 (270 to 320 km s^{-1})

Figure 24: Contour maps of each H I cloud candidate, overlaid with H I column density maps of the velocity range in which each cloud is detected. These figures are included to show the distinct nature of the H I clouds in velocity space. The greyscale is 0 to 12.5 kJy/beam × km/sec. Contour levels are 65 Jy/beam × km/sec × (10, 20, 50, 75, 100, 200, 500, 10000). The top left-hand panel shows the zoom regions for the contour plots; the upper box includes Clouds 1, 4, 5 and the lower box includes Clouds 2 and 3. Below each map, the velocity range summed into the integrated intensity map is indicated.

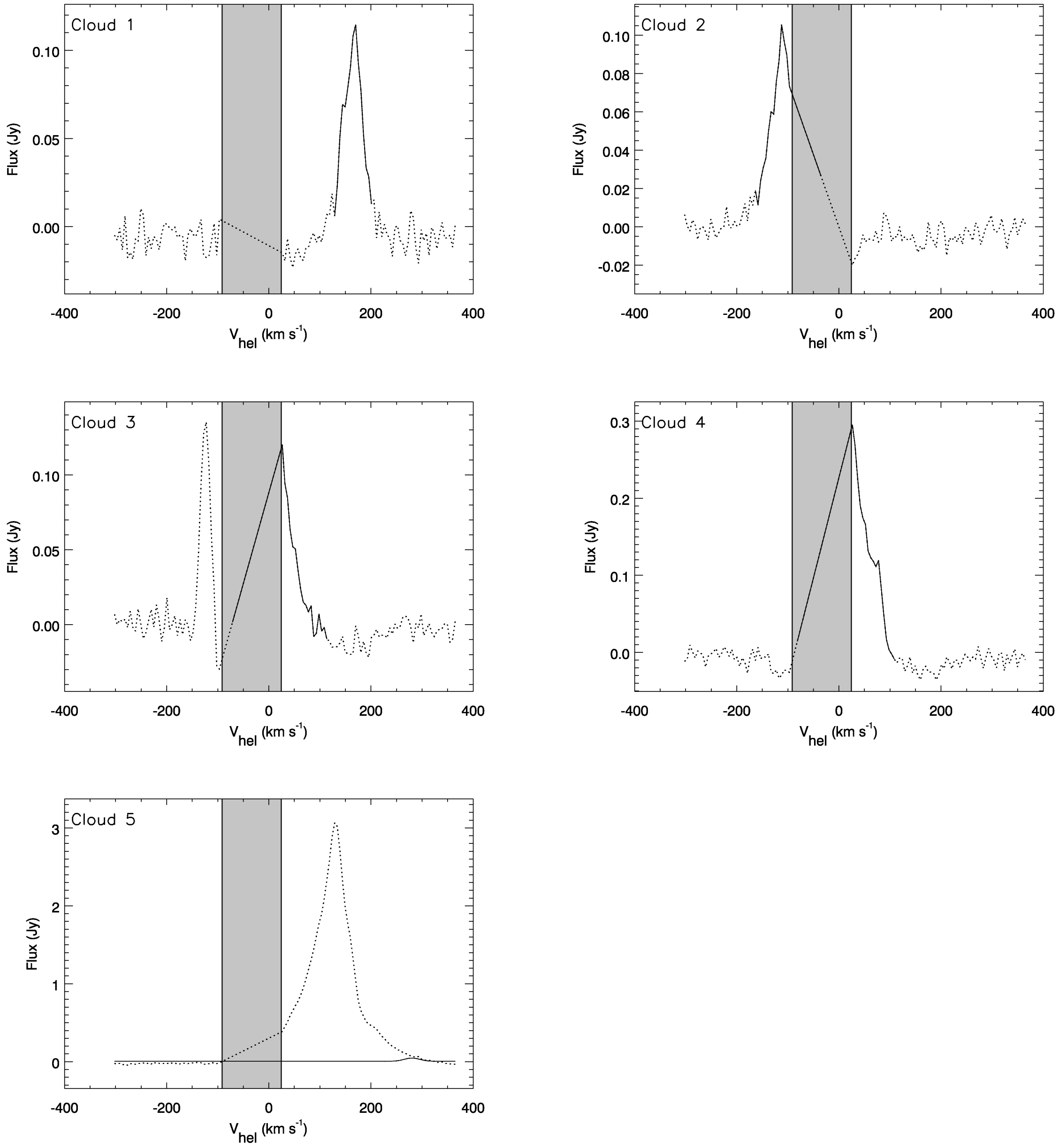

Figure 25: H I profiles for Clouds 1-5. The solid line indicates the range that was summed in order to calculate the cloud mass. For Cloud 5, note that M82 dominates the emission. The data (dashed line) along with Gaussian fit for Cloud 5 (solid line) are plotted. Note that the velocity range from -85 to 25 km s^{-1} is interpolated to remove foreground gas

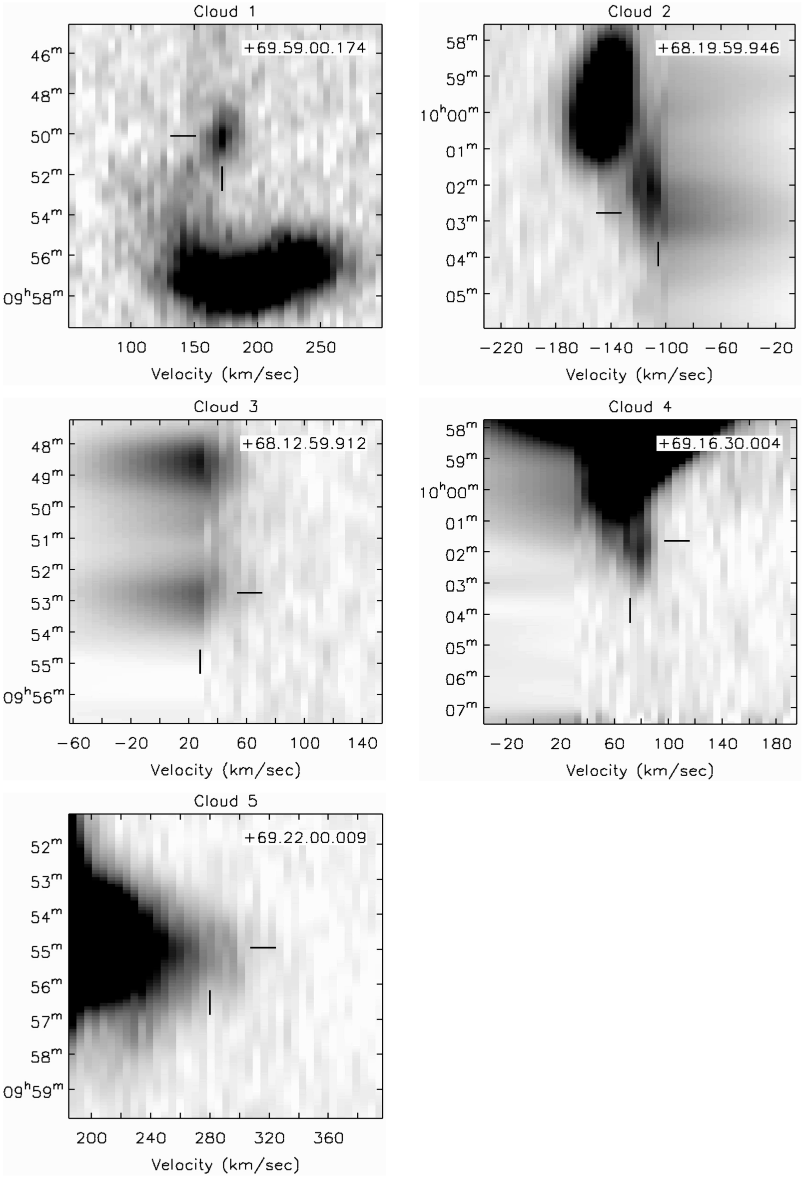

Figure 26: PV diagrams for Clouds 1-5. Note that the clouds are distinct from galaxies in velocity space. Each cloud is located approximately in the center of the diagram, marked by pointers. Each diagram extends ± 100 km s^{-1} from the cloud's peak velocity. The PV cut runs through the center of the clouds in declination, and the diagram is centered on the cloud in right ascension. The greyscale runs from -0.02 to 0.2 Jy $beam^{-1}$. The parent galaxy for each cloud are also visible in the PV diagrams.

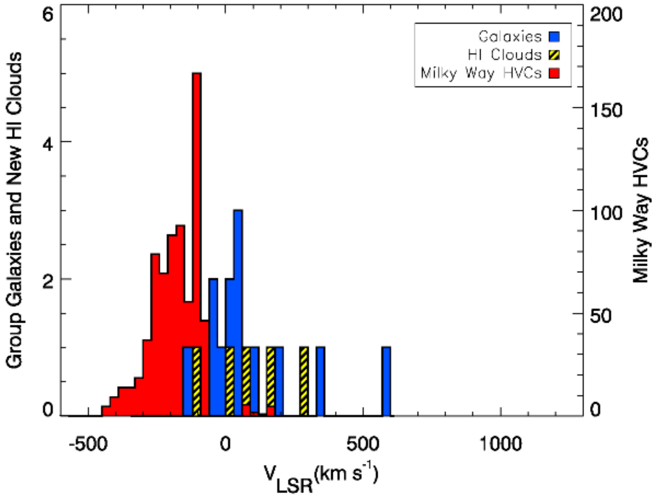

Figure 27: Velocity distribution of M81 group galaxies, Clouds 1-5, and Milky Way HVCs in the direction of the M81 group from van Woerden et al. (2004). The new H I clouds have velocities consistent with the group galaxies.

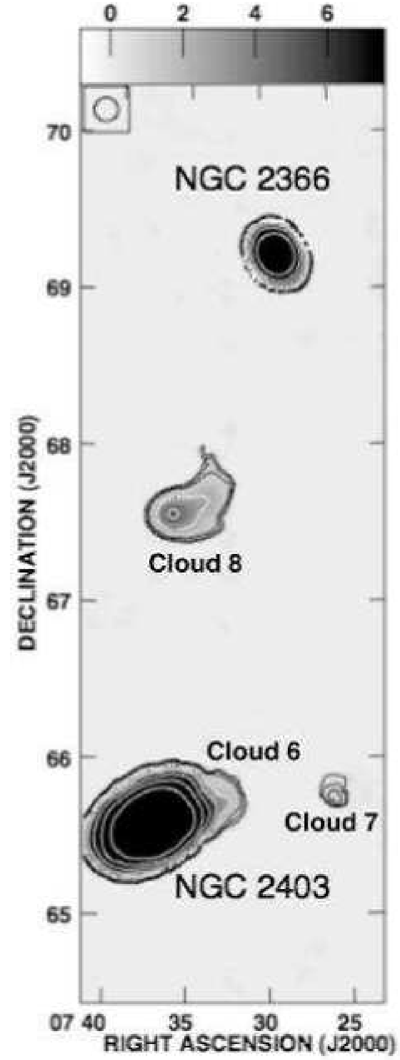

Figure 28: NGC 2403 Group Region 1 integrated H I column density map. The galaxies are labeled and the newly discovered H I feature are numbered. Velocity range: -260 to +335 km s^{-1}. Channels contaminated by foreground gas are not included in the map. The greyscale is -0.75 to 7.5 Jy beam^{-1} × km s^{-1}. Contours are at 5σ, 7σ, 10σ, 25σ, 50σ, 100σ, 200σ.

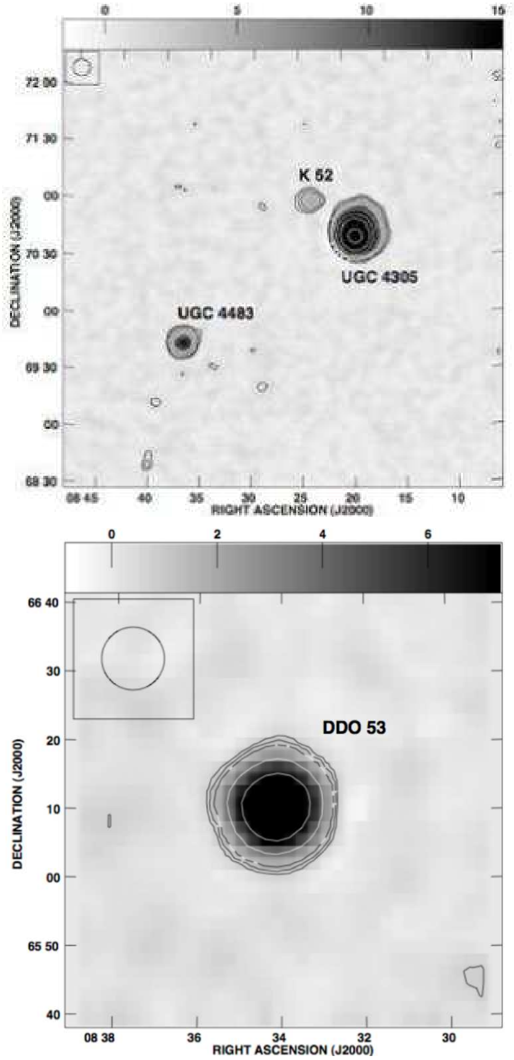

Figure 29: Top: Region 2. Integrated H I column density map, 80 to 220 km s^{-1}. Greyscale: -1.5 to 15 Jy beam^{-1} × km s^{-1}. Contours are at 5σ, 7σ, 10σ, 25σ, 50σ, 100σ, 200σ. Bottom: DDO 53. Integrated H I column density map, 25 to 65 km s^{-1}. Greyscale: -0.725 to 7.25 Jy beam^{-1} × km s^{-1}. Contours are at 5σ, 7σ, 10σ, 25σ, 50σ, 100σ, 200σ.

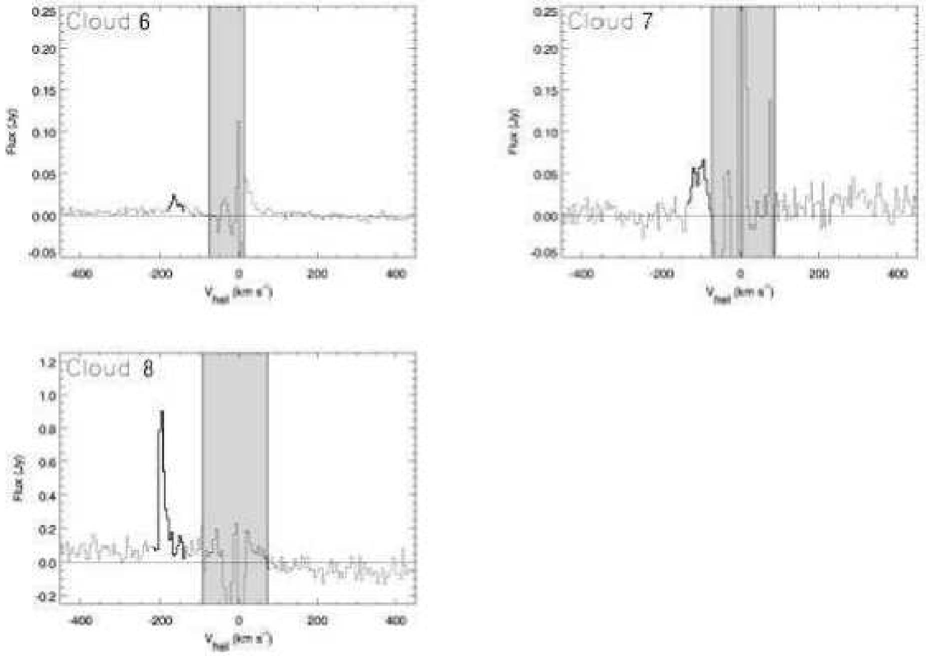

Figure 30: H I intensity profiles of Clouds 6,7, and 8. The regions of the spectrum used to calculate H I mass are highlighted in bold. The velocity ranges contaminated by foreground gas are indicated with gray boxes.

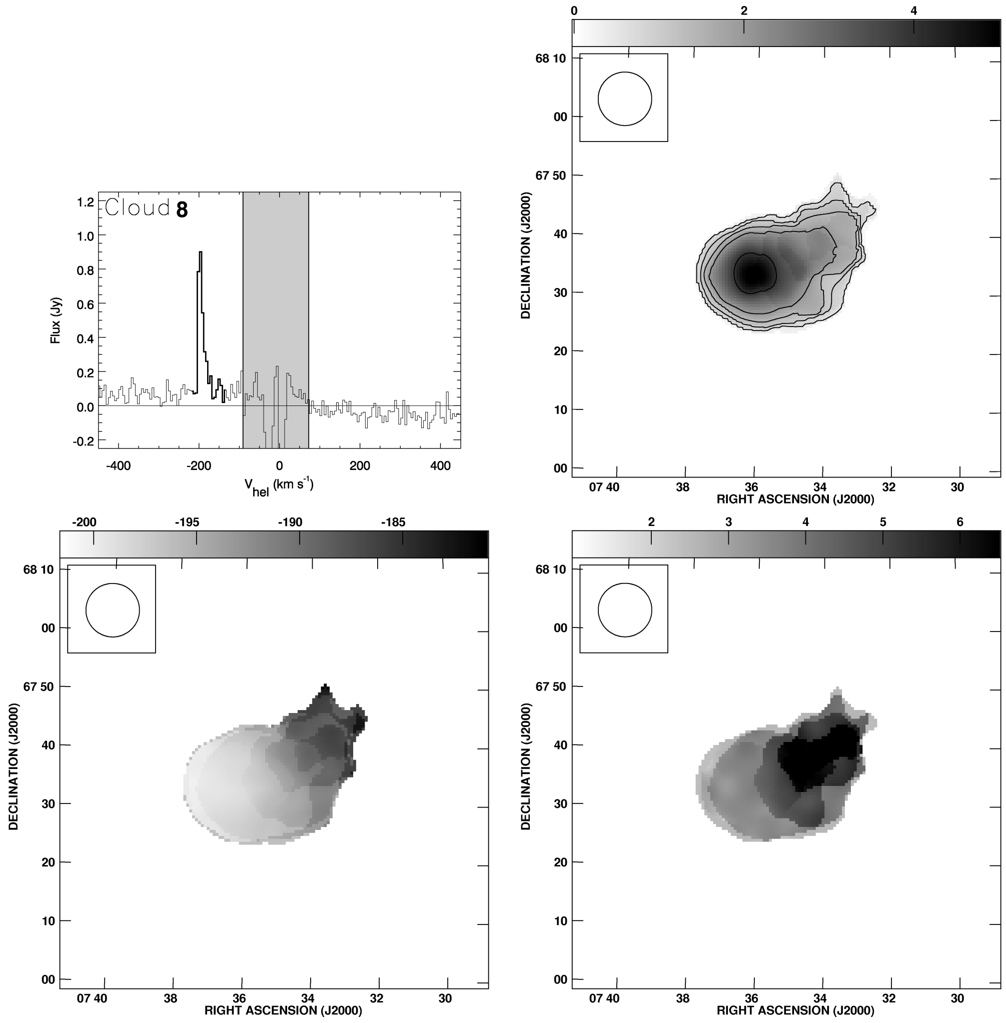

Figure 31: Detailed maps of Cloud 8. Note the prominent head-tail structure. From top left: H I intensity profile, H I column density (grayscale: 0 to 5 Jy beam^{-1} × km s^{-1}), velocity (grayscale: -200 to -180 km s^{-1}), velocity dispersion (grayscale: 1 to 6.5 km s^{-1}). Maps are integrated from -240 to -160 km s^{-1}.

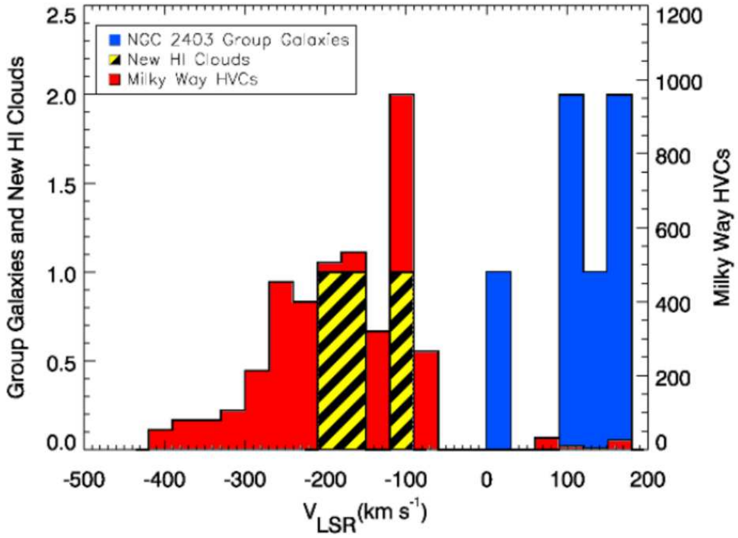

Figure 32: Velocity distribution of NGC 2403 group galaxies, new H I cloud detections, and Milky Way HVCs in the direction of the NGC 2403 group from van Woerden et al. (2004). The new H I clouds have velocities consistent with the Milky Way HVCs, but inconsistent with the group galaxies.

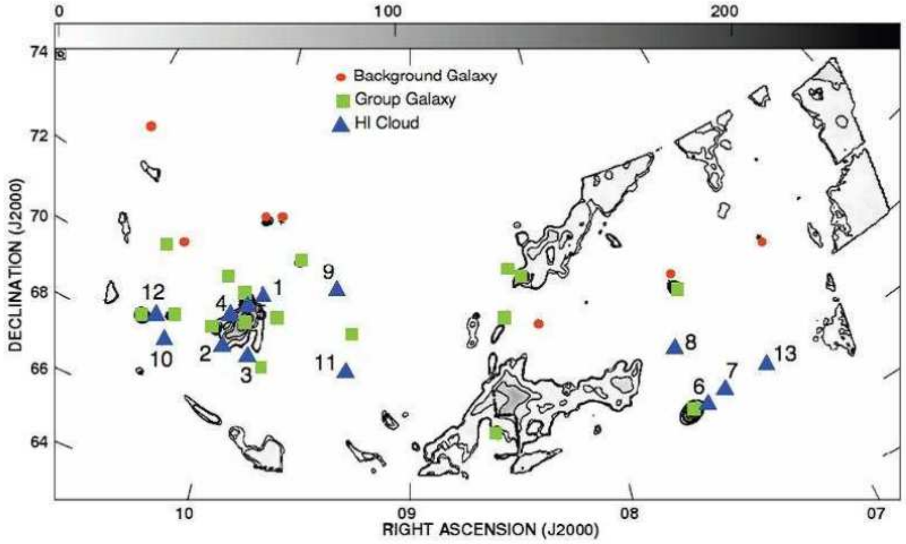

Figure 33: H I column density map of the observed area of the M81 Filament. Background galaxies, group galaxies, and H I clouds are marked. The diagonal filament of H I through the middle of the map is Milky Way HVC Complex A.

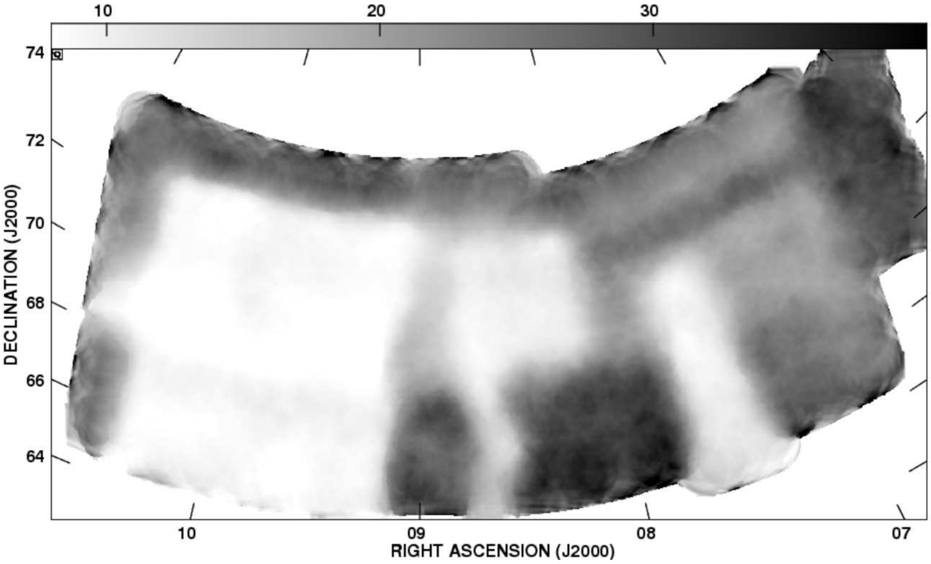

Figure 34: Sensitivity of the mapped area of the M81 Filament. The greyscale ranges from 8 to 40 mJy beam^{-1}, corresponding to mass sensitivity of 2.5 to 12.9 $\times$ 10^5 $M_\odot$. The colorbar above the figure is in units of mJy beam^{-1}.

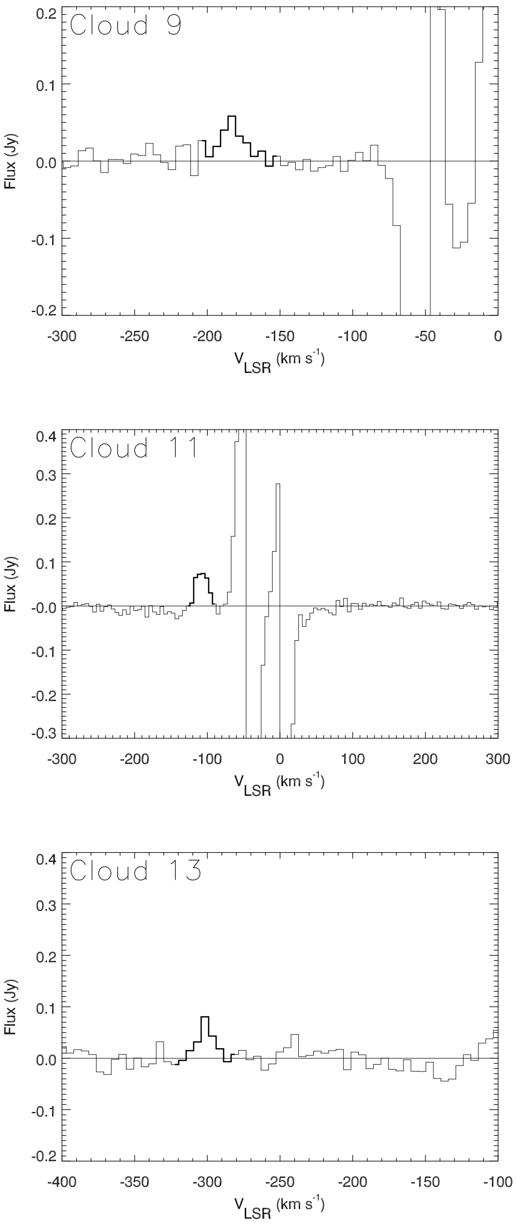

Figure 35: H I intensity profiles of new H I Clouds 9-13. The regions of the spectrum used to calculate H I mass are highlighted in bold.

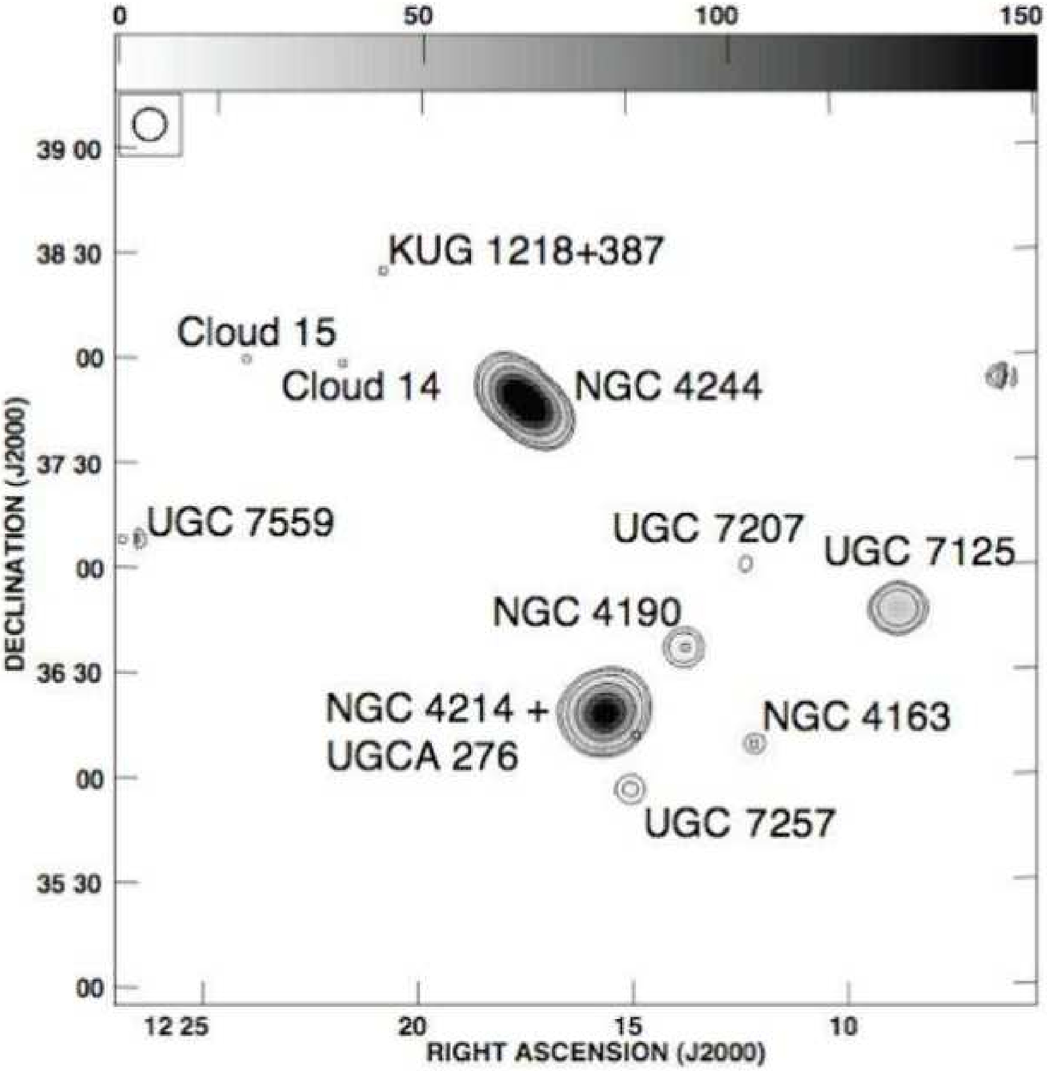

Figure 36: H I column density map of a region of the Canes I group. Group galaxies, background galaxies, and H I clouds are labeled. All flux above 1σ is included. Grayscale: 0-150 Jy beam^{-1} × km s^{-1}. Contours: 2 Jy beam^{-1} × km s^{-1} ×(-3,3,5,10,25,50,100,250)

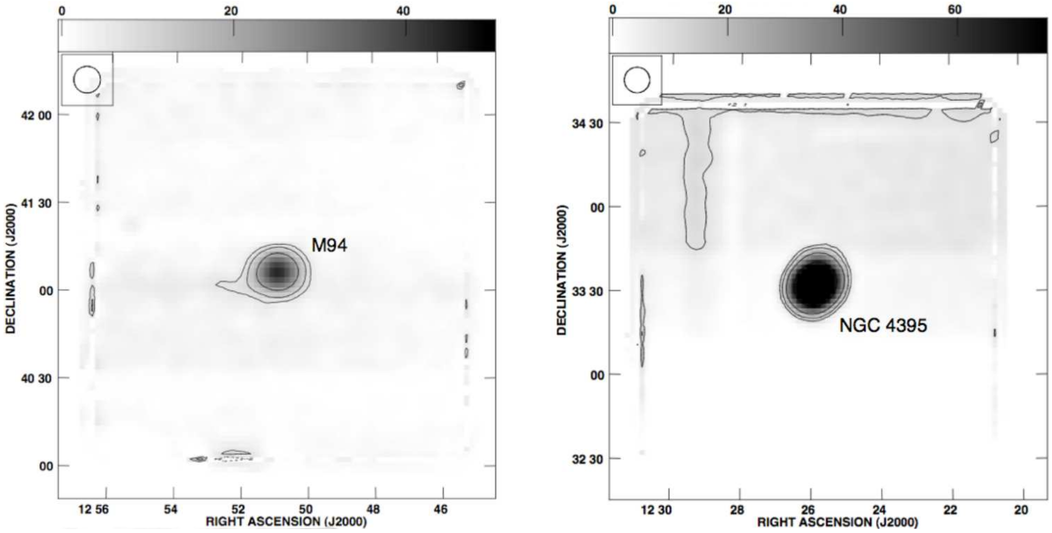

Figure 37: Left: H I column density map of M94. Grayscale: 0-50 Jy beam^{-1} × km s^{-1}. Contours: 2 Jy beam^{-1} × km s^{-1} ×(-3,3,5,10,25,50,100,250. Right: H I column density map of NGC 4395. Grayscale: 0-75 Jy beam^{-1} × km s^{-1}. Contours: 2.75 Jy beam^{-1} × km s^{-1} ×(-3,3,5,10,25,50,100,250)

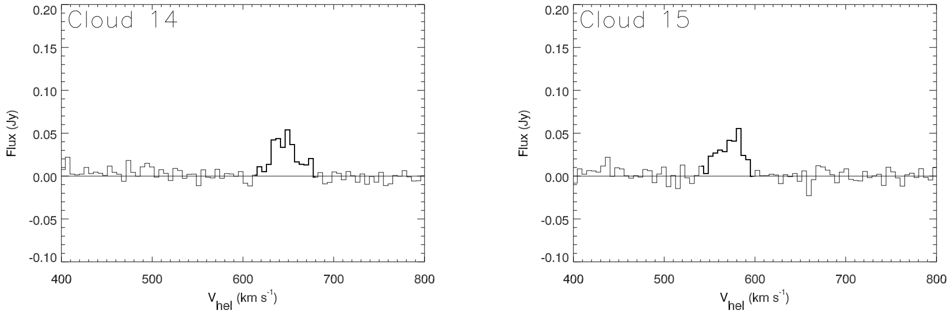

Figure 38: Line profiles of H I clouds 14 and 15, discovered in the direction of the Canes I galaxy group.

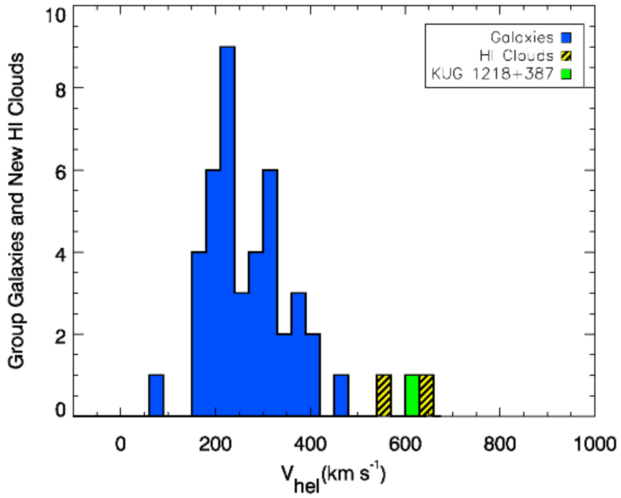

Figure 39: Velocity distribution of Canes I Group galaxies, H I cloud detections, and KUG 1218+387. Note that the H I clouds appear to be kinematically associated with KUG 1218+387 rather than the Canes I group.

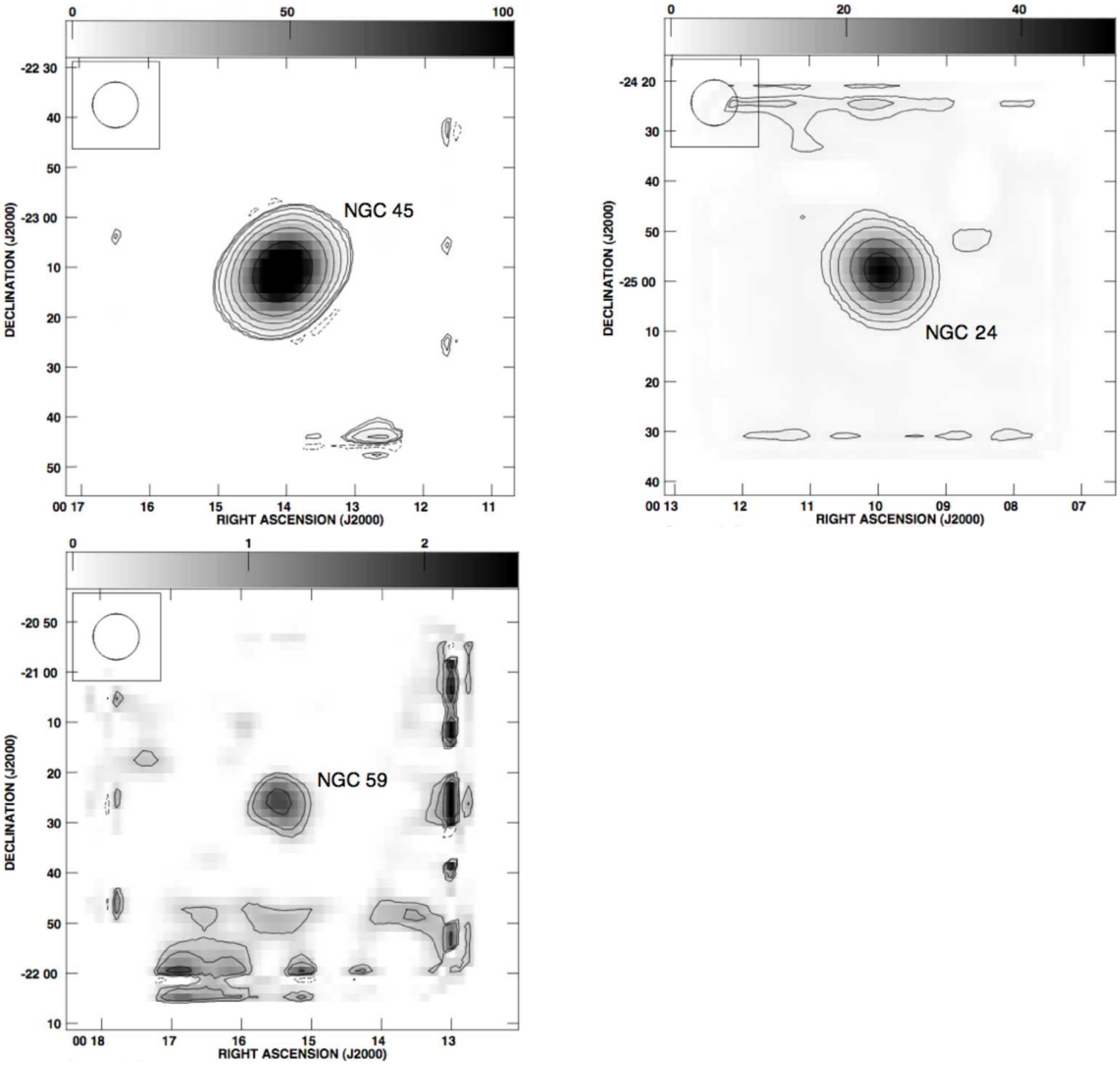

Figure 40: NGC 45 group galaxies. Any extraplanar emission is due to noise, since it does not have coherent velocity structure. Top Left: H I column density map of NGC 45. Grayscale: 0-100 Jy beam^{-1} × km s^{-1}. Contours: 0.30 Jy beam^{-1} × km s^{-1} ×(-3,3,5,10,25,50,100,250. Top Right: H I column density map of NGC 24. Grayscale: 0-50 Jy beam^{-1} × km s^{-1}. Contours: 0.75 Jy beam^{-1} × km s^{-1} ×(-3,3,5,10,25,50,100,250). Bottom Left: H I column density map of NGC 59. Grayscale: 0-2.5 Jy beam^{-1} × km s^{-1}. Contours: 0.15 Jy beam^{-1} × km s^{-1} ×(-3,3,5,10,25,50,100,250)

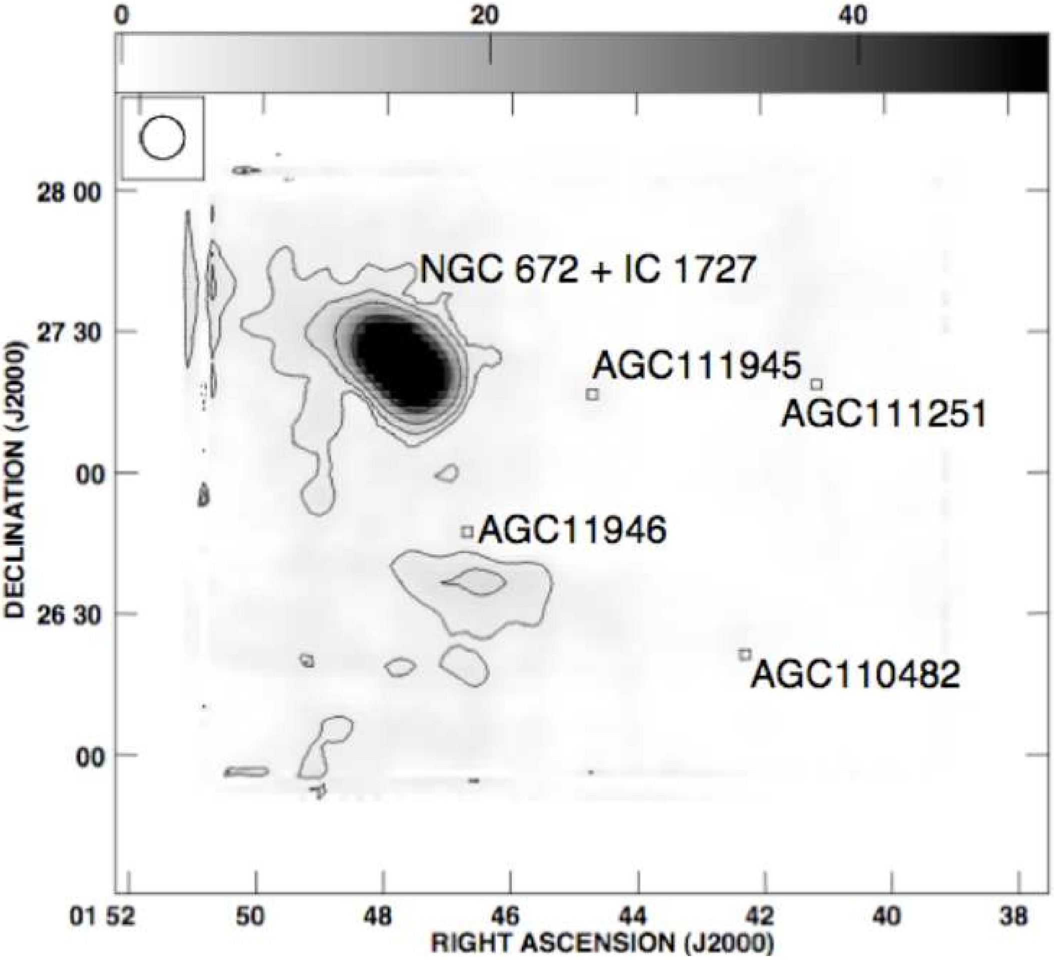

Figure 41: H I column density map of a region of the NGC 672 group. Any emission not associated with labeled galaxies is due to noise, since it does not have coherent velocity structure. Grayscale: 0-115 Jy beam^{-1} × km s^{-1}. Contours: 3.25 Jy beam^{-1} × km s^{-1} ×(-3,3,5,10,25,50,100,250)

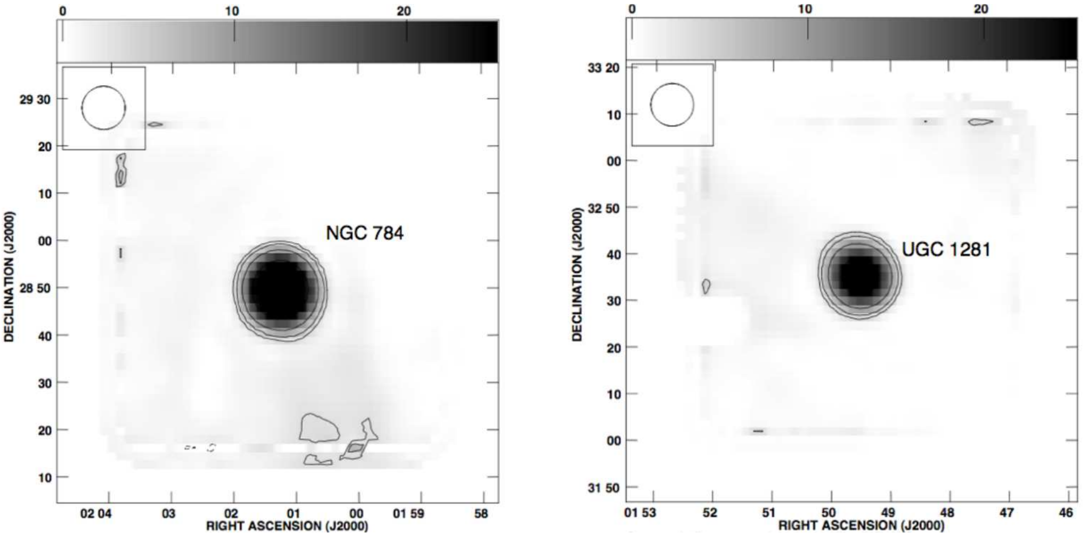

Figure 42: Left: H I column density map of NGC 784. Grayscale: 0-25 Jy beam^{-1} × km s^{-1}. Contours: 1.0 Jy beam^{-1} × km s^{-1} ×(-3,3,5,10,25,50,100,250. Right: H I column density map of UGC 1281. Grayscale: 0-25 Jy beam^{-1} × km s^{-1}. Contours: 1.0 Jy beam^{-1} × km s^{-1} ×(-3,3,5,10,25,50,100,250)

CHAPTER VI

ANCILLARY DATA: GALAXY MASSES AND SPECTRA

H I masses of all galaxies observed are easily calculated from our observations. Galaxy spectra and H I masses will be valuable for future studies of the H I properties of nearby galaxies, and are presented in the following sections.

6.1 M81 Group

There is some overlap in velocity space between the M81/M82 group and the Milky Way, and over this velocity range we can not discriminate between local and distant emission. To estimate the total H I mass of neutral hydrogen for the M81/M82 group we replaced the velocity channels contaminated by Milky Way and local high velocity clouds with interpolated values computed from spectral line observations at -85 and +25 km s^{-1}.

The spectrum of the entire field used to compute the neutral hydrogen mass of the group is shown in Figure 43. The computed mass was $10.46 \pm 2.86 \times 10^9$ $M_\odot$. For this mass and all following mass estimates, the error estimates are 1σ. The dominant error contribution is the uncertainty in the absolute calibration. Our total mass value is greater than the values found by Appleton et al. (1981) and Yun (1999) . Our study is more sensitive to faint, extended emission over the entire field than either of these previous studies.

Table 24: Calculated Galaxy Masses: M81 Group

Galaxy	H I Mass ($\times 10^9 M_\odot$)	Mass from Yun (1999)	Mass from Appleton et al. (1981)
Field of Study	10.46 ± 2.86	5.6	5.4
M81	2.67 ± 0.55	2.81 ± 0.56	2.19 ± 0.22
M82	0.75 ± 0.16	0.80 ± 0.16	0.72 ± 0.07
NGC3077	1.01 ± 0.21	0.69 ± 0.14	1.00 ± 0.10
NGC2976	0.52 ± 0.11	...	0.16 ± 0.02

The H I spectra for the major galaxies are presented in Figure 43. Neutral hydrogen masses of known galaxies were calculated to confirm the accuracy of our mass calculation methods. Our calculated values for M_{HI} are in agreement with the literature; see Table 24.

6.2 NGC 2403 Group

H I spectra for the known galaxies are presented in Figure 44. The velocity ranges affected by foreground Milky Way emission are indicated on each plot. There is some overlap in velocity space between the NGC 2403 group and the Milky Way, and over this velocity range we can not discriminate between local and distant emission. Of the galaxies, only NGC 2403 overlaps with Milky Way velocities. To estimate the total H I mass of neutral hydrogen for NGC 2403, we replaced the velocity channels contaminated by Milky Way and local high velocity clouds with interpolated values computed from spectral line observations at either end of the contaminated channels.

Our calculated values for M_{HI} are in agreement with the literature; see Table

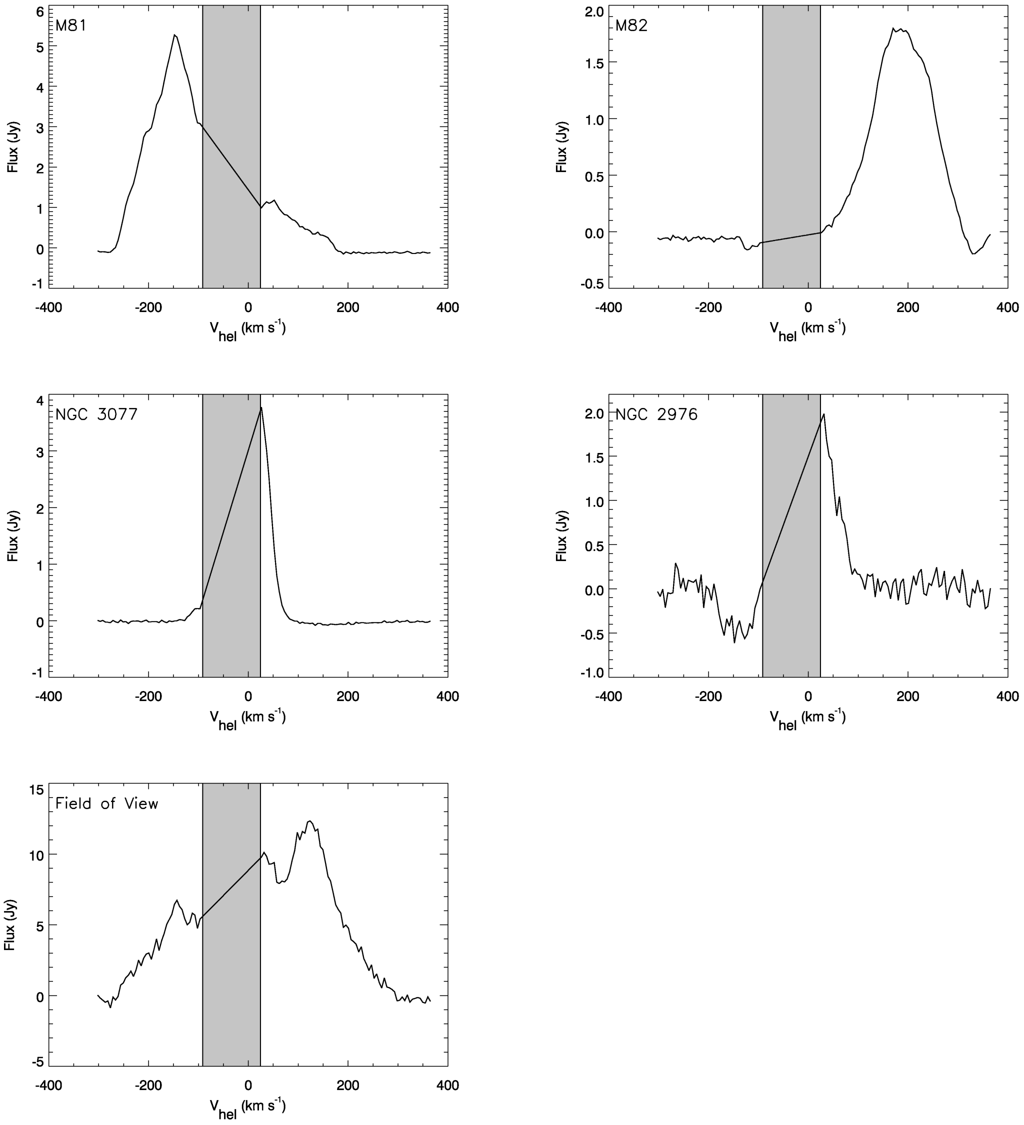

Figure 43: H I intensity profiles of major group galaxies, used to calculate H I mass. From top left: M81, M82, NGC 3077, and NGC2976. Also included is the H I spectrum of the entire area observed (bottom left). Note that the velocity range from -85 to 25 km s^{-1} is interpolated to remove foreground gas

Table 25: Calculated Galaxy Masses: NGC 2403 Group

Galaxy	H I Mass ($\times 10^9 M_\odot$)	H I Mass from Karachentsev & Kaisin (2007)
NGC 2403	3.38 ± 0.26	3.31
DDO 44	...	< 0.001
NGC 2366	0.68 ± 0.05	0.71
UGC 4483	0.04 ± 0.005	0.03
UGC 4305/HoII	0.91 ± 0.07	0.98
K 52	0.02 ± 0.004	0.01
DDO 53/UGC 4459	0.05 ± 0.004	...
VKN	...	...

25. Error estimates on the masses are 1σ. The dominant error contribution is the uncertainty in the absolute calibration, about 7% for the GBT.

6.3 M81 Filament

Because this survey encompasses such a large volume, we have detected a significant number of galaxies in H I . We calculated H I masses of all known galaxies in the observed volume.

Distances for galaxies in the M81 Filament were taken from Karachentsev & Kaisin (2007). Distances to background galaxies were taken from NED where available; otherwise, they were calculated from the radial velocity, assuming a Hubble constant of $H_0 = 75$ km s^{-1} Mpc^{-1}. Because of the high number of galaxies and continuum sources in the field, each galaxy spectrum was re-baselined using a first-order fit to the surrounding spectral region, in order to calculate an accurate H I mass.

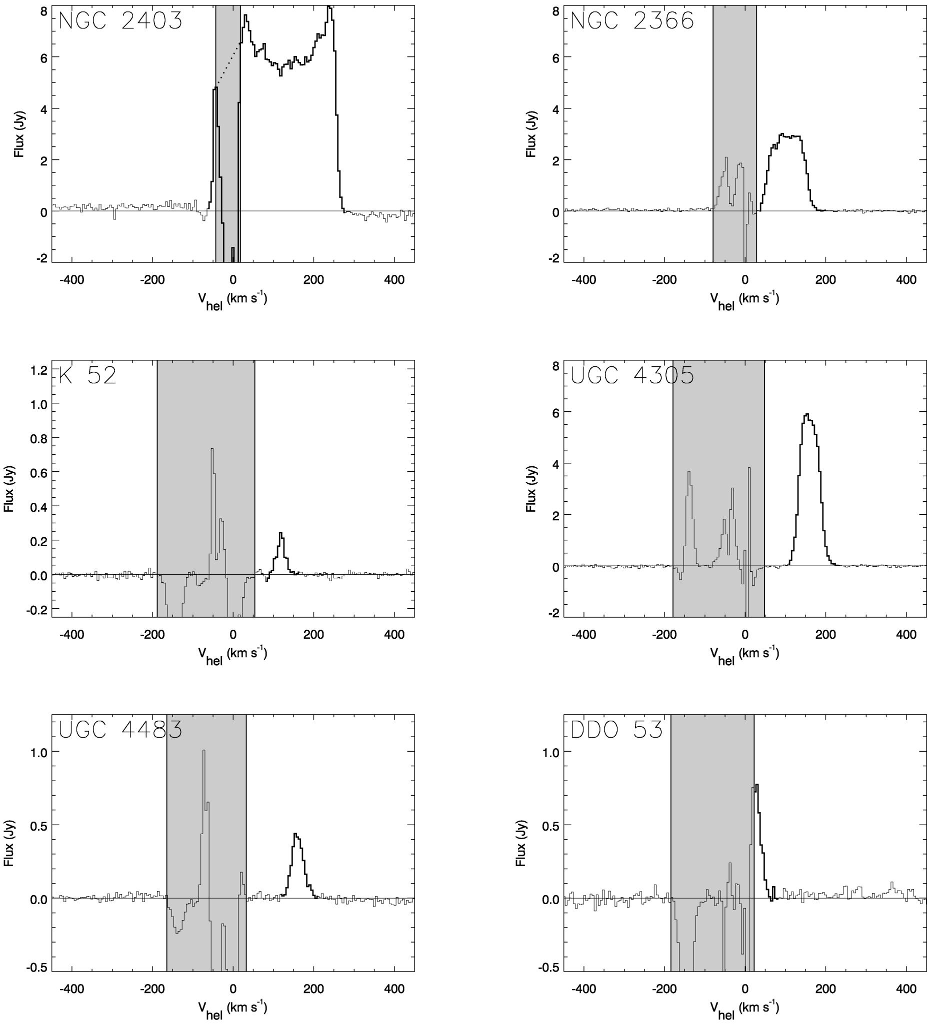

Figure 44: H i intensity profiles of major group galaxies. The regions of the spectrum used to calculate H i mass are highlighted in bold. From top left: NGC 2403, NGC 2366, K 52, UGC 4305, UGC 4483, and DDO 53. The velocity ranges contaminated by foreground gas are indicated with gray boxes.

Table 26: Calculated Galaxy Masses: M81 Filament and Background Galaxies

Name	H I Mass $\times 10^9 M_\odot$
UGC 3580*	3.32 ± 0.52
KUG 0724+695	0.27 ± 0.05
KKH 44	0.08 ± 0.02
NGC 2787	0.96 ± 0.15
Holmberg I	0.16 ± 0.03
BK1N	0.09 ± 0.02
NGC 2985*	4.70 ± 0.73
NGC 3027	6.14 ± 0.95
UGC 5423	0.03 ± 0.01
HIJASS J1021+68	0.08 ± 0.01
UGC 5612	1.25 ± 0.20
IC 2574	1.36 ± 0.21
UGC 5692*	0.006 ± 0.001
NGC 3403*	2.53 ± 0.40

The H I spectra for the known galaxies are presented in Figure 45. Calculated H I masses not in Tables 24 or 25 are presented in Table 26. Error estimates on the masses are difficult to obtain, given the wide range in rms noise values over the map; in Table 26 they are calculated using the average rms noise. Error estimates on the masses are 1σ. The dominant error contribution is the uncertainty in the absolute calibration, about 7% for these observations. The galaxies UGC 3580, NGC 2985, UGC 5692, and NGC 3403 are not completely covered by our bandwidth, so their masses are calculated only to our velocity limit of 1320 km s^{-1}.

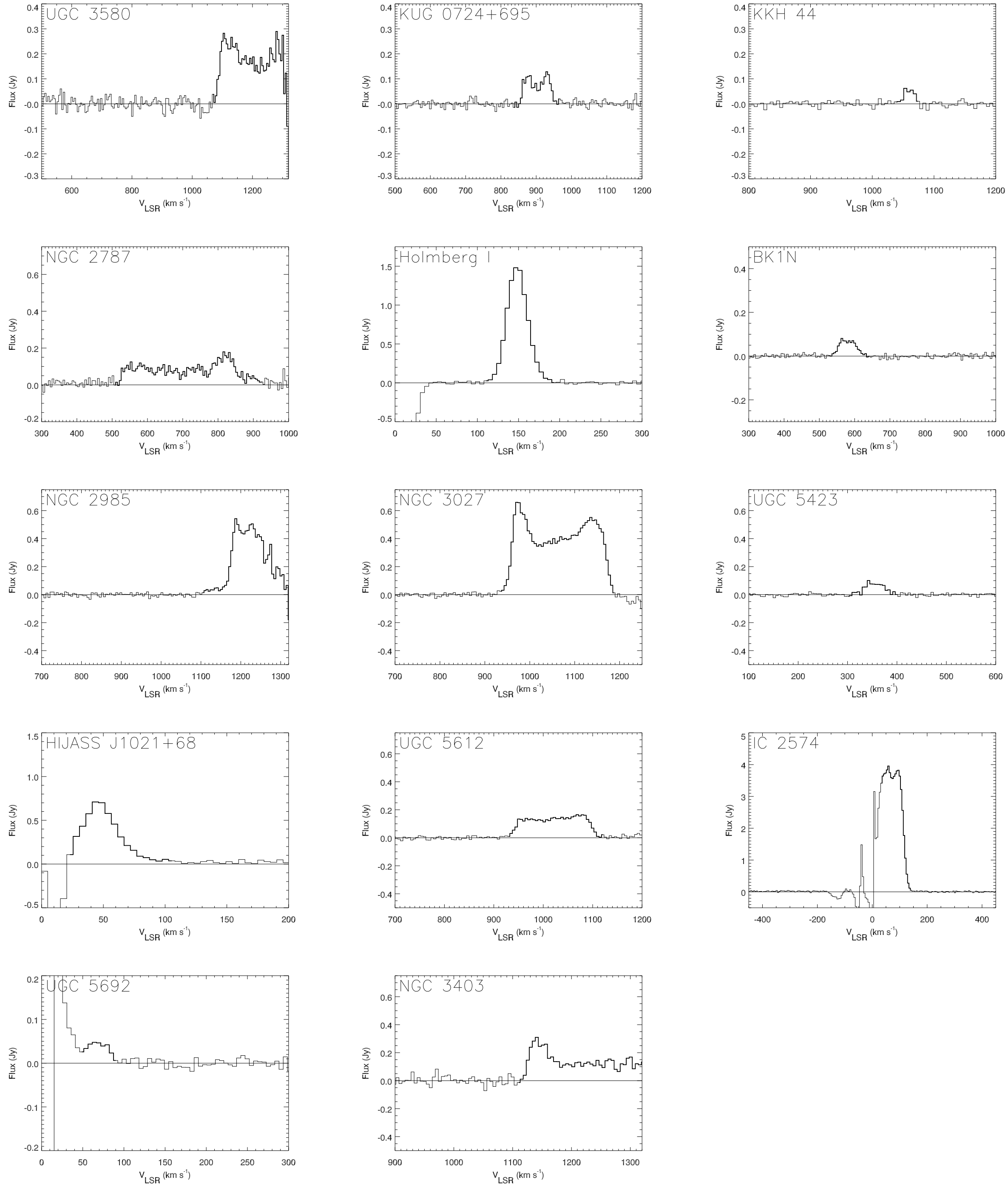

Figure 45: H I line profiles of known galaxies within our observed field. Line profiles for the galaxies in the M81 and NGC 2403 groups can be found in Chynoweth et al. (2008) and Chynoweth et al. (2009).

Table 27: Calculated Galaxy Masses: Canes I Group and Background Galaxies

Galaxy	H I Mass ($\times 10^9 M_\odot$)
UGC 7125	2.21 ± 0.36
UGC 7207	0.23 ± 0.08
UGC 7257	0.57 ± 0.11
KUG1218+387	0.09 ± 0.02
NGC 4244	2.27 ± 0.35
NGC 4214	1.12 ± 0.17
NC 4163	0.02 ± 0.001
NGC 4190	0.05 ± 0.01
M94	0.44 ± 0.07
NGC 4395	1.40 ± 0.22

6.4 Canes I Group

In the volume observed for the Canes I Group, we also observe the galaxy KUG 1218+387. Its H I mass is presented in Table 27 along with the H I masses of group galaxies.

6.5 NGC 45 Group

H I masses for the three NGC 45 group galaxies are presented in Table 28. H I spectra are shown in Figure 47. No foreground or background galaxies are detected in maps of the NGC 45 group.

6.6 NGC 672 Group

The interacting galaxies NGC 672 and IC 1727 are blended with the GBT beam. Therefore, the mass and spectra are calculated for the galaxies combined. Galaxy

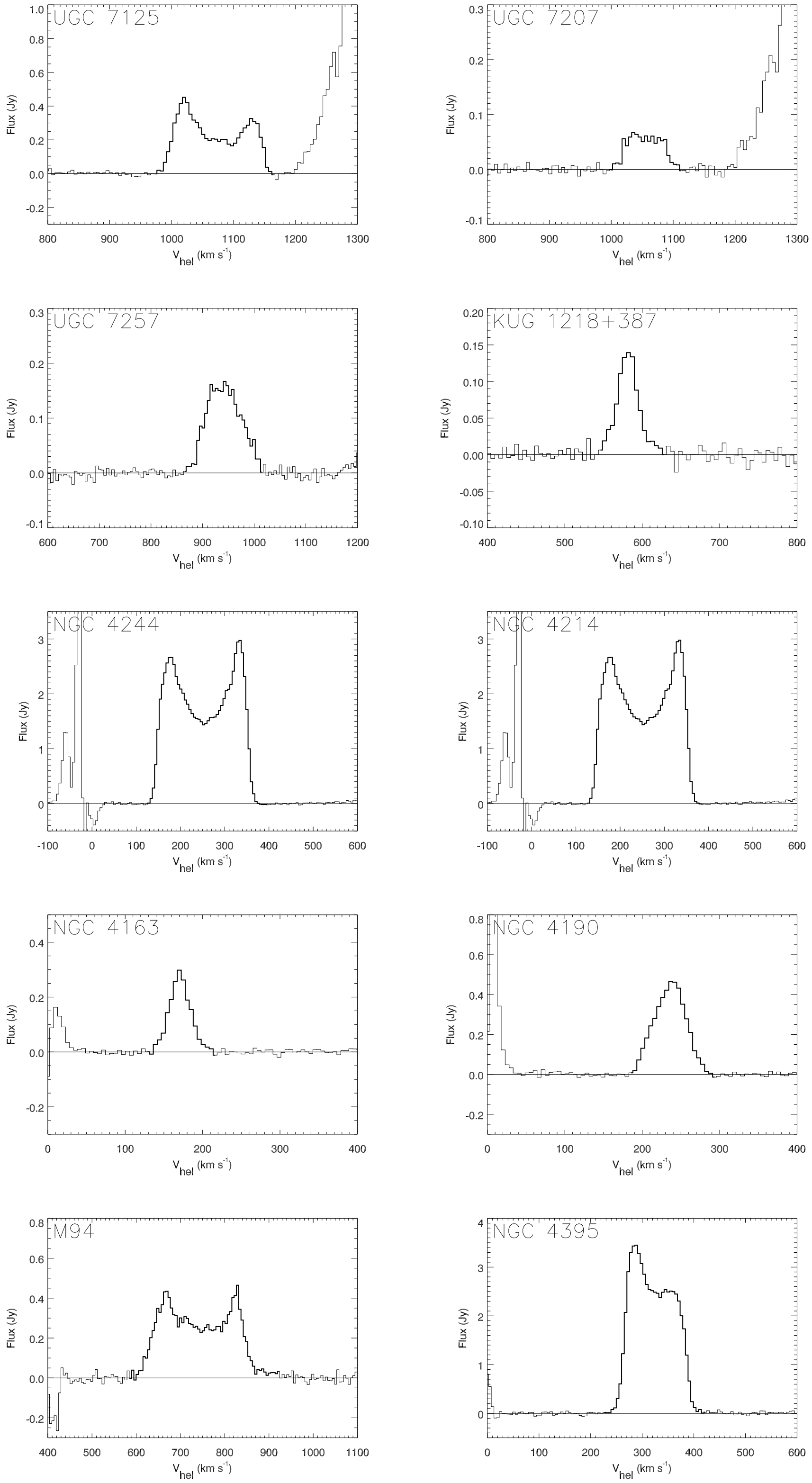

Figure 46: H I intensity profiles of major Canes I Group galaxies, used to calculate H I mass.

Table 28: Calculated Galaxy Masses: NGC 45 Group

Galaxy	H I Mass $(\times 10^9 M_\odot)$
NGC 45	2.82 ± 0.44
NGC 24	0.86 ± 0.13
NGC 59	0.02 ± 0.004

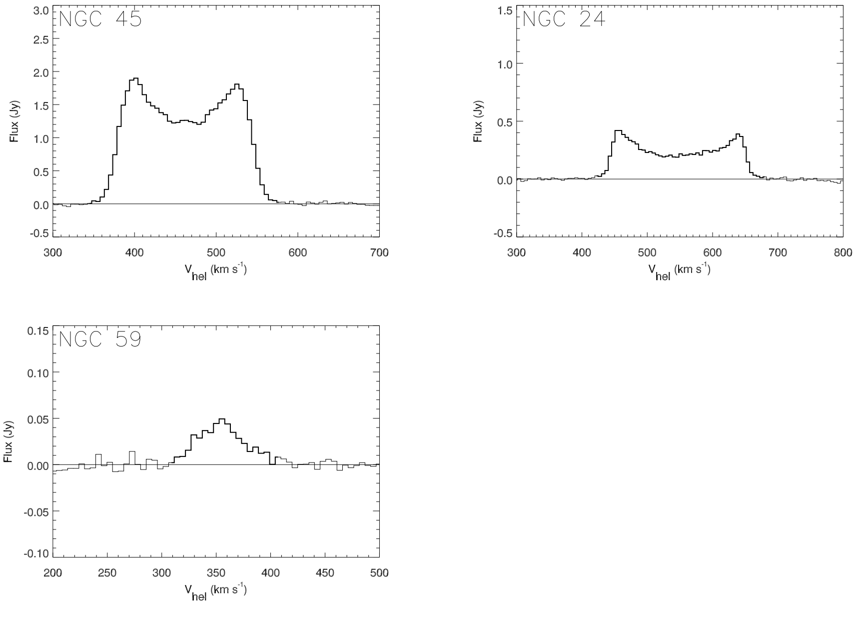

Figure 47: H I intensity profiles of major NGC 45 Group galaxies, used to calculate H I mass.

Table 29: Calculated Galaxy Masses: NGC 672 Group

Galaxy	H I Mass ($\times 10^9 M_\odot$)
NGC 672	3.75 ± 0.58
AGC111945	0.04 ± 0.007
AGC111946	0.007 ± 0.002
AGC112521	0.009 ± 0.003
AGC110482	0.01 ± 0.003
NGC 784	0.33 ± 0.05
UGC 1281	0.27 ± 0.04

masses are listed in Table 29 and spectra are shown in Figure 48. No foreground or background galaxies are observed in the direction of the NGC 672 group.

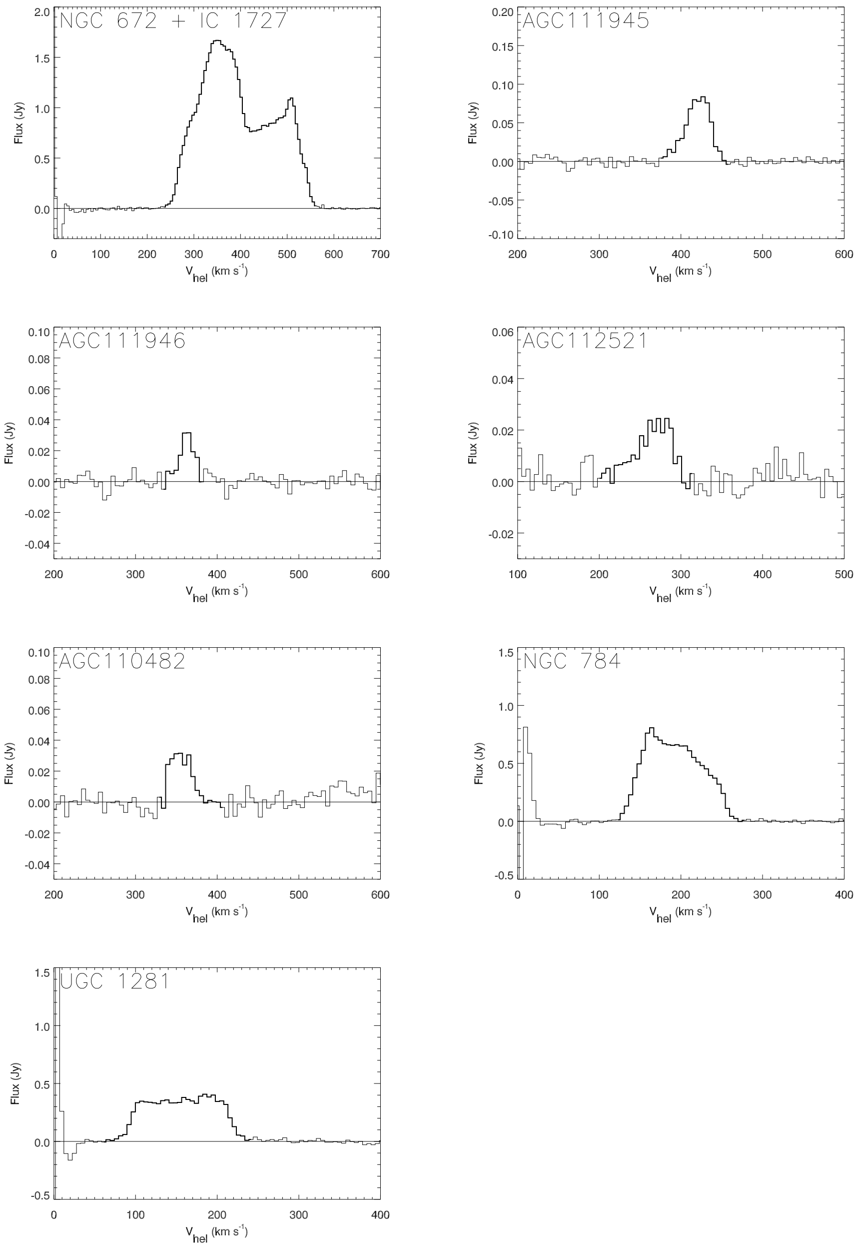

Figure 48: H I intensity profiles of major NGC 672 Group galaxies, used to calculate H I mass.

CHAPTER VII

COMPARISON WITH NUMERICAL SIMULATIONS

In order to determine the origin of the H I clouds we have observed, we must compare their properties to clouds generated in simulations. No existing simulations include all possible H I cloud originating mechanisms. Therefore, we compare our observations to simulations of individual originating mechanisms. For the M81 Group, we compare to the simulation of Yun (1999), which models the interaction of M81, M82, and NGC 3077 using only gravitational force. For the NGC 2403 group, we compare to the Via Lactea II dark matter simulation of a single galaxy halo[1] (Diemand et al., 2008). For the M81 Filament, we compare to a cosmological dark matter only simulation by Holley-Bockelmann (2010).

7.1 M81 Group

A useful insight on whether the newly discovered H I clouds are part of the system of tidal debris produced by the recent collisions involving M81, M82, and NGC 3077 can be obtained by comparing their observed locations and kinematics with the results of a numerical simulation of the tidal interactions in this group. Such a comparison can be made with the simulation of Yun (1999).

The simulation by Yun (1999) is primarily an illustrative model in that only the

---

[1] http://www.ucolick.org/∼diemand/vl/

velocity field of tidal debris is mapped using a limited three-body calculation, rather than employing a full N-body calculation. On the other hand, this approach has been shown to be effective in tracing the location and kinematics of tidally disrupted H I disks as the H I emitting clouds originate from a dynamically cold structure (Toomre & Toomre, 1972). This simulation suggests that nearly all of the observed H I features in the M81 group are consistent with being part of the tidally driven structures resulting from the collisions involving all three galaxies during the last 200-300 Myrs – see Yun (1999) for more detailed discussions. A comparison of the cloud locations with the simulation is shown in Figure 49. Specifically, the locations of the Clouds 1, 2, 4, and 5 are coincident with the locations of tidally disrupted material from the individual disks. While a chance coincidence cannot be ruled out, this comparison suggests that the origin of these H I clouds are tidally disrupted disk material, rather than a kinematically distinct satellite in the group. A more sophisticated, self-consistent future numerical simulation will offer an improved understanding on the nature of these H I clouds.

7.2 NGC 2403 Group

The NGC 2403 Group is not interacting (see Section 3.4), so no HVCs generated by galaxy interactions are expected. However, the clouds may represent cold accretion or dark matter halos with associated H I gas. There are no simulations of the cold accretion process with sufficient resolution for comparison to our observations, but the dark-matter only Via Lactea II simulation by Diemand et al. (2008) is well-suited

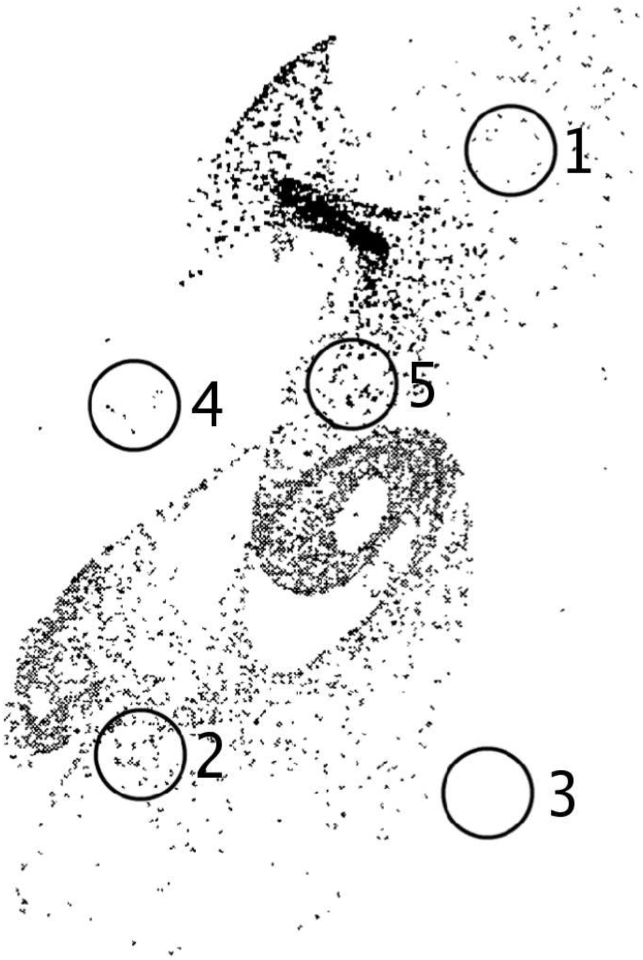

Figure 49: Comparison with the simulation of Yun (1999). Locations of new clouds in the M81 group are circled and numbered.

to comparison with these observations.

Cosmological galaxy formation models predict a population of dark halos; clumps of dark matter and gas that have not yet formed stars. These dark halos have not been observed, but Kravtsov et al. (2004) point out that some of the missing dark halos may be the population of compact HVCs identified by Braun & Burton (1999) (see Chapter 1 for more details on dark matter halos).

The existence of any HVCs associated with dark halos remains in doubt and our observations are designed to place strong limits on the existence of this class of object. The H I clouds we detect in the direction of the NGC 2403 group are likely to be associated with the Milky Way HVC Complex A. However, we cannot definitively rule out the clouds as dark matter halos with associated H I gas, since those halos may be separated by as much as 300 km s^{-1} from the associated galaxy. In the case that the clouds are located in the vicinity of NGC 2403, we can determine how many of these halos our observations should have been able to detect and compare their properties to those expected for dark matter halos with associated H I gas.

The public release of the Via Lactea II simulation consists of a table of resolved sub-halos, with the total masses and 3 dimensional positions and velocities. In order to connect the numerical simulations with the observed H I mass limits, we require an estimate of the H I mass to dark matter mass ratio. The distribution of H I gas compared to the dark matter halo distribution is very uncertain. For the purpose of comparing our observations with the H I clouds, we assume that H I gas follows the dark matter distribution. We take as the scaling factor from dark matter to H

I gas mass the Zwaan et al. (2003) results, summarized in Fukugita & Peebles (2004). Their values yield a H I to dark matter mass ratio of 0.18 ± 0.03 %. We include in our calculation the prescription of Gnedin (2000), which includes a mass cutoff such that a dark matter halo with mass less than 2×10^8 $M_\odot$ has no associated H I gas.

We assume this H I to dark matter ratio, and compute the number of clouds that could be detected. We have taken the Via Lactea II simulation and applied our observing selection criteria of mass limits, angular region surveyed and velocity ranges searched, and computed the number of dark matter halos we would detect, if each halo has 0.18% of its mass in H I .

We placed the simulated components at the distance of NGC 2403 and at the same relative location as is shown in Figure 28. After applying all observing constraints, we counted the number of objects in the field. The simulation was performed with the Via Lactea II model oriented in 4 different configurations: The first configuration placed the simulation components at Z=3300 kpc, the distance of NGC 2403, with velocity 131 km s^{-1}. The other three cases simply flipped the positions about the principle axes. In each configuration there were between 1 and 3 dark matter halos that we should have detected in H I . This is consistent with the number of H I clouds we detect in the direction of the NGC 2403 Group. However, comparison of the phase space (positions and velocities) of simulated and observed components is necessary in order to determine whether they represent the same phenomenon.

We compare the positions and velocities of the detected clouds with the dark matter halos identified in the Via Lactea simulation. To make the comparison we used a 2-dimensional Kolmogorov-Smirnov (KS) test, which gives the probability that two sets of data are part of the same distribution. A 2-dimensional phase-space diagram comparing cloud properties with dark matter halos is shown in Figure 50. It is clear from the figure that the H I clouds are unlikely to be associated with dark matter halos, since they are much more concentrated around the central galaxy in both position and velocity than the dark matter halos. The results of the 2-dimensional KS-test bear this out, giving only a 4% probability that the positions and velocities are part of the same phase-space distribution. Therefore, we conclude that if these clouds are a part of the NGC 2403 group and not foreground Milky Way HVCs, they are not likely to be tracers of dark matter halos. However, due to the position and velocity overlap with the Milky Way HVC Complex A, it is likely that the clouds are foreground Milky Way objects. The Via Lactea II simulation, combined with an assumption for the H I content of dark-matter halos, is not an accurate model for the distribution of mass surrounding the NGC 2403 Group.

7.3 M81 Filament

For the large area observed for the M81 Filament, a single-halo simulation like Via Lactea is not sufficient. In order to determine whether the H I clouds in the M81 filament have the properties expected for gas-embedded dark matter halos, we have compared their properties statistically with the properties of dark matter halos generated by a large cosmological N-body simulation. Analysis includes all clouds detected in M81 Filament within the 8° × 8° region centered on M81. We only include

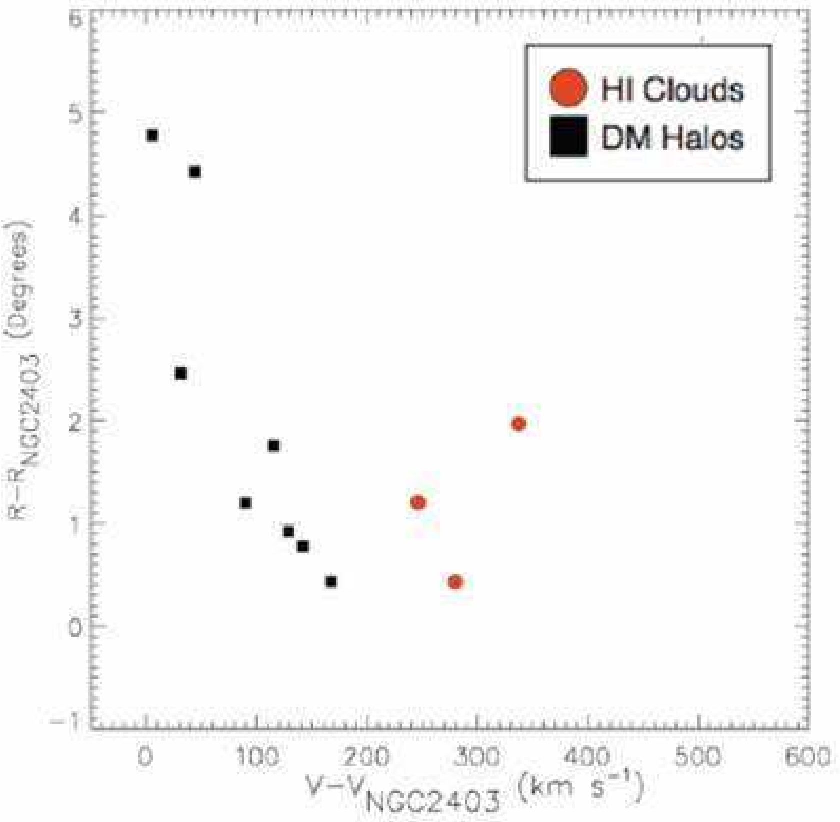

Figure 50: Comparison of positions and velocites of H I clouds NGC 2403 Group with the expected properties of dark matter halos in the Via Lactea simulation with a 0.18% H I /total mass fraction. Note that the H I clouds appear to be a distinct population from the dark matter halos, and they are far from NGC 2403 in position and velocity.

the H I clouds located in this region due to the greater rms noise and contamination by Complex A in other regions of the map. Therefore this analysis excludes clouds 6,7,8, and 13.

We conducted a dark matter only cosmological N-body simulation of a 50^3 Mpc^3 volume of the universe from redshift 149 to redshift zero using 256^3 particles and WMAP5 initial conditions. At redshift zero, we selected a volume 10 Mpc on a side to resimulate with 512^3 particles with a 'zoom' technique aimed to preserve the tidal field outside the higher resolution volume. This smaller volume was selected to host a $\sim 10^{12} M_\odot$ halo at redshift zero – this halo is consistent with the M81 galaxy. We used a friends-of-friends algorithm with a linking length of $b = 0.2$ to identify dark matter halos, and used a SUBFIND technique to determine the bound subhalos.

We again assume a H I to dark matter mass fraction of 0.18%. We then take the numerical simulation prescription described in the previous section and apply it to the 8° × 8° region centered on M81. Our simulation generated a total of 29 clouds with sufficient mass to be detected in our observations. Figure 51 shows a z=0 snapshot of the simulation. Figure 52 shows the histogram of velocities of the components in the simulation. The comparison of the simulated cloud distribution and the observed distribution is striking. There are more clouds predicted in the simulation than are detected in the observations.

We compare the positions and velocities of the detected clouds with the dark matter halos identified in the simulation, using a 2-dimensional Kolmogorov-Smirnov (KS) test. A 2-dimensional phase-space diagram comparing cloud properties with dark matter halos is shown in Figure 52. It is clear from the figure that the H I clouds in our observations are unlikely to be associated with dark matter halos, since they are much more concentrated around the central galaxy in both position and velocity than the dark matter halos found in our simulation. The results of the 2-dimensional KS-test bear this out, giving a 5.7% probability that the position-velocity distributions are alike. Therefore, we conclude that these clouds are not likely to be tracers of dark matter halos. Of the 13 clouds detected in the observed region, 8 are likely to be part of the Milky Way. The remaining 5 H I clouds are most likely generated through some combination of galaxy interactions and cold accretion. In order to determine which of these mechanisms is dominant, further simulations are needed. We have carried out N-body simulations of galaxy groups in order to determine the effect of galaxy interactions; these simulations are described in Chapter 8.

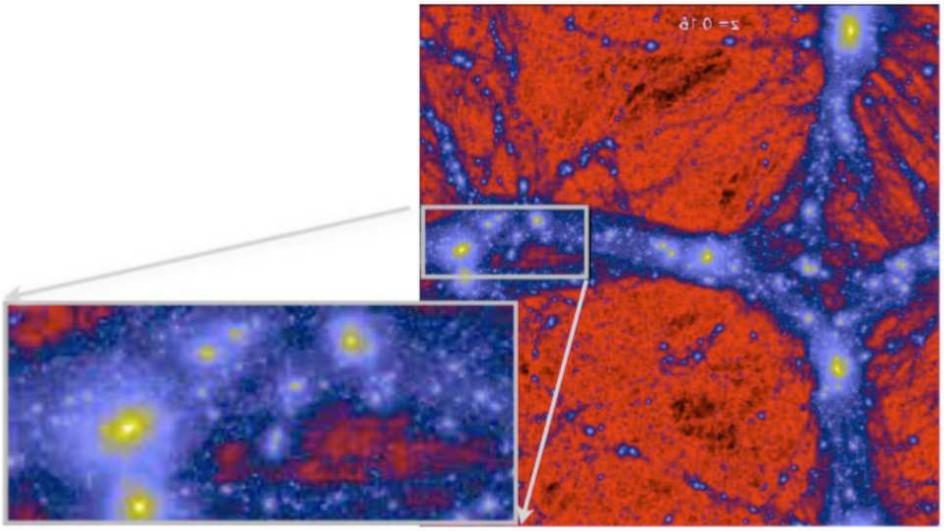

Figure 51: Snapshot of the projected density of dark matter in the cosmological simulation used to find expected properties of halos. The large box is 10 Mpc on a side. The highlighted box corresponds to the angular size of our observations.

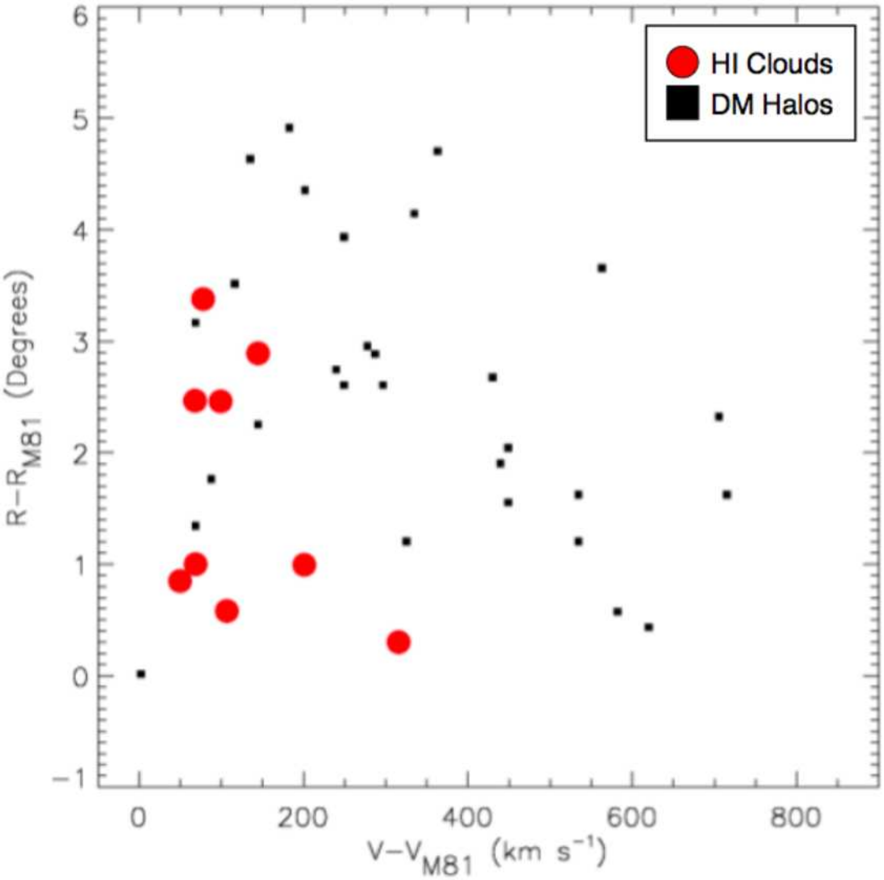

Figure 52: Comparison of positions and velocites of H I clouds in the 8° × 8° region centered on M81 with the expected properties of dark matter halos with a 0.18% H I /total mass fraction. Note that the H I clouds are much more clustered in position and velocity than dark matter halos.

CHAPTER VIII

N-BODY GALAXY GROUP SIMULATIONS

In order to determine whether the H I clouds we observe are generated through interactions between galaxies, it is useful to compare their properties to N-body simulations of galaxy interactions. In a pure N-body simulation of an isolated group of interacting galaxies, any "clouds" that appear must have been generated by those interactions. The full 6-dimensional phase space (position and velocity) properties of those clouds are simple to obtain and compare against observations.

An N-body simulation uses many massive particles to represent the potential of the system of interest – be it a solar system or globular cluster or a slice of the cosmos. The simulation is advanced through time by allowing gravity to act on these particles. N-body simulations of galaxy interactions have mostly involved either mergers between two galaxies (e.g. Toomre & Toomre (1972); Barnes & Hernquist (1992); Mihos & Hernquist (1996); Naab et al. (1999); Lotz et al. (2008); Cox & Loeb (2008)) or much larger-scale, lower-resolution simulations of galaxy harassment in clusters (Rudick et al., 2009), neither of which replicate the dynamics of a galaxy group. Therefore, we have carried out simulations of interactions in galaxy groups for this study.

Ideally, these numerical simulations would self-consistently incorporate all the physical processes and gas physics involved with galaxy interactions, such as atomic and molecular line cooling, star formation, AGN feedback, turbulent viscosity, radiative transfer, and dust opacity. However, current hydrodynamic N-body simulations treat gas physics in a heuristic way with simple, semi-analytic prescriptions to model all the processes that happen on a scale below the resolution element of a simulation; this "subgrid physics" is not physically motivated, but is tuned to match observations. Hydrodynamic simulations are very time-consuming, simply because each time-step must not only solve Poisson's equations, but several hydrodynamic equations as well. As a first step it is useful to carry out pure N-body simulations with the assumption that the H I gas will follow the baryonic collisionless mass, and that gravity is the dominant force in the evolution of large-scale tidal debris (Mihos, 2004). Therefore, we have run a suite of N-body simulations in order to quantify the properties of clouds generated through galaxy interactions.

The simulations encompass a group of four galaxies that are rough analogs in size and mass to the major M81 group galaxies (M81, M82, NGC 3077, and NGC 2976). The galaxy initialization is described in Section 8.1. In total, six simulations are performed with different orbital parameters, chosen to vary the strength of galaxy interactions. The selection of orbital parameters is described in Section 8.2. The N-body code is described in Section 8.3. Analysis of simulations is described in Section 8.4.

Simulations were run using the Advanced Computing Center for Research Education (ACCRE) at Vanderbilt University[1].

---

[1] http://www.accre.vanderbilt.edu/

8.1 Initial Conditions

The simulated galaxy group was constructed to be a close analog to the M81 Group, where H I clouds are observed. The masses and sizes of the galaxy models are initialized to approximate the H I properties of the galaxies observed in Chynoweth et al. (2008). Each galaxy is hosted by a dark matter halo with an NFW density profile truncated at the virial radius. Each galaxy consists of an exponential disk, and all but the analog for NGC 2976 has a bulge with a spherical Hernquist density profile. The properties of the simulated galaxies are listed in Table 30.

N-body realizations of each galaxy were generated using the `buildgal` code, described in Hernquist (1993). In `buildgal`, the particle positions are realized by drawing particles from a density distribution function for each component of the galaxy (dark matter halo, disk, and bulge). The velocities are calculated using the low-order moments of the collisionless Boltzmann equation (Binney & Tremaine, 1987), which describes the motion of massive particles that interact only via the Newtonian gravitational potential:

$$\frac{\partial f}{\partial t} + \mathbf{v} \cdot \frac{\partial f}{\partial \mathbf{r}} - \Delta\Phi \cdot \frac{\partial f}{\partial \mathbf{v}} = 0, \tag{11}$$

where f is the 6-dimensional phase space distribution function of particle positions and velocities ($f(\mathbf{r}, \mathbf{v}, t)$), and Φ is the potential.

The density functions are as follows:

Dark matter halo (Navarro et al., 1996):

$$\frac{\rho_{halo}(r)}{\rho_{crit}} = \frac{\delta_c}{(r/r_s)(1+r/r_s)^2}, \tag{12}$$

where r_s is the scale radius, ρ_{crit} is the critical density, δ_c is the characteristic overdensity, and c is the halo concentration. These variables are described by:

$$r_s = r_{200}/c, \tag{13}$$

where r_{200} is the virial radius, defined as the radius within which the average density is 200 times the critical density of the universe,

$$\rho_{crit} = 3H^2/8\pi G, \tag{14}$$

where H is the Hubble constant and G is the gravitational constant,

$$\delta_c = \frac{200}{3}\frac{c^3}{[ln(1+c) - c(1+c)]}. \tag{15}$$

Since the NFW density profile in this form yields an infinite halo mass, we truncate the dark matter halo at the virial radius.

Disk:

$$\rho_{disk}(R,z) = \frac{M_d}{4\pi h^2 z_0} exp(-R/h) sech^2\left(\frac{z}{z_0}\right), \tag{16}$$

where M_d is the disk mass, h is the radial scale length, and z_0 is the vertical scale thickness (Hernquist, 1993).

Bulge:

$$\rho_{bulge}(r) = \frac{M_b}{2\pi}\frac{a}{r}\frac{1}{(r+a)^3}, \tag{17}$$

where M_b is the bulge mass and a is the scale length (Hernquist, 1990).

8.2 Orbital Parameters

After each galaxy was initialized in isolation, they were tested for stability. Figure 53 shows an example galaxy that is stable over the period of the simulation (1 Gyr), with a bound total energy and a virial ratio (2T/W) near unity. Galaxies were then combined into a single galaxy group to simulate. Each galaxy was given a random orientation, and an initial position and velocity corresponding to the orbits described in Table 31. The M81 analog galaxy was set to be the center of the simulation, at a position and velocity of zero. The other three galaxies' trajectories were defined relative to the M81 analog. In order to explore galaxy interactions with varying levels of intensity, we ran six simulations. Three orbital parameters were varied: First, the trajectory of the M82 analog towards the M81 analog, which was set to either a plunging or an elliptical orbit with eccentricity $e = 0.8$. Secondly, the orbits of the satellite galaxies (NGC 3077 and NGC 2976) around M81 and M82 respectively were set to either be initially circular or elliptical with $e = 0.8$. We chose elliptical orbits to match simulations of infalling satellites (Wetzel, 2010).

Finally, we set the closest approach (orbital pericenter, r_p in the table below) to be zero, for a head-on collision, or 15 kpc for a grazing collision. After the simulation was completed, each snapshot was smoothed to the angular resolution of the GBT

Table 30: Model Galaxy Parameters

Galaxy	Dark Matter Halo				Disk					Bulge			
	Mass ($\times 10^{10}$ $M_{\odot}$)	R (kpc)	c	N	Mass	R (kpc)	Max z (kpc)	h	N	Mass	R (kpc)	a (kpc)	N
M81	600	370	10	75×10^4	20	15	2	0.2	10×10^4	4	2	0.2	2×10^4
M82	80	190	15	10×10^4	4	6.7	2	0.2	2×10^4	0.8	2	0.117	4×10^3
NGC 3077	40	150	15	5×10^4	2	4.7	2	0.2	1×10^4	0.4	0.93	0.093	2×10^3
NGC 2976	4	70	20	5×10^3	0.2	2.5	0.75	0.075	1×10^3	...	...	...	...

Table 31: Parameters of Simulations

Number	M81/M82 eccentricity	r_p (kpc)	Satellite eccentricity
1	1	15	0
2	1	15	0
3	1	0	0.8
4	1	0	0
5	0.8	15	0
6	0.8	15	0.8

at the distance of the M81 group, to facilitate comparison with observations. An example initial snapshot and one snapshot after 800 Myr of evolution are shown in Figure 54.

8.3 N-Body Code

In an N-body simulation, the gravitational force on each particle from every other particle must be calculated, and the motion of each particle must be advanced in time. In principle, the force calculation is of order N^2, where N is the total number of particles in the simulation; the computation time for this calculation becomes prohibitive for simulations with large N (anything above $N = 10^7$). Therefore, we use GADGET2[2], a tree-code, to perform the force calculation. Tree codes simplify the force calculation by grouping far-away particles into one larger mass and calculating the force from that large mass. Using this method reduces the calculation time to order $N ln N$ (Binney & Tremaine, 1987). The integration is performed using

---

[2] http://www.mpa-garching.mpg.de/galform/gadget/index.shtml

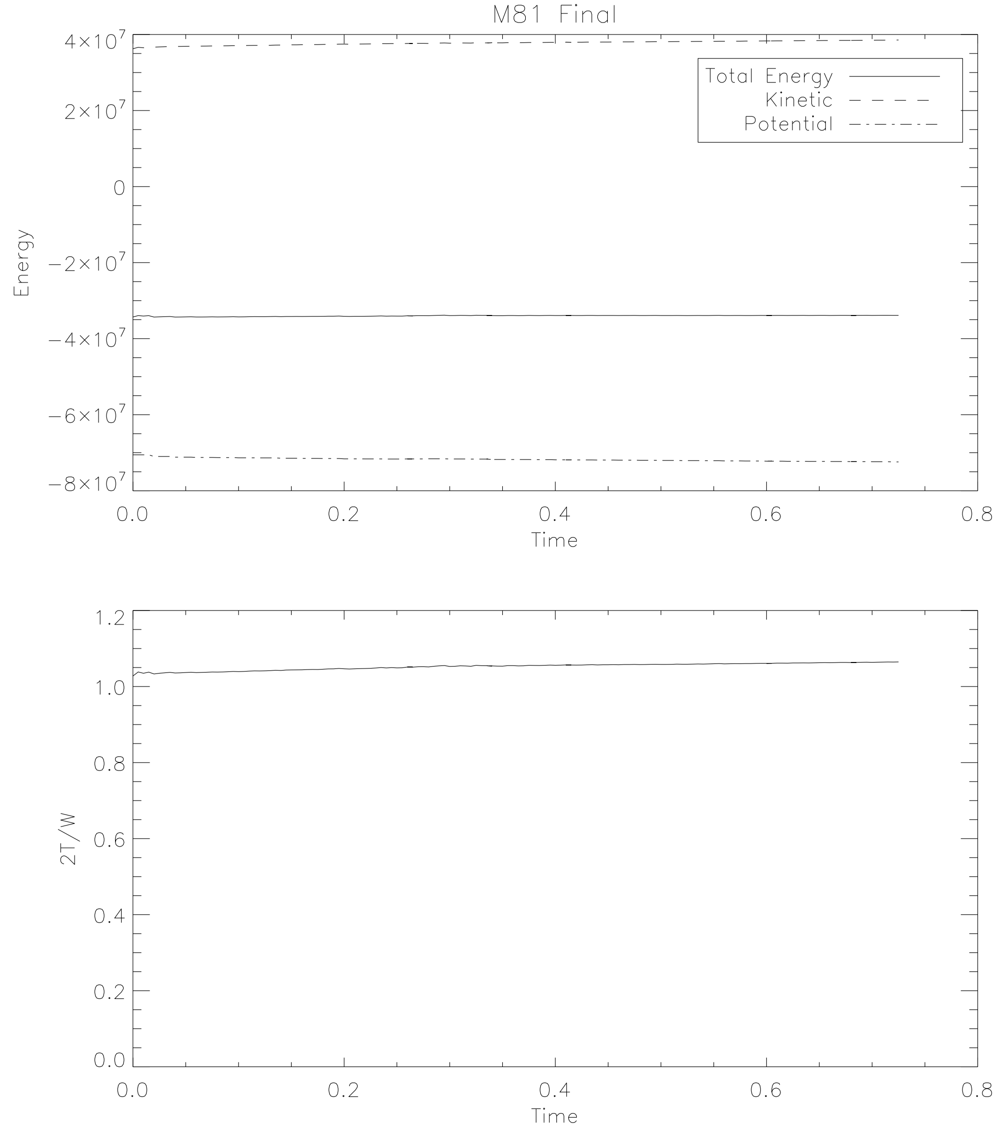

Figure 53: Example energy statistics for the M81 analog galaxy in isolation. Top: Note that the total energy is negative throughout the simulation, indicating that the majority of particles remain bound to the galaxy. Bottom: Note that the virial ratio 2T/W remains near unity for the duration of the simulation.

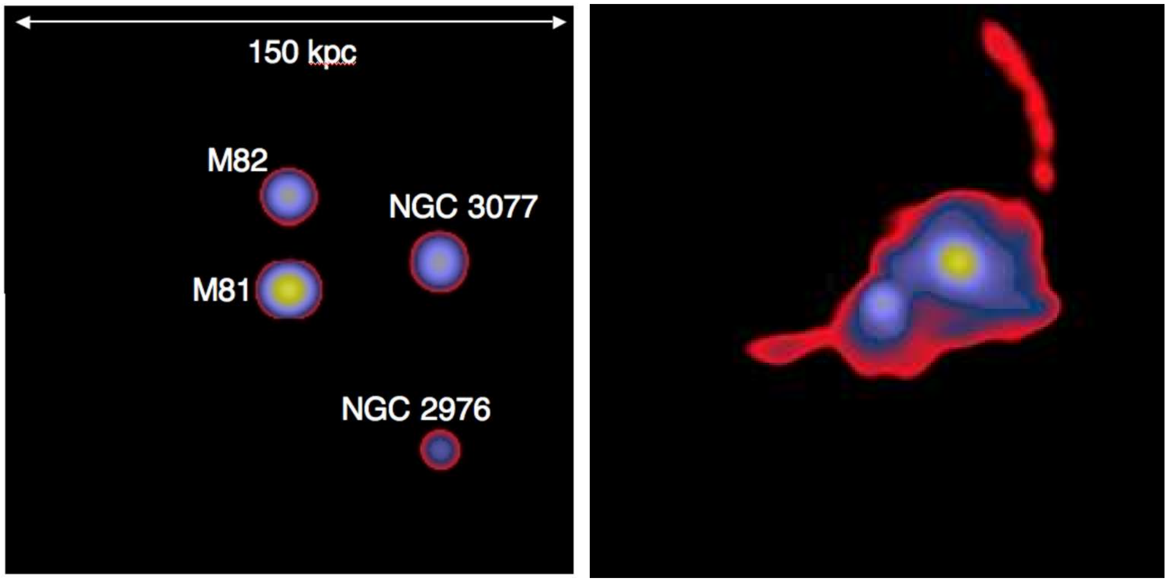

Figure 54: Example simulation snapshots, smoothed to the GBT resolution at the distance of the M81 group (9 kpc). Left: time=0. Right: time=800 Myr. Galaxy analogs are labeled.

a leapfrog integrator to calculate particle positions and velocities. In the leapfrog algorithm, the positions and velocities are calculated at time intervals that are offset by a half timestep, and hence the particle positions and velocities 'leap' over one another (Hut & Makino, 2004). This algorithm can also be expressed using only integer times as:

$$\mathbf{r}_{i+1} = \mathbf{r}_i + \mathbf{v}_i dt + \mathbf{a}_i (dt)^2/2, \tag{18}$$

and

$$\mathbf{v}_{i+1} = \mathbf{v}_i + (\mathbf{a}_i + \mathbf{a}_{i+1}) dt/2, \tag{19}$$

where **r** is the particle position, **v** is the velocity, and **a** is the acceleration calculated from Newton's law of gravitation with softening,

$$\mathbf{F}_i = m_i a_i = -\sum_{j \neq i} \frac{G m_i m_j |\mathbf{r}_{\_}\mathbf{r}_j|}{(|\mathbf{r}_i - \mathbf{r}_j|^2 + \epsilon^2)^{3/2}}, \tag{20}$$

where m is particle mass, G is Newton's universal gravitational constant, and r is particle distance. The gravitational softening parameter, ϵ, prevents a diverging force for close particles. The softening length also represents the minimum spatial resolution of the simulation. For our simulations, the softening lengths are:

$$\epsilon_{\text{Halo}} = 20\text{pc}, \epsilon_{\text{Disk}} = 14\text{pc}, \epsilon_{\text{Bulge}} = 1\text{pc} \tag{21}$$

The simulations are run for a period of 1 Gyr.

8.4 Analysis

We have made first steps towards analyzing these simulations; this section describes what has been done so far and sets out the technique for further analysis. We have run a suite of lower-resolution simulations with a factor of 10 fewer particles than in Table 30 to test our techniques and analysis tools. Future high-resolution simulations will test for convergence and find lower-mass H I cloud analogs.

Simulations will be analyzed throughout the entire interaction to study the formation and evolution timescales for H I clouds. However, most of our statistics will focus on the 200 Myr following the first pericenter passage of M81 and M82, since early simulations (Yun, 1999) and observations (de Mello et al., 2008) suggest that the last major passage occurred 200 Myr ago.

We have constructed analysis codes to detect clouds in the same manner as the GBT observations. Particle positions and velocities are written out as snapshots every 20 Myr. These snapshots are converted into datacubes with the same velocity resolution as the GBT data. The simulations are smoothed to the angular resolution of the GBT at the distance of the M81 group, approximately 9 kpc. The simulated datacubes are then searched by eye for cloud-like structures with coherent velocities. Cloud candidates are followed up by construction of a spectrum, which determines whether the candidate is coherent in velocity space and kinematically distinct from galaxies and tidal streams. So far we have conducted a preliminary search for clouds in one snapshot and plan to search more exhaustively for clouds in the future. Figure 55 shows this snapshot with cloud candidates labeled, along with the spectrum of one cloud. In total, we confirm 6 clouds in the snapshot.

The velocities and positions of clouds relative to the M81 analog galaxy will be tabulated. H I masses are calculated by scaling the peak H I intensity of the M81 analog to the observed peak H I intensity of M81 in the GBT data. Using this method, the calculated H I mass of the M81 analog matches the mass of M81 calculated from observations to within 0.4%. After scaling and smoothing to GBT angular resolution, clouds with an H I mass greater than $\sim 10^5$ $M_\odot$ can be detected. The positions, velocities and masses of the simulated, interaction-generated clouds will be compared against our GBT observations using a 2-dimensional KS test, as described in Chapter 7.

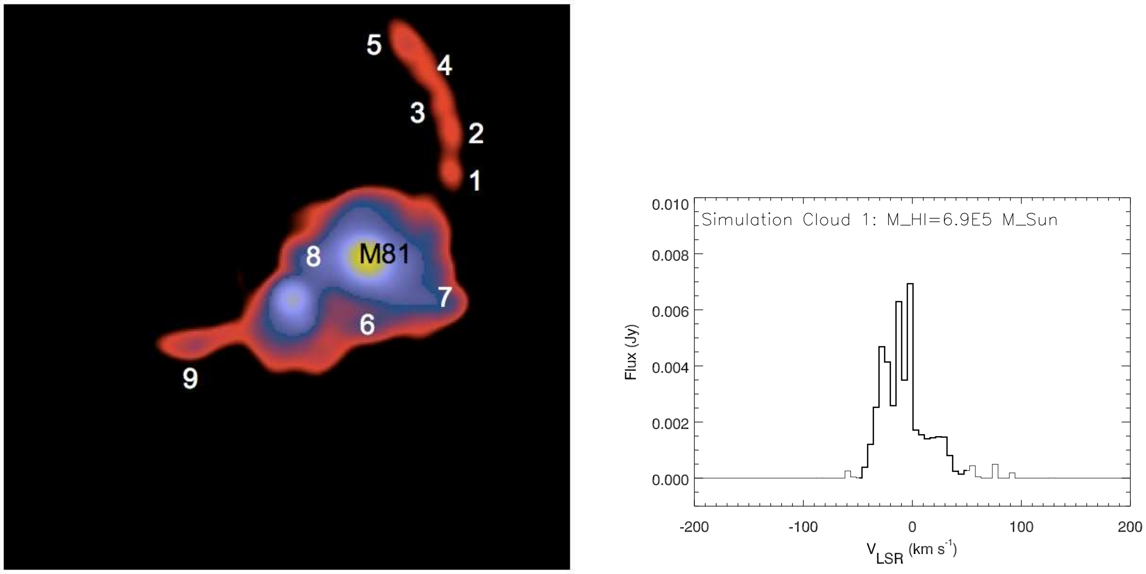

Figure 55: Left: Example simulation snapshot with cloud candidates labeled. Cloud candidates 6,7, and 8 are not coherent in velocity space, and are thus discarded. Right: Example spectrum of cloud candidate 1. Note the distinct velocity structure.

CHAPTER IX

FUTURE WORK

It is not clear whether the clouds we have discovered in the M81 Filament are exact analogs to the local Milky Way HVCs. In fact, they are most likely not precise analogs, since these clouds are associated with a galaxy group instead of an isolated galaxy, and since many of the clouds are much farther away from any galaxy than the clouds around the Milky Way. Further statistical comparison of our clouds with the Milky Way HVC system will better quantify the probability that the H I clouds we have observed are HVC analogs. Follow-up high resolution radio observations, as well as UV and optical wavelength observations will be key pieces to investigating the exact nature of these H I clouds.

9.1 Statistical Comparison to HVCs

Statistical comparisons (such as KS tests) between our observed H I clouds and the Milky Way HVC system are difficult, due to the small numbers of clouds observed. In order to determine whether the observed H I clouds are similar to the Milky Way HVCs, a Monte Carlo-type simulation may be useful. Specifically, we plan to compare the velocity deviations of HVCs and our observed H I clouds from the host galaxy.

In this Monte Carlo simulation, a normalized cumulative distribution function (CDF) is constructed from the known HVC velocity deviations. Then many samples are drawn from the CDF, and the fraction of times that the sample matches the observed H I cloud velocity deviations gives the probability that the samples are alike.

The difficulty with performing such a Monte Carlo simulation is that the CDF for Milky Way HVCs is not well constrained. There are only 4 Milky Way HVC complexes that could be observed at the M81 distance (Complexes H and C, the Smith Cloud, and the Magellanic Stream). Nevertheless, we have written the code to perform this analysis, included in Appendix C. Future work towards this analysis will involve attempting to build a realistic CDF for Milky Way HVC velocities. More sensitive observations would allow the inclusion of lower-mass Milky Way HVCs in the CDF.

9.2 EVLA H I Observations

As discussed in Chapter 1, the Milky Way HVCs have a distinct spatial and kinematic substructure. It would be very useful to compare the substructure of the new H I clouds discovered in this study to the HVCs. All H I clouds detected in this study are unresolved in the 9ʻ beam of the GBT. Therefore, the structure of the clouds is unknown. In order to determine the detailed spatial and kinematic structure of the clouds, interferometric observations are necessary. With current interferometers such as the Very Large Array (VLA) and Westerbork, observations of faint extragalactic H I clouds are difficult. This is due to both the long integration times necessary and the lack of adequate velocity coverage and resolution.

The Expanded Very Large Array (EVLA) will be beginning operations in 2010. The EVLA will be more sensitive at L-band than the VLA; a factor of about 5 improvement in sensitivity is predicted. In addition, the EVLA correlator has a much wider bandwidth and higher spectral resolution. A survey of interferometric follow-up observations of H I clouds is feasible with the EVLA.

9.3 UV and Optical Observations

One remaining question is whether the clouds we discovered are in fact starless, as the HVCs are. The observations of de Mello et al. (2008) cause questions to arise concerning the nature of our H I clouds. Recently a number of "blue blobs" of young stars have been observed near the M81 group in the UV and in Hα by de Mello et al. (2008); these stars may be related to the H I clouds we have observed. Alternatively, the H I clouds may in fact be dwarf galaxies or may contain stars that were ripped from the M81 or M82 disk during the last major passage. If the clouds do contain stars, this lends credence to the theory that they are produced by the ongoing interactions in the M81 group – in that case, though, the H I clouds cannot be considered HVC analogs and therefore the observations shed no light on the HVC mystery. Follow-up observations of the H I clouds in the UV regime, Hα, and [O III] (for planetary nebulae) would determine whether the clouds contain or are forming stars.

9.4 Simulations

It will be very useful to compare both our N-body simulations and observations to recent work that simulates the M81/M82 merger with gas physics included. Simulations have been done by Joung et al. (2010) using Enzo[1], an adaptive mesh refinement (AMR) hydrodynamics code. They first ran a low resolution model with a side length of 64 Mpc h^{-1} (comoving) to identify a halo with a virial mass of $\sim 1.5 \times 10^{12}$ $M_\odot$ that undergoes a recent close encounter with a less massive galaxy. They looked for a system with the relevant parameters (mass ratio, distance at closest approach, time since closest approach, etc.) matching those in Sofue (1998). Then they ran a higher resolution, zoom-in simulation, focusing on the halo selected to represent the M81/M82 system. For the intermediate resolution model, particle masses are $m_{DM} = 2.8\times 10^6$ $M_\odot$, $m_{star} = 1.0\times 10^5$ $M_\odot$, and minimum cell size = 350 pc. For the high resolution model, the mass resolutions were unchanged but the minimum cell size was set to 44 pc. Radiative cooling of gas, star formation, stellar feedback, metagalactic UV background, and self-shielding of the UV background were included in a self-consistent way.

In Figure 56 are 2 different projections of H I column densities in the high spatial resolution model. In those images, the field of view is approximately (700 kpc)^2.

---

[1] http://lca.ucsd.edu/projects/enzo

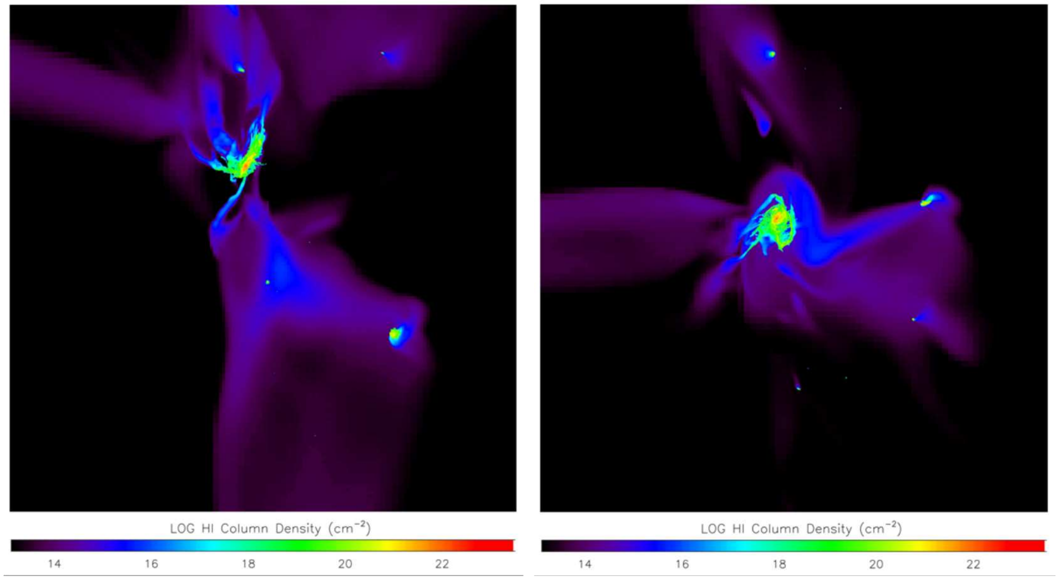

Figure 56: Two H I column density projections of the M81 Group simulation of Joung et al. (2010). Field of view is approximately (700 kpc)^2.

CHAPTER X

SUMMARY AND CONCLUSIONS

This dissertation addressed the origin of the neutral hydrogen clouds observed around the Milky Way and other nearby galaxies. In particular, we investigated the role of galaxy-galaxy interactions, gas-embedded dark matter halos, and cold accretion as originating mechanisms for clouds with H I masses greater than $\sim 10^6$ $M_\odot$. We have detected several new H I clouds in nearby galaxy groups. We find the role of each mechanism to be as follows:

1. H I **embedded dark-matter halos:** The observed $M_{HI} \geq 10^6$ $M_\odot$ H I cloud population does not match the predictions of ΛCDM cosmological models.
2. **Cold accretion:** The observed H I clouds are not likely to be a product of cold accretion. If H I clouds tracing cold accretion exist in our observed position, velocity, and mass regimes, as simulations predict, they should have been observed in all groups.
3. **Galaxy interactions:** Our results indicate that the majority of $M_{HI} \geq 10^6$ $M_\odot$ extragalactic H I clouds are generated through tidal stripping caused by galaxy interactions.

By analogy, the Milky Way HVC population is likely generated through a combination of tidal stripping and galactic fountains.

We have observed 5 nearby galaxy groups in H I with the GBT in an effort to search for H I clouds that are analogous to the Milky Way HVCs. Such clouds are likely created through a combination of galactic fountains, galaxy interactions, dark matter substructure, and cold accretion. The observed groups have varying levels of galaxy interactions, which we quantify using interaction potential and interaction evidence indices. Our survey allows us to detect all clouds in velocity space, all clouds within 50 kpc of group galaxies, and 8% to 29% clouds in mass space. We find 13 clouds in the direction of the M81 Filament, which includes the M81 and NGC 2403 galaxy groups. These clouds have properties similar to clouds detected around the Milky Way and nearby galaxies. Five of these clouds are likely to be associated with the Milky Way HVC Complex A, rather than extragalactic.

We also observed the M81 Filament in order to search for evidence of the H I cosmic web at the limits of current observational capability. We detected no diffuse H I associated with the M81 Filament. This is most likely due either to confusion with foreground Milky Way H I gas or inadequate column density sensitivity. Future radio instrumentation such as the EVLA may be able to detect the H I cosmic web.

We find two H I clouds in the direction of the Canes I galaxy group, near the galaxy KUG 1218+387. These clouds may be HVCs associated with KUG 1218+387, or companion galaxies to KUG 1218+387.

The properties of the H I clouds associated with the M81 Filament are compared with a cosmological dark matter simulation in order to determine whether the clouds are associated with dark matter halos. We find that the H I clouds are not likely to be associated with dark matter halos, with a 94% probability that the clouds are originated with a different mechanism. Since the clouds are located in the group with the highest interaction evidence index, it is likely that the clouds are a product of galaxy interactions. However, more simulations are needed of the cold accretion and galaxy interactions processes in order to determine the expected properties for H I cloud generated through those processes. We have carried out a suite of N-body simulations of galaxy group interactions, and we have made first steps towards analyzing these simulations.

Future work towards determining the origin of H I clouds in galaxy groups should include high-resolution H I observations with the EVLA to determine their substructure; UV and optical observations to search for a stellar component; and comparison with simulations of the M81 Group that include all the relevant gas physics and allow for cold accretion. These studies would place stronger constraints on the origins of H I clouds in galaxy groups, and determine whether such clouds are analogs to the Milky Way HVCs. Finally, these future observations will place stronger constraints on cosmological models of galaxy formation.

APPENDIX A

THE 21-CENTIMETER NEUTRAL HYDROGEN LINE

This Appendix reviews the relevant aspects of the physics of neutral hydrogen emission. These processes lead to formulae for the H I mass and column density of an emitting region.

The 21 cm transition is a result of the splitting of the ground state of the atom into two states with a very slight energy difference. This hyperfine splitting is caused by the magnetic interaction of the electron and proton spins, which may be either aligned (total angular momentum $F = 1$) or anti-aligned ($F = 0$). The energy of the atom in the $F = 1$ state is higher than the $F = 0$ configuration by $\simeq 6 \times 10^{-6}$ eV, so a transition results in a photon with that energy.

This transition is forbidden, and hence has an extremely small probability. Therefore the half-life is very long ($\simeq$ 11 million years, see below), and transitions are rare. However, H I is so abundant in the ISM that the 21 cm line is easily observable.

The statistical weights of the upper and lower state are 3 and 1 respectively, since F=1 is a triplet state and F=0 a singlet. The populations of the F=1 and F=0 states in thermodynamic equilibrium are described by statistical mechanics, with the Boltzmann factor:

$$\frac{n_1}{n_0} = 3e^{-h\nu/kT_s} \tag{22}$$

Where ν is frequency of the transition and T_s is the spin temperature. Spin temperature is defined by this relation: it is the temperature required for a given population ratio of the states, if the gas is in thermodynamic equilibrium.

In order for thermodynamic equilibrium conditions to exist, the density of the gas must be high enough for collisional excitations and de-excitations to dominate over spontaneous transitions. For the typical density of the ISM, the time between collisions is much less than the radiative half-life, so the spin temperature corresponds to the kinetic temperature of the gas.

The energy of the transition is so small that $h\nu << kT$ always holds; even the cosmic microwave background at 2.7 Kelvin has $kT = 2.3 \times 10^{-4}$ eV, a factor of 100 higher than $h\nu$ for the 21 cm line. Therefore, in thermodynamic equilibrium, the exponential factor in equation (1) can be neglected and $n_1 \simeq 3n_0$. The total density of neutral hydrogen, then, is $N_H = n_0 + n_1 = 4n_0$.

Since the radiation is due to the magnetic dipole moment of the atom, the Einstein A coefficient for the probability of spontaneous transition can be expressed by analogy with the coefficient for an electric dipole (Lang, 1999):

$$A_{10} \simeq \frac{64\pi^4\nu^3}{3hc^3}\mu^2 \tag{23}$$

Where ν_{10} is the frequency of the transition and μ is the magnetic moment for H I in the ground state, called the Bohr magneton. The Bohr magneton is found by

$$\mu = \frac{eh}{4\pi mc} = 0.927 \times 10^{-20}\ erg\, Gauss^{-1} \tag{24}$$

So the probability that the atom will spontaneously undergo this transition is

$$A_{10} \simeq 2.85 \times 10^{-15}\ s^{-1} \tag{25}$$

corresponding to a radiative half-life of $\sim$ 11 million years. In order to find the column density of neutral hydrogen, we assume local thermodynamic equilibrium. We can then find the absorption coefficient (Rybicki & Lightman, 1979):

$$\alpha_\nu = \frac{h\nu}{4\pi} n_0 B_{01} \left[1 - e^{-h\nu/kT}\right] \phi(\nu) \tag{26}$$

Using the Einstein relations

$$A_{10} = \frac{8\pi h\nu^3}{c^3} B_{10} \tag{27}$$

and

$$g_0 B_{01} = g_1 B_{10}, \tag{28}$$

and keeping in mind that we are working in the Rayleigh-Jeans regime where $e^{-h\nu/kT_s} \simeq 1 - h\nu/kT_s$, this simplifies to

$$\alpha_\nu \simeq \frac{3c^2}{32\pi} \frac{A_{10} N_H I}{\nu} \frac{h}{kT_s} \phi(\nu) \tag{29}$$

Where $\phi(\nu)$ is the line profile function. Since the broadening of the line is determined by the variations in radial velocity of the particles, the line profile is really a function of velocity. This function must be normalized when integrated over velocity; therefore, when we integrate over velocity $\phi(\nu)$ goes to unity. When we integrate over the line of sight to the object, we obtain the column density of neutral hydrogen in terms of the optical depth:

$$\left(\frac{N_{HI}}{cm^{-2}}\right) = 1.82 \times 10^{18} \int \left(\frac{T_s}{K}\right) \tau(v) d\left(\frac{v}{kms^{-1}}\right) \tag{30}$$

Provided that the gas observed is optically thin (a safe assumption for observations of H I clouds), we can use the relation $T_s\tau \simeq T_B$ where T_B is the brightness temperature (the quantity directly measured by a telescope). Finally, we have

$$\left(\frac{N_{HI}}{cm^{-2}}\right) = 1.82 \times 10^{18} \int \left(\frac{T_B}{K}\right) d\left(\frac{v}{kms^{-1}}\right) \tag{31}$$

The brightness temperature of neutral hydrogen can be used to calculate the HI mass of the observed object in the optically thin case. Mass is an especially important quantity for observations of H I clouds. Mass is found by integrating the column density over the surface area of the system (Binney & Merrifield, 1998):

$$\frac{M_{HI}}{M_{\odot}} = 2.36 \times 10^{5} \left(\frac{D}{Mpc}\right)^{2} \frac{\int S(v)dv}{Jy\ kms^{-1}} \tag{32}$$

Where $S(v)$ is the flux measured in Janksys, where 1 Jy = 10^{-23} erg s^{-1} cm^{-2} Hz^{-1}. The conversion from brightness temperature in K to flux in Jy is determined by parameters of the telescope used.

APPENDIX B

N-BODY TOOLS

Galaxy Initialization

Galaxies are realized in N-body form using the `buildgal.f` code, via the methods described in Hernquist (1993) and Chapter 8. Below is a sample `buildgal.f` input file, with the relevant parameters for producing an M81 analog galaxy.

Sample buildgal.f infile

```
20.0   disk mass
123 random number seed
y output softening length?
2000000     # of disk pcles
0.2 scale height
2.428571429 solar radius
1.5 Q-solar
0.005 softening length for disk pcles
2.0 zmax
15.0 rmax
n include gas?
y include a bulge?
4.0 bulge mass
0.2 bulge scale-length
y bulge self-grav?
400000 number of bulge particles
2.0 max radius for bulge pcles
0.0005 softening for bulge
n non-spherical bulge?
y include a halo?
y include halo self-gravity?
370.0 maximum radius of halo
15000000   # of halo pcles
0.015 softening length for halo pcles
NF halo type
600.0 halo mass
```

```
10.0 halo concentration
200 virial overdensity
n include a satellite?
n add two models?
```

GADGET2

The output of `buildgal.f` is a file with the 3-dimensional position, 3-dimensional velocity, and mass of each particle. The GADGET2 code requires an input file called a 'snapshot', with a format as described in the GADGET2 users' guide at `http://www.mpa-garching.mpg.de/gadget/users-guide.pdf`. The GADGET2 code requires a parameter file to run each simulation. An example parameter file is below. Lines preceded with '%' are comment lines.

Sample GADGET2 .param file

```
%  Relevant files

InitCondFile      4gal_final.1.dat
OutputDir          /home/chynowkm/final_1/

EnergyFile         energy_final_1.txt
InfoFile           info_final_1.txt
TimingsFile        timings_final_1.txt
CpuFile            cpu_final_1.txt

RestartFile        restart
SnapshotFileBase   snapshot_final1

OutputListFilename output_list.txt

% CPU time -limit

TimeLimitCPU      2629750  % = 96 hours
ResubmitOn        0
ResubmitCommand   my-scriptfile

% Code options
```

```
ICFormat                 1
SnapFormat               1
ComovingIntegrationOn    0

TypeOfTimestepCriterion  0
OutputListOn             0
PeriodicBoundariesOn     0

%  Characteristics of run

TimeBegin           0.0        % Begin of the simulation
TimeMax             1.0        % End of the simulation

Omega0               0
OmegaLambda           0
OmegaBaryon           0
HubbleParam         1.0
BoxSize               0

% Output frequency

TimeBetSnapshot        0.02
TimeOfFirstSnapshot    0

CpuTimeBetRestartFile     36000  % = 10 hours in seconds
TimeBetStatistics         0.005

NumFilesPerSnapshot       1
NumFilesWrittenInParallel 1

% Accuracy of time integration

ErrTolIntAccuracy      0.025

CourantFac             0.15

MaxSizeTimestep       0.001
MinSizeTimestep       0.0

% Tree algorithm, force accuracy, domain update frequency

ErrTolTheta            0.5
TypeOfOpeningCriterion 1
```

```
ErrTolForceAcc         0.005

TreeDomainUpdateFrequency    0.1

%  Further parameters of SPH

DesNumNgb              50
MaxNumNgbDeviation     2
ArtBulkViscConst       0.8
InitGasTemp            0          % always ignored if set to 0
MinGasTemp             0

% Memory allocation

PartAllocFactor       2.0
TreeAllocFactor       0.8
BufferSize            25          % in MByte

% System of units

UnitLength_in_cm         3.085678e21        ;  1.0 kpc
UnitMass_in_g            1.989e43           ;  1.0e10 solar masses
UnitVelocity_in_cm_per_s 1e5                ;  1 km/sec
GravityConstantInternal  0

% Softening lengths

MinGasHsmlFractional 0.25

SofteningGas       0
SofteningHalo      0.015
SofteningDisk      0.005
SofteningBulge     0.0005
SofteningStars     0
SofteningBndry     0

SofteningGasMaxPhys       0
SofteningHaloMaxPhys      0.015
SofteningDiskMaxPhys      0.005
SofteningBulgeMaxPhys     0.0005
SofteningStarsMaxPhys     0
SofteningBndryMaxPhys     0
```

```
MaxRMSDisplacementFac 0.2
```

Sample PBS job script

Below is an example script used to run an N-body simulation using GADGET2 on the ACCRE super-computing cluster at Vanderbilt University.

```
#!/bin/tcsh
#PBS  -M katie.m.chynoweth@vanderbilt.edu
#PBS -m bae
#PBS -l nodes=64:ppn=2:x86
#PBS -l pmem=2000mb
#PBS -l mem=256000mb
#PBS -l walltime=100:00:00
#PBS -o out_final1.test.9
#PBS -j oe

echo $PBS_NODEFILE
cd $PBS_O_WORKDIR

#mpirun -v -np 64 Gadget2 test_2.param 2
/usr/local/mpiexec/latest/opteron/gcc42/nonet/bin/mpiexec
-n 128 P-Gadget2-alloc 4gal_final.1.param 1


# - end of script
```

APPENDIX C

STATISTICAL ANALYSIS

This Appendix includes the FORTRAN code that performs a Monte Carlo statistical comparison of the Milky Way HVC velocity deviations and the observed H I cloud velocity deviations. The code takes as input a file named `mwhvcdv.dat`, which has two columns of data representing the Milky Way HVCs: Column 1 should list a velocity deviation, and column 2 the number of clouds with that velocity deviation. The observed H I cloud velocity deviations are hard-coded as data1, data2, etc. The output of the code is the number of draws taken from the CDF (also hard-coded) and the number of times the draws matched the observed H I cloud velocity deviations.

```
      program twopoint
C
C     find density.
C
      parameter(n1=24,n2=300, n3=2000)
      integer i,j,k,countv,iseed,totnum
      real*8 vbin,probvbin1,probvbin2,testv1,testv2,
     &     totprob,deltav(n1),num(n1),vprob(n2),cumulative,
     &     mcdeltav1(n3),mcdeltav2(n3),data1,data2,match1,
     &     match2


      data1=153.
      data2=128.
      iseed=-1238

      do i=1,n2
        vprob(i)=0
```

```
      enddo


      open(11,file='mwhvcdv.dat')
      do i=1,n1
         read(11,*) deltav(i),num(i)
      enddo
      close(11)


      open(99,file='monte.vel.dat')
      open(2,file='veldist.dat')
      cumulative=0
      do i=1,n2
         vbin=float(i+100)
         vprob(i)=0
         do j=1,n1
         if((deltav(j).gt.vbin-1).and.(deltav(j).le.vbin))then
            vprob(i)=num(j)
         else

         endif

         cumulative=cumulative+vprob(i)
         enddo
c               write(*,*) vbin,vprob(i),cumulative

         vprob(i)=cumulative
      enddo
      do i=1,n2
         vbin=float(i+100)
         vprob(i)=vprob(i)/cumulative
               write(2,*) vbin,vprob(i),cumulative
      enddo

      countv=0
      match=0
      do while(countv.lt.n3)
         testv1=0
         testv2=0
         do while((testv1.eq.0))
            probvbin1=ran2(iseed)
            do i=2,n2
```

```
               vbin=float((i-1)+100)
c               write(*,*) 'vbin',vbin,probvbin1,probvbin2,
c     &           vprob(i-1),vprob(i)
               if((probvbin1.gt.vprob(i-1)).and.
     &              (probvbin1.le.vprob(i)))then
                  mcdeltav1(countv+1)=vbin
                  testv1=1.0
               endif
          enddo
          enddo
         do while((testv2.eq.0))
            probvbin2=ran2(iseed)
            do i=2,n2
               vbin=float((i-1)+100)
c               write(*,*) 'vbin',vbin,probvbin1,probvbin2,
c     &           vprob(i-1),vprob(i)
               if((probvbin2.gt.vprob(i-1)).and.
     &              (probvbin2.le.vprob(i)))then
                  mcdeltav2(countv+1)=vbin
                 testv2=1.0
               endif
            enddo

         enddo
         if((mcdeltav1(countv+1).le.data1+5.0).and.
     &       (mcdeltav1(countv+1).ge.data1-5.0)
     &       .and.(mcdeltav2(countv+1).le.data2+5.0).and.
     &            (mcdeltav2(countv+1).ge.data2-5.0))then
            match1=match1+1.0
         endif

         if((mcdeltav2(countv+1).le.data1+5.0).and.
     &      (mcdeltav2(countv+1).ge.data1-5.0)
     &       .and.(mcdeltav1(countv+1).le.data2+5.0).and.
     &            (mcdeltav1(countv+1).ge.data2-5.0))then
            match2=match2+1.0
         endif


         countv=countv+1
         write(99,*) countv,mcdeltav1(countv),mcdeltav2(countv),
     &    match1,match2
         write(*,*) countv,mcdeltav1(countv),mcdeltav2(countv),
```

```
     &     match1, match2

      enddo




c
c      do mhisto=0,2000
c         histo(mhisto)=0.1
c      enddo


c      mhisto=0
c      do massran=0,2000
c         mhisto=mhisto+1
c         do k=1,n3
c            if((vtot(k).lt.massran+1).and.
c     &           (vtot(k).ge.massran))then
c               histo(mhisto)=histo(mhisto)+1.0
c            endif
c         enddo
c      enddo
c      mhisto=0
c      do massran=0,2000
c         mhisto=mhisto+1
c         write(10,*) massran,histo(mhisto)

c      enddo

 999   format(i9,1x,10(1x,e10.4))

       close(99)
       end


        FUNCTION ran2(idum)
        INTEGER idum,IM1,IM2,IMM1,IA1,IA2,IQ1,IQ2,IR1,IR2,NTAB,NDIV
        REAL ran2,AM,EPS,RNMX
        PARAMETER (IM1=2147483563,IM2=2147483399,AM=1./IM1,IMM1=IM1-1,
     *IA1=40014,IA2=40692,IQ1=53668,IQ2=52774,IR1=12211,IR2=3791,
     *NTAB=32,NDIV=1+IMM1/NTAB,EPS=1.2e-7,RNMX=1.-EPS)
      INTEGER idum2,j,k,iv(NTAB),iy
```

```
      SAVE iv,iy,idum2
      DATA idum2/123456789/, iv/NTAB*0/, iy/0/
      if (idum.le.0) then
        idum=max(-idum,1)
        idum2=idum
        do 11 j=NTAB+8,1,-1
          k=idum/IQ1
          idum=IA1*(idum-k*IQ1)-k*IR1
          if (idum.lt.0) idum=idum+IM1
          if (j.le.NTAB) iv(j)=idum
11      continue
        iy=iv(1)
      endif
      k=idum/IQ1
      idum=IA1*(idum-k*IQ1)-k*IR1
      if (idum.lt.0) idum=idum+IM1
      k=idum2/IQ2
      idum2=IA2*(idum2-k*IQ2)-k*IR2
      if (idum2.lt.0) idum2=idum2+IM2
      j=1+iy/NDIV
      iy=iv(j)-idum2
      iv(j)=idum
      if(iy.lt.1)iy=iy+IMM1
      ran2=min(AM*iy,RNMX)
      return
      END
```

BIBLIOGRAPHY

Appleton, P. N., Davies, R. D., & Stephenson, R. J. 1981, *Monthly Notices of the Royal Astronomical Society*, 195, 327

Bahcall, J. N., Kirhakos, S., Saxe, D. H., & Schneider, D. P. 1997, *Astrophysical Journal*, 479, 642. `arXiv:astro-ph/9611163`

Barentine, J. C., Wakker, B. P., York, D. G., Howk, J. C., Wilhelm, R., van Woerden, H., Peletier, R. F., Beers, T. C., Richter, P., Ivezic, Z., & Schwarz, U. J. 2008, in New Horizons in Astronomy, edited by A. Frebel, J. R. Maund, J. Shen, & M. H. Siegel, vol. 393 of Astronomical Society of the Pacific Conference Series, 179

Barnes, J. E., & Hernquist, L. 1992, *Annual Review of Astronomy and Astrophysics*, 30, 705

— 1996, *Astrophysical Journal*, 471, 115

Begum, A., Chengalur, J. N., Karachentsev, I. D., Kaisin, S. S., & Sharina, M. E. 2006, *Monthly Notices of the Royal Astronomical Society*, 365, 1220. `arXiv:astro-ph/0511253`

Bekki, K. 2008, *Monthly Notices of the Royal Astronomical Society*, 390, L24. `0807.1161`

Ben Bekhti, N., Brüns, C., Kerp, J., & Westmeier, T. 2006, *Astronomy and Astrophysics*, 457, 917. `arXiv:astro-ph/0607383`

Bender, R., & Surma, P. 1992, *Astronomy and Astrophysics*, 258, 250

Binney, J., & Merrifield, M. 1998, Galactic astronomy (Galactic astronomy / James Binney and Michael Merrifield. Princeton, NJ : Princeton University Press, 1998. (Princeton series in astrophysics) QB857 .B522 1998 ($35.00))

Binney, J., Nipoti, C., & Fraternali, F. 2009, *Monthly Notices of the Royal Astronomical Society*, 397, 1804. `0902.4525`

Binney, J., & Tremaine, S. 1987, Galactic dynamics

Boyce, P. J., Minchin, R. F., Kilborn, V. A., Disney, M. J., Lang, R. H., Jordan, C. A., Grossi, M., Lyne, A. G., Cohen, R. J., Morison, I. M., & Phillipps, S. 2001, *Astrophysical Journal Letters*, 560, L127. `arXiv:astro-ph/0109086`

Braun, R., & Burton, W. B. 1999, *Astronomy and Astrophysics*, 341, 437. `arXiv:astro-ph/9810433`

Braun, R., & Thilker, D. A. 2004, *Astronomy and Astrophysics*, 417, 421. `arXiv:astro-ph/0312323`

— 2005, in Extra-Planar Gas, edited by R. Braun, vol. 331 of Astronomical Society of the Pacific Conference Series, 121

Bregman, J. N. 1980, *Astrophysical Journal*, 236, 577

Bregman, J. N., Benjamin, R. A., Bonamente, M., Canizares, C. R., Hornschemeier, A., Jenkins, E., Lockman, F. J., Nicastro, F., Ohashi, T., Paerels, F., Putman, M. E., Sembach, K., Schulz, N., Savage, B., Smith, R., Yamasaki, N., Yao, Y., & Wakker, B. 2009, in AGB Stars and Related Phenomenastro2010: The Astronomy and Astrophysics Decadal Survey, vol. 2010 of Astronomy, 25

Brinks, E., Walter, F., & Skillman, E. D. 2008, in IAU Symposium, edited by J. Davies & M. Disney, vol. 244 of IAU Symposium, 120

Brüns, C., Kerp, J., Kalberla, P. M. W., & Mebold, U. 2000, *Astronomy and Astrophysics*, 357, 120. `arXiv:astro-ph/0003110`

Bureau, M., & Carignan, C. 2002, *Astronomical Journal*, 123, 1316. `arXiv:astro-ph/0112325`

Bushouse, H. A. 1986, *Astronomical Journal*, 91, 255

Cen, R., & Ostriker, J. P. 1999, *Astrophysical Journal*, 514, 1. `arXiv:astro-ph/9806281`

— 2006, *Astrophysical Journal*, 650, 560. `arXiv:astro-ph/0601008`

Chemin, L., Carignan, C., Drouin, N., & Freeman, K. C. 2006, *Astronomical Journal*, 132, 2527. `arXiv:astro-ph/0609148`

Chynoweth, K. M., Langston, G. I., Holley-Bockelmann, K., & Lockman, F. J. 2009, *Astronomical Journal*, 138, 287. `0905.0906`

Chynoweth, K. M., Langston, G. I., Yun, M. S., Lockman, F. J., Rubin, K. H. R., & Scoles, S. A. 2008, *Astronomical Journal*, 135, 1983. `arXiv:0803.3631`

Combes, F., Foy, F. C., Weliachew, L., & Gottesman, S. T. 1980, *Astronomy and Astrophysics*, 84, 85

Cox, T. J., Jonsson, P., Somerville, R. S., Primack, J. R., & Dekel, A. 2008, *Monthly Notices of the Royal Astronomical Society*, 384, 386. `0709.3511`

Cox, T. J., & Loeb, A. 2008, *Monthly Notices of the Royal Astronomical Society*, 386, 461. `0705.1170`

Darg, D. W., Kaviraj, S., Lintott, C. J., Schawinski, K., Sarzi, M., Bamford, S., Silk, J., Andreescu, D., Murray, P., Nichol, R. C., Raddick, M. J., Slosar, A., Szalay, A. S., Thomas, D., & Vandenberg, J. 2010, *Monthly Notices of the Royal Astronomical Society*, 401, 1552. `0903.5057`

Davé, R., Cen, R., Ostriker, J. P., Bryan, G. L., Hernquist, L., Katz, N., Weinberg, D. H., Norman, M. L., & O'Shea, B. 2001, *Astrophysical Journal*, 552, 473. `arXiv:astro-ph/0007217`

Davé, R., Hernquist, L., Katz, N., & Weinberg, D. H. 1999, *Astrophysical Journal*, 511, 521. `arXiv:astro-ph/9807177`

Davé, R., & Oppenheimer, B. D. 2007, *Monthly Notices of the Royal Astronomical Society*, 374, 427. `arXiv:astro-ph/0608268`

de Mello, D. F., Smith, L. J., Sabbi, E., Gallagher, J. S., Mountain, M., & Harbeck, D. R. 2008, *Astronomical Journal*, 135, 548. `0711.2685`

de Vaucouleurs, G. 1953, *Astronomical Journal*, 58, 30

Diemand, J., Kuhlen, M., Madau, P., Zemp, M., Moore, B., Potter, D., & Stadel, J. 2008, *Nature*, 454, 735. `0805.1244`

Dobbs, C. L., Theis, C., Pringle, J. E., & Bate, M. R. 2010, *Monthly Notices of the Royal Astronomical Society*, 159. `0912.1201`

Dolag, K., Meneghetti, M., Moscardini, L., Rasia, E., & Bonaldi, A. 2006, *Monthly Notices of the Royal Astronomical Society*, 370, 656. `arXiv:astro-ph/0511357`

Dopita, M. A., Pereira, M., Kewley, L. J., & Capaccioli, M. 2002, *Astrophysical Journal Supplement*, 143, 47

Eke, V. R., Baugh, C. M., Cole, S., Frenk, C. S., Norberg, P., Peacock, J. A., Baldry, I. K., Bland-Hawthorn, J., Bridges, T., Cannon, R., Colless, M., Collins, C., Couch, W., Dalton, G., de Propris, R., Driver, S. P., Efstathiou, G., Ellis, R. S., Glazebrook, K., Jackson, C., Lahav, O., Lewis, I., Lumsden, S., Maddox, S., Madgwick, D., Peterson, B. A., Sutherland, W., & Taylor, K. 2004, *Monthly Notices of the Royal Astronomical Society*, 348, 866. `arXiv:astro-ph/0402567`

Emsellem, E., Cappellari, M., Krajnović, D., van de Ven, G., Bacon, R., Bureau, M., Davies, R. L., de Zeeuw, P. T., Falcón-Barroso, J., Kuntschner, H., McDermid, R., Peletier, R. F., & Sarzi, M. 2007, *Monthly Notices of the Royal Astronomical Society*, 379, 401. `arXiv:astro-ph/0703531`

Ferrarese, L., & Merritt, D. 2000, *Astrophysical Journal Letters*, 539, L9. `arXiv:astro-ph/0006053`

Fouque, P., Gourgoulhon, E., Chamaraux, P., & Paturel, G. 1992, *Astronomy and Astrophysics Supplement*, 93, 211

Fraternali, F., & Binney, J. J. 2006, *Monthly Notices of the Royal Astronomical Society*, 366, 449. `arXiv:astro-ph/0511334`

Fraternali, F., van Moorsel, G., Sancisi, R., & Oosterloo, T. 2002, *Astronomical Journal*, 123, 3124. `arXiv:astro-ph/0203405`

Fukugita, M., Hogan, C. J., & Peebles, P. J. E. 1998, *Astrophysical Journal*, 503, 518. `arXiv:astro-ph/9712020`

Fukugita, M., & Peebles, P. J. E. 2004, *Astrophysical Journal*, 616, 643. `arXiv:astro-ph/0406095`

Gebhardt, K., Bender, R., Bower, G., Dressler, A., Faber, S. M., Filippenko, A. V., Green, R., Grillmair, C., Ho, L. C., Kormendy, J., Lauer, T. R., Magorrian, J., Pinkney, J., Richstone, D., & Tremaine, S. 2000, *Astrophysical Journal Letters*, 539, L13. `arXiv:astro-ph/0006289`

Geller, M. J., & Huchra, J. P. 1983, *Astrophysical Journal Supplement*, 52, 61

Gerin, M., Combes, F., & Athanassoula, E. 1990, *Astronomy and Astrophysics*, 230, 37

Gnedin, N. Y. 2000, *Astrophysical Journal*, 542, 535. `arXiv:astro-ph/0002151`

Grossi, M., Giovanardi, C., Corbelli, E., Giovanelli, R., Haynes, M. P., Martin, A. M., Saintonge, A., & Dowell, J. D. 2008, *Astronomy and Astrophysics*, 487, 161. `0806.0412`

Hernquist, L. 1990, *Astrophysical Journal*, 356, 359

— 1993, *Astrophysical Journal Supplement*, 86, 389

Hess, K. M., Pisano, D. J., Wilcots, E. M., & Chengalur, J. N. 2009, *Astrophysical Journal*, 699, 76. `0904.3494`

Holley-Bockelmann, K. 2010. In prep

Huchtmeier, W. K., & Skillman, E. D. 1998, *Astronomy and Astrophysics Supplement*, 127, 269

Hummel, E., van der Hulst, J. M., Kennicutt, R. C., & Keel, W. C. 1990, *Astronomy and Astrophysics*, 236, 333

Hut, P., & Makino, J. 2004, Moving stars around: The art of computational science. `http://www.artcompsci.org/msa/web/index.html`

Joung, M. K. R., Chynoweth, K. M., Holley-Bockelmann, K., & Cen, R. 2010. In prep

Kalberla, P. M. W., Burton, W. B., Hartmann, D., Arnal, E. M., Bajaja, E., Morras, R., & Pöppel, W. G. L. 2005, *Astronomy and Astrophysics*, 440, 775. `arXiv:astro-ph/0504140`

Karachentsev, I. D., Dolphin, A. E., Geisler, D., Grebel, E. K., Guhathakurta, P., Hodge, P. W., Karachentseva, V. E., Sarajedini, A., Seitzer, P., & Sharina, M. E. 2002, *Astronomy and Astrophysics*, 383, 125

Karachentsev, I. D., & Kaisin, S. S. 2007, *Astronomical Journal*, 133, 1883. `arXiv:astro-ph/0701465`

Karachentsev, I. D., Karachentseva, V. E., Huchtmeier, W. K., & Makarov, D. I. 2004, *Astronomical Journal*, 127, 2031

Karachentsev, I. D., Sharina, M. E., Dolphin, A. E., Grebel, E. K., Geisler, D., Guhathakurta, P., Hodge, P. W., Karachentseva, V. E., Sarajedini, A., & Seitzer, P. 2003, *Astronomy and Astrophysics*, 398, 467. `arXiv:astro-ph/0210414`

Keel, W. C., Kennicutt, R. C., Jr., Hummel, E., & van der Hulst, J. M. 1985, *Astronomical Journal*, 90, 708

Kennicutt, R. C., Jr. 1998, *Astrophysical Journal*, 498, 541. `arXiv:astro-ph/9712213`

Kennicutt, R. C., Jr., & Keel, W. C. 1984, *Astrophysical Journal Letters*, 279, L5

Kennicutt, R. C., Jr., Lee, J. C., Funes, S. J., José G., Sakai, S., & Akiyama, S. 2008, *Astrophysical Journal Supplement*, 178, 247. `0807.2035`

Kereš, D., & Hernquist, L. 2009, *Astrophysical Journal Letters*, 700, L1. `0905.2186`

Kereš, D., Katz, N., Weinberg, D. H., & Davé, R. 2005, *Monthly Notices of the Royal Astronomical Society*, 363, 2. `arXiv:astro-ph/0407095`

Knapen, J. H., & James, P. A. 2009, *Astrophysical Journal*, 698, 1437. `0904.4263`

Kravtsov, A. V., Gnedin, O. Y., & Klypin, A. A. 2004, *Astrophysical Journal*, 609, 482. `arXiv:astro-ph/0401088`

Kuo, C., Lim, J., Tang, Y., & Ho, P. T. P. 2008, *Astrophysical Journal*, 679, 1047. `0802.4205`

Lacey, C. 1989, *Nature*, 340, 675

Lang, K. R. 1999, Astrophysical formulae (Astrophysical formulae / K.R. Lang. New York : Springer, 1999. (Astronomy and astrophysics library,ISSN0941-7834))

Langston, G., & Turner, B. 2007, *Astrophysical Journal*, 658, 455

Larson, R. B., & Tinsley, B. M. 1978, *Astrophysical Journal*, 219, 46

Laurikainen, E., & Salo, H. 1995, *Astronomy and Astrophysics*, 293, 683

Lockman, F. J., Benjamin, R. A., Heroux, A. J., & Langston, G. I. 2008, *Astrophysical Journal Letters*, 679, L21. `0804.4155`

Lockman, F. J., Murphy, E. M., Petty-Powell, S., & Urick, V. J. 2002, *Astrophysical Journal Supplement*, 140, 331. `arXiv:astro-ph/0201039`

Lotz, J. M., Jonsson, P., Cox, T. J., & Primack, J. R. 2008, *Monthly Notices of the Royal Astronomical Society*, 391, 1137. `0805.1246`

Maller, A. H., & Bullock, J. S. 2004, *Monthly Notices of the Royal Astronomical Society*, 355, 694. `arXiv:astro-ph/0406632`

McKinnon, M. 2002, Green Bank Telescope, NRAO Eighth Synthesis Imaging Summer School

Mihos, J. C. 2004, in Recycling Intergalactic and Interstellar Matter, edited by P.-A. Duc, J. Braine, & E. Brinks, vol. 217 of IAU Symposium, 390

Mihos, J. C., & Hernquist, L. 1996, *Astrophysical Journal*, 464, 641. `arXiv:astro-ph/9512099`

Miller, E. D., Bregman, J. N., & Wakker, B. P. 2009, *Astrophysical Journal*, 692, 470. `0810.5130`

Mirabel, I. F., & Morras, R. 1984, *Astrophysical Journal*, 279, 86

Mulder, P. S., & van Driel, W. 1993, *Astronomy and Astrophysics*, 272, 63

Muller, C. A., Oort, J. H., & Raimond, E. 1963, Academie des Sciences Paris Comptes Rendus, 257, 1661

Naab, T., Burkert, A., & Hernquist, L. 1999, *Astrophysical Journal Letters*, 523, L133. `arXiv:astro-ph/9908129`

Navarro, J. F., Frenk, C. S., & White, S. D. M. 1996, *Astrophysical Journal*, 462, 563. `arXiv:astro-ph/9508025`

Noguchi, M. 1988, *Astronomy and Astrophysics*, 203, 259

Oh, S. H., Kim, W., Lee, H. M., & Kim, J. 2008, *Astrophysical Journal*, 683, 94. `0803.1893`

Oosterloo, T., Fraternali, F., & Sancisi, R. 2007, *Astronomical Journal*, 134, 1019. `0705.4034`

Ott, M., Witzel, A., Quirrenbach, A., Krichbaum, T. P., Standke, K. J., Schalinski, C. J., & Hummel, C. A. 1994, *Astronomy and Astrophysics*, 284, 331

Pisano, D. J., Barnes, D. G., Gibson, B. K., Staveley-Smith, L., Freeman, K. C., & Kilborn, V. A. 2007, *Astrophysical Journal*, 662, 959. `arXiv:astro-ph/0703279`

Popping, A., Davé, R., Braun, R., & Oppenheimer, B. D. 2009, *Astronomy and Astrophysics*, 504, 15. `0906.3067`

Putman, M. E., de Heij, V., Staveley-Smith, L., Braun, R., Freeman, K. C., Gibson, B. K., Burton, W. B., Barnes, D. G., Banks, G. D., Bhathal, R., de Blok, W. J. G., Boyce, P. J., Disney, M. J., Drinkwater, M. J., Ekers, R. D., Henning, P. A., Jerjen, H., Kilborn, V. A., Knezek, P. M., Koribalski, B., Malin, D. F., Marquarding, M., Minchin, R. F., Mould, J. R., Oosterloo, T., Price, R. M., Ryder, S. D., Sadler, E. M., Stewart, I., Stootman, F., Webster, R. L., & Wright, A. E. 2002, *Astronomical Journal*, 123, 873. `arXiv:astro-ph/0110416`

Putman, M. E., Staveley-Smith, L., Freeman, K. C., Gibson, B. K., & Barnes, D. G. 2003, *Astrophysical Journal*, 586, 170. `arXiv:astro-ph/0209127`

Quilis, V., & Moore, B. 2001, *Astrophysical Journal Letters*, 555, L95. `arXiv:astro-ph/0106253`

Rossa, J., & Dettmar, R. 2003, *Astronomy and Astrophysics*, 406, 505. `arXiv:astro-ph/0305472`

Rudick, C. S., Mihos, J. C., Frey, L. H., & McBride, C. K. 2009, *Astrophysical Journal*, 699, 1518. `0906.1185`

Rybicki, G. B., & Lightman, A. P. 1979, Radiative processes in astrophysics (New York, Wiley-Interscience, 1979. 393 p.)

Sancisi, R., Fraternali, F., Oosterloo, T., & van der Hulst, T. 2008, *Astronomy and Astrophysics Review*, 15, 189. `0803.0109`

Sanders, D. B., Soifer, B. T., Elias, J. H., Madore, B. F., Matthews, K., Neugebauer, G., & Scoville, N. Z. 1988, *Astrophysical Journal*, 325, 74

Schinnerer, E., Böker, T., Emsellem, E., & Lisenfeld, U. 2006, *Astrophysical Journal*, 649, 181. `arXiv:astro-ph/0605702`

Schwarz, U. J., Wakker, B. P., & van Woerden, H. 1995, *Astronomy and Astrophysics*, 302, 364

Shapiro, P. R., & Field, G. B. 1976, *Astrophysical Journal*, 205, 762

Shull, J. M., Jones, J. R., Danforth, C. W., & Collins, J. A. 2009, *Astrophysical Journal*, 699, 754. `0904.4901`

Silk, J. 1990, Canadian Journal of Physics, 68, 799

Simon, J. D., Blitz, L., Cole, A. A., Weinberg, M. D., & Cohen, M. 2006, *Astrophysical Journal*, 640, 270. `arXiv:astro-ph/0511542`

Simon, J. D., & Geha, M. 2007, *Astrophysical Journal*, 670, 313. `0706.0516`

Sofue, Y. 1998, Publ. of the Astronomical Society of Japan, 50, 227. `arXiv:astro-ph/9803012`

Sohn, Y., & Davidge, T. J. 1996, *Astronomical Journal*, 112, 2559

Sparke, L. S., & Gallagher, J. S. 2000, "Galaxies in the Universe" (Cambridge University Press)

Springel, V., Di Matteo, T., & Hernquist, L. 2005, *Monthly Notices of the Royal Astronomical Society*, 361, 776. `arXiv:astro-ph/0411108`

Stil, J. M., Lockman, F. J., Taylor, A. R., Dickey, J. M., Kavars, D. W., Martin, P. G., Rothwell, T. A., Boothroyd, A. I., & McClure-Griffiths, N. M. 2006, *Astrophysical Journal*, 637, 366. `arXiv:astro-ph/0509730`

Strickland, D. K., Heckman, T. M., Colbert, E. J. M., Hoopes, C. G., & Weaver, K. A. 2004, *Astrophysical Journal*, 606, 829. `arXiv:astro-ph/0306598`

Tago, E., Einasto, J., Saar, E., Tempel, E., Einasto, M., Vennik, J., & Müller, V. 2008, *Astronomy and Astrophysics*, 479, 927. `0706.1593`

Thilker, D. A., Braun, R., Walterbos, R. A. M., Corbelli, E., Lockman, F. J., Murphy, E., & Maddalena, R. 2004, *Astrophysical Journal Letters*, 601, L39. `arXiv:astro-ph/0311571`

Thom, C., Putman, M. E., Gibson, B. K., Christlieb, N., Flynn, C., Beers, T. C., Wilhelm, R., & Lee, Y. S. 2006, *Astrophysical Journal Letters*, 638, L97. `arXiv:astro-ph/0601139`

Thronson, H. A., Jr., Hunter, D. A., Casey, S., Harper, D. A., & Latter, W. B. 1989, *Astrophysical Journal*, 339, 803

Toomre, A., & Toomre, J. 1972, *Astrophysical Journal*, 178, 623

Tully, R. B. 1987, *Astrophysical Journal*, 321, 280

Urry, C. M., & Padovani, P. 1995, *Publications of the Astronomical Society of the Pacific*, 107, 803. `arXiv:astro-ph/9506063`

van der Hulst, T., & Sancisi, R. 1988, *Astronomical Journal*, 95, 1354

van Woerden, H., Peletier, R. F., Schwarz, U. J., Wakker, B. P., & Kalberla, P. M. W. 1999a, in Stromlo Workshop on High-Velocity Clouds, edited by B. K. Gibson, & M. E. Putman, vol. 166 of Astronomical Society of the Pacific Conference Series, 1

van Woerden, H., Schwarz, U. J., Peletier, R. F., Wakker, B. P., & Kalberla, P. M. W. 1999b, *Nature*, 400, 138. `arXiv:astro-ph/9907107`

van Woerden, H., Wakker, B. P., Schwarz, U. J., & de Boer, K. S. (eds.) 2004, High Velocity Clouds, vol. 312 of Astrophysics and Space Science Library

Wakker, B. P. 1991, *Astronomy and Astrophysics*, 250, 499

Wakker, B. P., & van Woerden, H. 1997, *Annual Review of Astronomy and Astrophysics*, 35, 217

Wakker, B. P., York, D. G., Howk, J. C., Barentine, J. C., Wilhelm, R., Peletier, R. F., van Woerden, H., Beers, T. C., Ivezić, Ž., Richter, P., & Schwarz, U. J. 2007, *Astrophysical Journal Letters*, 670, L113. `arXiv:0710.3340`

Westmeier, T. 2009, All-sky map of high velocity clouds. `http://www.atnf.csiro.au/people/Tobias.Westmeier/research_hvcsky.php`

Westmeier, T., Braun, R., Brüns, C., Kerp, J., & Thilker, D. A. 2007, New Astronomy Review, 51, 108

Westmeier, T., Braun, R., & Thilker, D. 2005a, *Astronomy and Astrophysics*, 436, 101. `arXiv:astro-ph/0503246`

Westmeier, T., Brüns, C., & Kerp, J. 2005b, in Extra-Planar Gas, edited by R. Braun, vol. 331 of Astronomical Society of the Pacific Conference Series, 105

— 2008, *Monthly Notices of the Royal Astronomical Society*, 390, 1691. `0808.3611`

Wetzel, A. R. 2010, ArXiv e-prints. `1001.4792`

Wetzstein, M., Naab, T., & Burkert, A. 2007, *Monthly Notices of the Royal Astronomical Society*, 375, 805. `arXiv:astro-ph/0510821`

Yun, M. S. 1999, in Galaxy Interactions at Low and High Redshift, edited by J. E. Barnes, & D. B. Sanders, vol. 186 of IAU Symposium, 81

Yun, M. S., Ho, P. T. P., & Lo, K. Y. 1993, *Astrophysical Journal Letters*, 411, L17

— 1994, *Nature*, 372, 530

Zitrin, A., & Brosch, N. 2008, *Monthly Notices of the Royal Astronomical Society*, 390, 408. `0808.1789`

Zwaan, M. A., Staveley-Smith, L., Koribalski, B. S., Henning, P. A., Kilborn, V. A., Ryder, S. D., Barnes, D. G., Bhathal, R., Boyce, P. J., de Blok, W. J. G., Disney, M. J., Drinkwater, M. J., Ekers, R. D., Freeman, K. C., Gibson, B. K., Green, A. J., Haynes, R. F., Jerjen, H., Juraszek, S., Kesteven, M. J., Knezek, P. M., Kraan-Korteweg, R. C., Mader, S., Marquarding, M., Meyer, M., Minchin, R. F., Mould, J. R., O'Brien, J., Oosterloo, T., Price, R. M., Putman, M. E., Ryan-Weber, E., Sadler, E. M., Schröder, A., Stewart, I. M., Stootman, F., Warren, B., Waugh, M., Webster, R. L., & Wright, A. E. 2003, *Astronomical Journal*, 125, 2842. `arXiv:astro-ph/0302440`